Max-Planck Institut für Kolloid- und Grenzflächenforschung

Sustainable electrode materials based on lignin

Saowaluk Chaleawlert-umpon

Dissertation

Zur Erlangung des akademischen Grades
“Doctor rerum naturalium”
(Dr. rer. nat.)
in der Wissenschaftsdisziplin “Kolloidchemie”

Eingereicht an der
Mathematisch-Naturwissenschaftlichen Fakultät
der Universität Potsdam

Published online at the
Institutional Repository of the University of Potsdam:
URN urn:nbn:de:kobv:517-opus4-411793
http://nbn-resolving.de/urn:nbn:de:kobv:517-opus4-411793

Table of contents

		Page
1.	Introduction	2
1.1	Motivation	2
1.2	Energy storage technology	4
1.3	Batteries	6
1.4	Lithium-ion batteries (LIBs)	9
1.4.1	Anode materials	9
1.4.2	Cathode materials	9
1.5	Organic electrodes for batteries	10
1.5.1	Introduction and principle	10
1.5.2	Quinones	12
1.6	Lignin	15
1.6.1	Introduction and chemical structure	15
1.6.2	Isolation processes	16
1.6.3	Applications	19
2.	Kraft lignin-carbon composite for sustainable cathode materials	24
2.1	Background and objective	24
2.2	Electrochemistry of Kraft lignin-carbon composites	26
2.3	Conclusion	37
3.	Modification of Kraft lignin with dialdehyde crosslinkers for cathode materials	38
3.1	Background and objective	38
3.2	Characterization	41
3.3	Charge storage properties of a binder-free lignin composite electrode	55
3.4	Conclusion	63
4.	Oxidation of Kraft lignin for cathode materials	64
4.1	Background and objective	64
4.2	Battery testing of the glyoxalated lignin based electrode	67
4.3	Oxidation reaction of 2-methoxy-4-methylphenol (MMP) with Cerium ammonium nitrate (CAN)	70
4.4	Oxidation reaction of lignin with cerium ammonium nitrate (CAN)	74
4.5	Lithium battery application	77
4.6	Conclusion	79
5.	Conclusion and outlook	80
	Appendix	83
	A. Materials and methods	83
	B. Experimental parts	89
	C. Supplementary information	93
	D. List of abbreviations	103
	E. List of publications	105
	F. Acknowledgements	106
	G. Declaration	107
	H. References	108

1. Introduction

1.1 Motivation

With the ever-increasing global population, world annual energy consumption is set to double from 14 terawatts (TW) in 2010 to 28 TW in 2050. This equates to 130,000 TWh or the equivalent of 10^{10} tons of oil yearly (Figure 1-1 (a)).[1] Oil and coal have remained the dominant primary energy sources of world energy consumption followed by natural gas, which has also undergone considerable growth, while renewable energy showing gradual growth (Figure 1-1 (b)).[2] Owing to the limitations of crude oil storage and global warming concerns, there is an increasing need to switch to alternative and renewable energy sources.

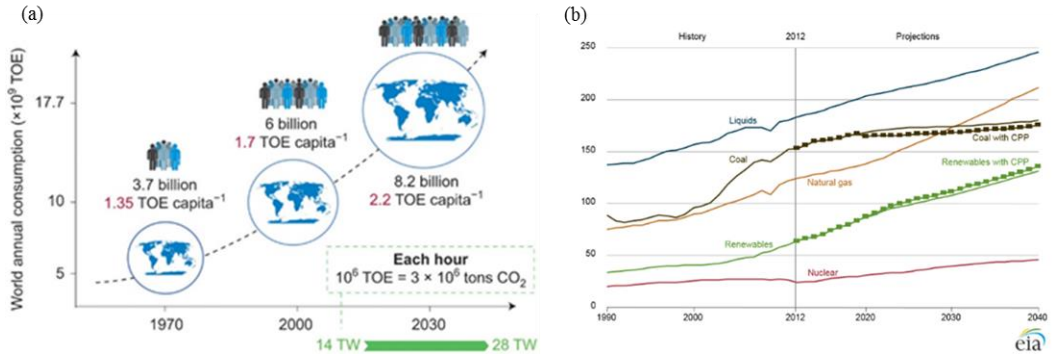

Figure 1-1 (a) The world's energy needs from the past to 2050; TOE = ton of oil equivalent[1] and (b) Plot between world energy consumption by energy source (quadrillion Btu) and year during 1990-2040.[3]

Electricity is the world's fastest growing form of end-use energy consumption, as it has been for many decades. World net electricity generation will increase by 69% from 21.6 trillion kWh in 2012 to 25.8 trillion kWh in 2020 and to 36.5 trillion kWh in 2040. Electricity is generated from many primary energy sources, and it is expected that use of non-fossil resources will grow at a faster rate than fossil fuels for such means before 2040 (Figure 1-2).[2] In the recent years, there have been many efforts to reduce CO_2 emission in order to mitigate the negative environmental impact by seeking green and renewable resources for the production of electricity. A major drawback of renewable energy sources is an uneven energy generation which strongly affects the cost and reliability of electricity. To overcome this problem, energy storage systems (ESSs) are required to transform power from renewable sources in intermediate storage and match supply with demand in different

consumption periods. This current research focuses on the improvement of electric energy storage also in part due to the key role of mobile energy applications.

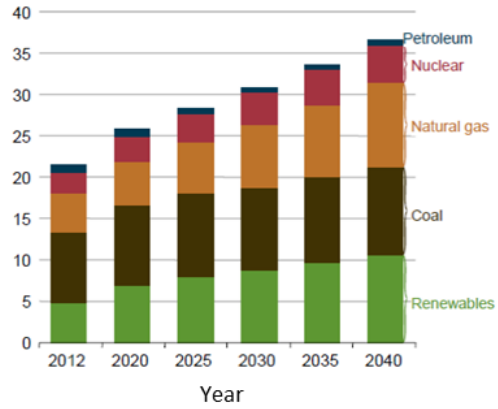

Figure 1-2 World net electricity generation by energy source in trillion kilowatt hours.[3]

As conventional metal-based inorganic compounds in electrochemical energy storage systems (EESSs) normally generate toxic and heavy metal waste in processing and synthesis, organic materials such as conducting polymers, conjugated carbonyl, organosulfur, and radical compounds, being abundant, flexible, lightweight, low-cost, non-toxic compounds, provide an excellent opportunity to further improve existing energy storage technologies and develop a versatile platform for novel EESSs.[4] Quinone-based compounds, a group of carbonyl compounds, are promising organic materials due to their natural occurrence. Lignin is the second most abundant biopolymer isolated from wood, annual plants such as wheat straw, or agricultural residues. Approximately 40 or 50 million tons per annum are produced worldwide as a mostly non-commercialized waste product from numerous pulping processes in the paper and biorefinery industries. Lignin is an aromatic heteropolymer featuring many phenolic or phenolate moieties converted to a quinone/hydroquinone redox active couple. Thus, lignin may serve as organic material for energy storage applications since it has many respective structure motifs.

This thesis focuses on the utilization of lignin biopolymer serving as sustainable redox active materials within the framework of electrochemical energy storage. A more sustainable way to fabricate the composite electrode than previous reports which described lignin composites with expensive conducting synthetic polymers, carbon nanotubes (CNTs),[5] or graphene,[6] was used. Sustainable conductive carbon additives were selected because they are inexpensive, safe, and involve facile production. Moreover, the fabrication of the electrode involves fewer steps and less toxic chemicals. To evaluate the

electrochemical behavior of lignin-carbon composites by studying redox and non-redox process contribution, composites of commercial Kraft lignin were prepared with different active surface areas of conductive carbon. The interplay between lignin and conductive carbon and the influence of the lignin-to-carbon ratio were studied. Two means of lignin modification were investigated to improve their electrochemical performance. Based on the concept of green chemistry, the crosslinking of lignin with glyoxal, which is a safe and halogen-free chemical, was carried out with a two-step and eco-efficient process of electrode fabrication to improve the stability of lignin and charge storage capacity. Oxidation of lignin with cerium ammonium nitrate (CAN) to enhance quinone active moieties was performed, and the product was tested for lithium primary battery performance.

1.2 Energy storage technology

Energy storage technologies have started to play a vital role in our lives since the discovery of electricity. Regarding the forms of energy storage, this can be classified into four main categories: electrical, chemical, mechanical, and thermal ESSs.[7-12] Currently, the dominating energy storage device for electricity remains the battery as well as supercapacitor depending on their applications. The most widely used rechargeable battery is the lead-acid battery but the fastest growing battery market is that of the lithium-ion battery (LIB).[7-9,11,13] One of the most common comparisons of the operational characteristics for various energy storage devices is the so-called Ragone plot which usually presents power density as a function of energy density as shown in Figure 1-3. Specific energy, or gravimetric energy density, defines battery capacity per weight (Wh kg^{-1}); energy density, or volumetric energy density, defines battery capacity per volume (Wh l^{-1}). It is a function of the cell's voltage and capacity depends on the chemistry of the system. A high energy density system has the ability to store a large amount of energy. Specific power (W kg^{-1}), or volumetric power density (W l^{-1}), is the rate of energy release. Compared to other devices, the LIB provides relatively large power at very high energy. In contrast, supercapacitors are the devices with the highest power and the lowest energy supply in the plot.

Electrochemical charge storage is generally based on the following electrode processes: faradaic and non-faradaic storage mechanisms. A faradaic process, the essential process in

battery-type electrodes, is involved in charge (or electron) transfer through the faradaic reaction or chemical redox reaction of electroactive materials according to Faraday's laws related to electrode potential. The charge storage of the battery-type electrode usually relates to a phase transformation from an oxidation state change and an intercalation reaction of cation (H^+ or Li^+) throughout the entire bulk of electrode materials. Consequently, this allows for a large amount of energy to be stored with slow kinetics of energy uptake and delivery. Furthermore, there is invariably some degree of irreversibility resulting in a limited number of cycles in the range of one thousand to several thousand depending on the battery type.[14-17]

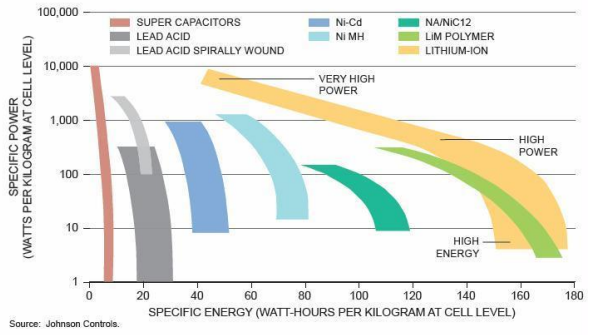

Figure 1-3 Ragone plot of many rechargeable batteries used in energy storage applications.[18]

A non-faradaic process stores charges through physical charge adsorption or accumulation by the electrostatic interaction at the electrode/electrolyte interface giving rise to an electrical double layer (EDL) capacitance. This process has no electron transfer across the electrode/electrolyte interface, and no chemical changes inside the solid phase of the electrode (without a phase change). The charge storage is not limited by the rate of chemical or electrochemical reactions and the diffusion process; hence, they have a high power capability, a fast energy uptake and delivery, and a great degree of cyclability. However, they suffer from limited energy density due to the limited charge storage on the surface of the electrode materials.[14,16,17,19]

The capacitance of supercapacitors mainly arises from the surface reactions of the electrode materials including the electrosorption of charges (non-faradaic or capacitive behavior) and the surface faradaic redox reactions (pseudocapacitive behavior). The typical EDL capacitance relies on the high surface area of active materials, commonly carbon-based materials. Pseudocapacitance is developed from a fast surface or near-surface faradaic charge-transfer mechanism, and a highly reversible change in the oxidation state

without a phase transition. Its electrochemical behavior is nearly identical with that of traditional capacitive behavior, which is termed pseudocapacitive behavior.[6,15,20] Faradaic pseudocapacitance only occurs accompanied by EDL capacitance; thus, pseudocapacitance is the ability to store a greater amount of charge than EDL capacitance. Transition metal oxides (e.g., RuO_2, Fe_3O_4, and MnO_2) and conductive polymers (e.g., polypyrrole (PPy), polyaniline (PANI), and polythiophene) are the typical active materials for the pseudocapacitive behavior of supercapacitor-type electrodes.[20-23] Figure 1-4 summarizes the electrochemical charge storage mechanisms.

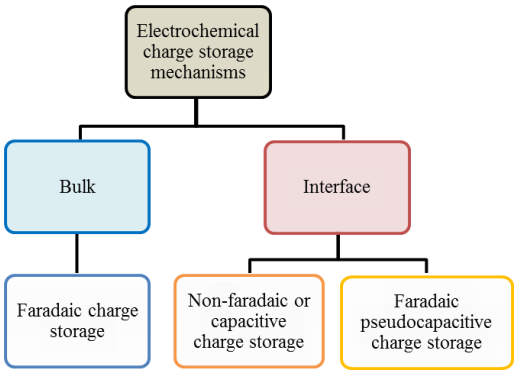

Figure 1-4 Different mechanisms of electrochemical charge storage.

Supercapacitors are the preferred choice in power device applications that can be charged and discharged in bursts repeatedly, even if their energy density is lower than in batteries. In contrast, batteries supply slow and steady energy for large energy demands over longer periods of time. Since both batteries and supercapacitors have individual features, they can be ideal partners for several applications such as hybrid buses and electric cars.[24] Finally, energy storage research generally focuses on moving every device's performance closer to the upper right-hand corner of the Ragone plot to gain optimum power and energy density to perform similarly to a normal combustion engine or gas turbine.[25]

1.3 Batteries

A battery is defined as one or more electrically connected electrochemical cells having terminals/contacts to supply electrical energy. The operation of a battery is well known as a galvanic cell with two electrodes (an anode and cathode) placed in ionically conductive electrolyte solutions and connected by a salt bridge or porous membrane (Figure 1-5).

Batteries operate with a constant voltage defined by the potential difference between two electrodes based on oxidation/reduction processes. During energy conversion, one component (with the lower positive standard reduction potential) is oxidized and transfers its electrons over an external circuit to another redox-active species (with the higher positive standard reduction potential) that is reduced. The potential difference between two active electrodes is known as the operating voltage. It is used to force electrochemical reactions on each electrode after being connected through an external circuit. During discharge, the electron flows from oxidation reactions (at anode) toward reduction reactions (at cathode) and the reverse electron flowing takes place when charging (in case of rechargeable batteries). The charges formed at the electrodes are balanced by electrolyte ions.

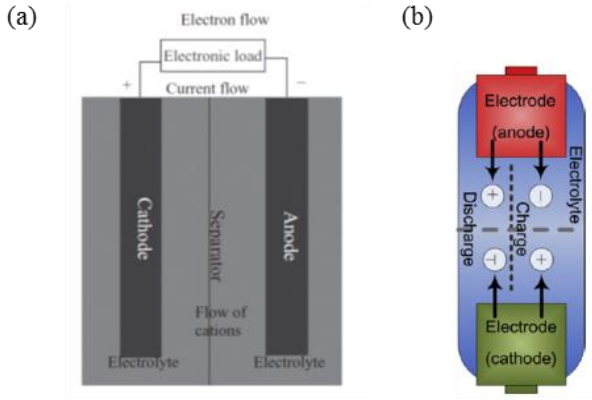

Figure 1-5 (a) The schematic diagram of a simple galvanic cell[26] and (b) Terminal designs for cylindrical batteries. Reprinted by permission.[10] Copyright 2015, Pergamon.

There are two main types of batteries: primary and secondary batteries. The primary batteries are also known as non-rechargeable batteries because their chemical reactions are generally not reversible. They can be used only once to generate electricity. Due to their high specific energy, long storage times and low price, they have a unique advantage over other power sources in applications where charging is impracticable such as in military combat, rescue missions, and forest-fire services. Many types of primary batteries exist, such as alkaline batteries (Zn/MnO_2 as active materials in KOH electrolyte) with energy density in the range of 40-100 Wh kg^{-1} and Li primary batteries (Li/MnO_2 or $Li/(CF)_n$) with energy density around 200-250 Wh kg^{-1}.[27] The secondary cells are (re)charged by applying electric current, which reverses the chemical reactions that occur during discharge. Electrons flow to the anode through the external circuit and cations from the cathode diffuse through the electrolyte to the anode during charging and the reverse

electron flowing takes place when discharging. Secondary cells can be recharged electrically several times after being discharged. Several different combinations of electrode materials and electrolytes are used and the most common are lead-acid, nickel cadmium (NiCd), nickel metal hydride (NiMH), sodium sulphur (Na-S), and LIBs. The ideal battery would not only have high power and energy density but also possess long life, compact size, light weight, safety, environmental compatibility, as well as be low in cost and distributed to consumers worldwide. Currently, no commercialized batteries can fully satisfy all these requirements. Furthermore, most display discharge capacities and energy densities far below their theoretical values.[28] The main parameters of batteries are defined in Table1-1.

Table 1-1 Battery characteristics.[29,30]

Battery characteristics	**Definition**	**Unit**
Open-circuit voltage	Maximum voltage in the charged state at zero current	Volts (V)
Current density (by weight or by area)	The electric current per unit weight or cross-section area of the cell	Amperes per gram (A g^{-1}) or Amperes per square meters (A m^{-2})
Energy density (by weight or by volume)	The energy that can be derived per unit of the weight or volume of the cell	Watt-hours per kilogram (Wh kg^{-1}) of Watt-hours per liter (Wh l^{-1})
Specific energy density	The energy that can be derived per unit weight of the cell	Watt-hours per kilogram (Wh kg^{-1})
Specific power density	The power that can be derived per unit weight of the cell	Watts per kilogram (W kg^{-1})
Specific capacity	The theoretical capacity of the battery is the maximum quantity of electricity involved in the electrochemical reaction	Ampere-hours per gram (Ah g^{-1})
Cycle life	The number of charge/discharge cycles before its capacity falls to 80%	Cycles
Coulombic efficiency	The ratio of the obtained discharging and charging capacity	Percent (%)

1.4 Lithium-ion batteries (LIBs)

LIB chemistry was proposed in 1976 by M. S. Whittingham and first commercialized in 1991 by SONY.[30] The great attractiveness of the LIBs comes from the low weight of Li metal (6.94 g mol^{-1} molecular weight and 0.51 g cm^{-3} density). Lithium is also the most electropositive element found in nature and possesses the highest electro-activity. The specific capacity of Li metal is 3,860 mAh g^{-1} and its standard redox potential is 3.04 V.

1.4.1 Anode materials

A wide variety of chemical reactions are used in the low voltage range required for the anode materials in LIBs. Normally, metallic Li is an excellent anode material, and it is used in Li primary cells. However, Li can form dendrites in rechargeable LIBs, which may lead to serious safety problems. Carbonaceous materials and Sn/Si alloys have been proposed as viable materials.[28,31-33]

1.4.2 Cathode materials

The capacity of LIBs is based on the intercalation concept and mainly restricted by the cathode materials. In the early era of LIBs, metal chalcogenides (e.g., TiS_2 and MoS_2) and manganese or vanadium oxides were used as the cathodes to pair with metallic Li, Li alloys, or graphite anodes leading to the commercial success of rechargeable LIBs.[25,28,34] During the last decade, layered compounds such as $LiCoO_2$, $LiNiO_2$, and the three-dimensional (3-D) $LiMn_2O_4$ spinel phase, were seen as promising candidates for cathode materials.[32] Recently, considerable interest has been directed to a new class of materials with an olivine structure, such as $LiMPO_4$ (M=Fe, Mn, Co), or polyanion-based compounds which potentially allow for low cost and high safety.[31,35,36] Shifting from the traditional insertion-compound-based LIBs to new types of battery systems such as Li-air and Li-S may provide a real breakthrough in terms of performance and sustainability.[4,31,36-41] Furthermore, one research trend is renewable organic materials as strong promising and "green" alternatives to conventional inorganic systems; however, their development is still at a preliminary research level (Figure 1-6).[36,42]

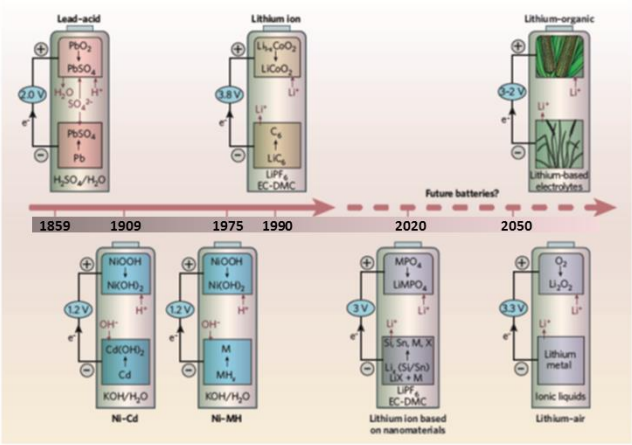

Figure 1-6 Battery technologies: past to future trends (adapted). Reprinted and adapted by permission.[42] Copyright 2008, Nature Publishing Group

1.5 Organic electrodes for batteries

1.5.1 Introduction and principle

The biggest drawback of inorganic electrode materials is the environmental impact from extraction, metal-refining, and recycling leading to the release of toxic materials or heavy metal wastes. In addition, the process often requires energy-intensive manufacturing including green-house gas emissions. This is why the concept of organic matter-based electrode materials has gained interest. Switching from inorganic to organic materials offers the true possibility of their preparation from renewable resources and by eco-friendly processes coupled with simplified recycling management.[43]

The cost of materials is essentially the main factor to consider during the stage of commercialization. As such, the cathode in LIBs can account for ~30% of the cost of the device. It is fairly important to develop low cost materials for applications which do not require high performance.[4] Since 1969, organic materials have been studied as electrodes for EESSs with the first report using dichloroisocyanuric acid as a cathode material.[44] Over past decades, many different organic structures and redox mechanisms have been investigated as regards achieving higher electrochemical performance such as various small organic molecules (e.g., quinones,[45] dianhydrides,[46] and phthalocyanines[47]). Conductive polymers such as PPy and PANI, and derivatives[48,49] were later assessed. Nevertheless, research on organic electrode materials for energy storage diminished as inorganic transition metal complexes were developed. The main reason for this was due to

their poor electrochemical performance compared to inorganic material, particularly in LIBs. The solubility in the electrolyte represents a further challenge for the development of organic electrode materials. Dissolution of active material leads to self-discharge of the battery that significantly affects the cycling stability. Incorporation of the redox-active unit into a polymeric backbone is an approach used to overcome this issue.

Until the 2000s, nitroxyl radical polymers and conjugated carbonyl compounds achieved great progress in this field.[50,51] Currently, the electrochemical performance of some organic cathode materials is comparable to conventional inorganic cathodes including energy density, power density and cycling stability.[52] Many organic Li battery materials have been studied such as carbonyl compounds,[53-56] conducting polymers,[48,57-59] radicals,[55,60] and organosulfur compounds.[51,61-63]

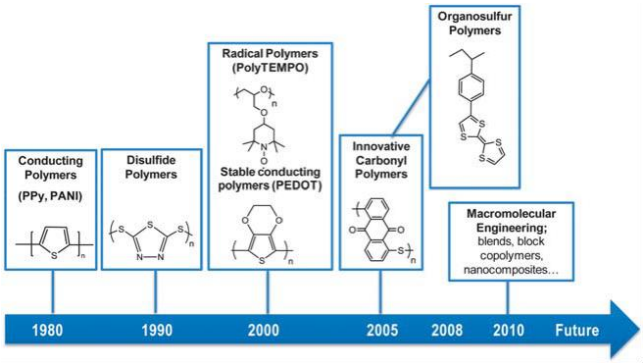

Figure 1-7 Development timeline of the most important polymers for batteries. Reprinted by permission.[64] Copyright 2013, Royal Society of Chemistry.

Figure 1-7 summarizes the historical discoveries in the use of polymer electrodes in batteries including the future opportunities of macromolecular engineering to design redox polymers. In addition to structural diversity, there are several unique features of organic materials such as light weight, abundance, less toxicity compared to traditional materials, processability, and low cost.[50,52,65] The basic requirements for electrode materials are the presence of a reversible redox reaction, high theoretical capacity (C_{theor}), chemical stability, simple synthesis and low cost, and stable redox potential.

Redox processes of inorganic materials are related to the valence charge of the metal and based on complex intercalation mechanisms which are accompanied by the transformation of the lattice and the layered structure. Consequently, slow kinetics and heat generation during the charge/discharge process occur and limit the usage of classical LIBs in high power applications. In contrast, organic materials are based on a change of the state of

charge of the electroactive groups leading to a simple and fast redox process with less extensive structural change. They provide high rate performances and long cycling ability. Nevertheless, the limiting factors of organic batteries are the migration of electrolyte ions and the rate constant for the electron transfer of the redox reaction.[30,52,66]

Organic compounds are more often suitable as cathode than as anode materials. Their redox potentials are typically between 2 and 4 V *vs.* Li^+/Li. However, the electroactive groups of organic compounds can be tuned by different chemical structures or functional groups such as electron-withdrawing and -donating groups. This produces flexible compounds with different redox potentials.[30,52] Due to the adjustable chemical structure of organic compounds, their capacity can be estimated or forecast from the C_{theor} which is calculated using the following eqn (1).

$$C_{theor} = \frac{n \times F(Cmol^{-1})}{M_w(gmol^{-1})} = \frac{n \times 96485(Asmol^{-1})}{M_w(gmol^{-1})} = \frac{n \times 26801}{M_w}(mAhg^{-1}) \qquad \text{eqn (1)}$$

where C_{theor}, n, F and M_w respectively mean the theoretical specific capacity, the transferred electron number in each structural unit, the Faraday constant and the molecular weight of the structural unit. Two ways to improve the C_{theor} are reducing the M_w of the structural unit and adopting multi-electron reactions.

1.5.2 Quinones

The class of carbonyl compounds has been extensively studied in the field of organic matter since the 1970s and 1980s.[30,51,52] Basically, the carbonyl compounds undergo reversible one-electron reduction to form a radical monoanion as displayed in Scheme 1-1. They can involve more electron reactions by further direct conjugating the carbonyl groups to form multivalent anions. Quinones and their derivatives are most widely studied molecules for LIBs due to their good electro-activity with two-electron reduction (Figure 1-8).[45,50,67,68] They provide a high C_{theor} (up to 500 mAh g^{-1}), and fast and reversible redox reactions.[45,69] Quinones naturally occur, involved in the electron transport of cofactors in photosynthesis and respiratory processes.[61]

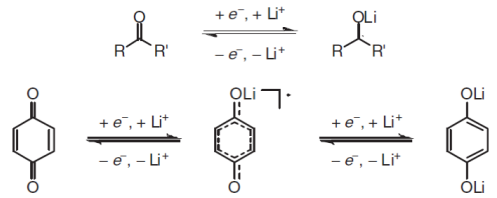

Scheme 1-1 Mechanism for reversible reduction of general carbonyl compounds (up) and quinone (down). Reprinted by permission.[51] Copyright 2012, Wiley-VCH.

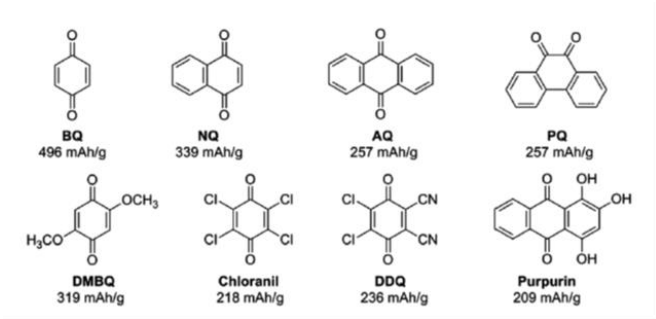

Figure 1-8 Conjugated carbonyl groups in quinones and their C_{theor}: benzoquinone (BQ), naphthoquinone (NQ), anthraquinone (AQ), phenanthraquinone (PQ), 2,5-dimethoxy-1,4-benzoquinone (DMBQ), 2,3,5,6-tetrachloro-1,4-benzoquinone (chloranil), 2,3-dichloro-5,6-dicyano-1,4-benzoquinone (DDQ), and 1,2,4-trihydroxyanthraquinone (purpurin). Reprinted by permission.[52] Copyright 2013, Royal Society of Chemistry.

However, solubility in electrolytes, poor conductivity, and low voltage are the main drawback of small organic molecules. To address these problems, constructing organic molecules with a stable skeleton and good conductivity (e.g., conductive polymers and conductive carbons) reduce the dissolution in electrolytes of organic electrode materials. There have been many conducting polymers used as backbones such as PPy[55,70] and poly(3,4-ethylenedioxythio-phene) (PEDOT)[61,71] or conductive carbons[55,72] coupled with quinone as a pendant group. Another approach is the use of quinone polymer that is always completely insoluble in the electrolytes.[56,73] Figure 1-9 presents some polyquinone derivatives with their C_{theor}. Many polymers (e.g., PAQs, PVAQ, PPYT) exhibit excellent electrochemical performance such as high capacity close to the theoretical value, good cycling stability, high Coulombic efficiency and high rate capability. However, there are disadvantages of electrodes produced from polymeric materials including their low electronic conductivity, since they are mostly insulating materials. To fully utilize the active material, sometimes a conductive carbon is incorporated during the fabrication of the electrode, usually amounting to 30-60%. In situ polymerization of active material with conductive carbon is also a choice. Well fabricated electrodes with conjugated quinone-

based polymers are likely to achieve a high rate performance due to the fast reaction kinetics.[74]

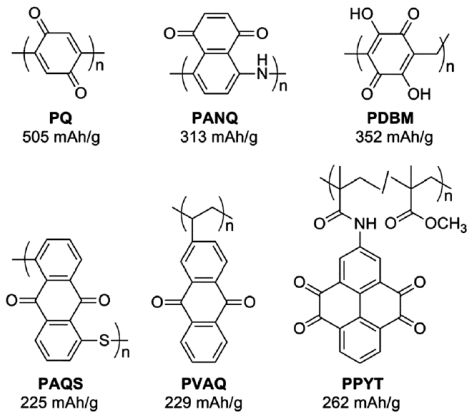

Figure 1-9 Typical polymer electrode materials based on conjugated carbonyl groups and their C_{theor}: polymeric quinone (PQ), poly(5-amino-1,4-naphthoquinone) (PANQ), poly(2,5-dihydroxy-1,4-benzoquinone-3,6-methylene) (PDBM), poly(anthraquinonyl sulfide) (PAQS), poly(2- vinylanthraquinone) (PVAQ), and polymer-bound pyrene-4,5,9,10-tetraone (PPYT).[52] Reprinted by permission. Copyright 2013, Royal Society of Chemistry.

Organic salts have emerged as a new class of conjugated carbonyl compounds. In order to reduce the solubility of organic compounds in organic electrolytes, salt formation is an alternative strategy through the coordination bond of Li metal (or other metal salts) with small organic molecules.[75-78] However, the influence of additional negatively charged oxide functions ($C\text{-}O^-$) induces a depletion of capacity during the charging/discharging process. A rearrangement of the coordination structure during the cycling process leads to gradual capacity loss. This is the main drawback for coordination polymer electrodes.[30,52,79]

However the synthesis of most organic electrode materials involves expensive and toxic reagents.[56,80] The physiological processes of ion transport and energy conversion of functional biomolecules, particularly quinone-based compounds, inspired researchers to develop green organic electrode materials. Many phenolic compounds or their derivatives widely occur in nature, e.g., dopamine, purpurin, flavins, tannin, and lignin. Their structure is mainly composed of phenolic or phenolate moieties that are well known as redox-active compounds. Therefore, they could be an ideal redox-active biomolecule-based electrode material for the next-generation of green and sustainable energy systems.

1.6 Lignin

1.6.1 Introduction and chemical structure

Wood, generally, consists of cellulose, hemicellulose, and lignin. Lignin is a plant cell wall component with the function of holding the cellulose/hemicellulose matrix together. It provides rigidity to the plant, protects against attack by microorganisms, and facilitates the internal transportation of nutrients and water. The chemical structure of lignin is constituted by an amorphous heterogeneous and highly cross-linked polymer of phenolic nature containing mainly three types of substituted phenols (monolignol monomers), namely, *p*-coumaryl, coniferyl, and sinapyl, alcohols (Figure 1-10). They are present in the form of *p*-hydroxylphenol (HP), guaiacyl (G) and syringyl (S) moieties in the lignin structure, respectively. Produced by enzymatic polymerization, lignin possesses a various number of functional groups and linkages between the monolignols such as ether and carbon-carbon bonds forming a 3-D network.[81-84]

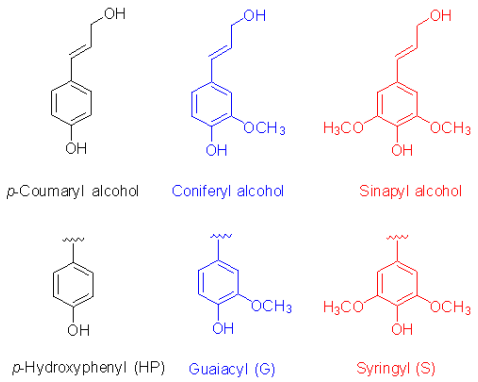

Figure 1-10 Three typical monolignol monomers and their corresponding structures in lignin.

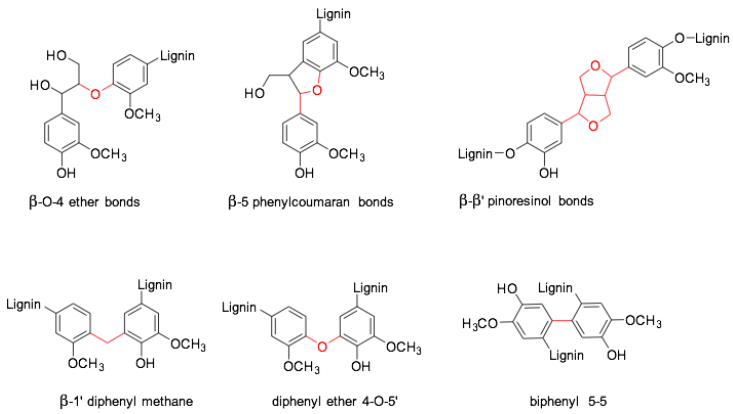

Figure 1-11 Common linkages found in lignin.[82,83,85]

Approximately 50% of the structure of lignin is formed by aromatic compounds with common linkage patterns as shown in Figure 1-11. The dominant linkage in lignin is the β-O-4 linkage.[83] The monolignol composition of lignin varies according to its original plant source. For instance, hardwood lignin has roughly equal amounts of coniferyl and sinapyl alcohol, while about 90% of softwood lignin is composed of coniferyl alcohol.[85,86] Due to more methoxy groups on the aromatic rings the formation of 5-5 (carbon-carbon bond) or dibenzodioxocin (carbon-oxygen and carbon-carbon bonds) linkages may be prevented in the hardwood lignin structure. A more linear structure results for hardwood lignin compared to softwood lignin (Figure 1-12). All lignin possesses a high aromatic content, giving it hydrophobicity and poor solubility in water at acidic or neutral pH. However, it may be dissolved in an alkali solution (depending on the isolation process, see below), or in many organic solvents.

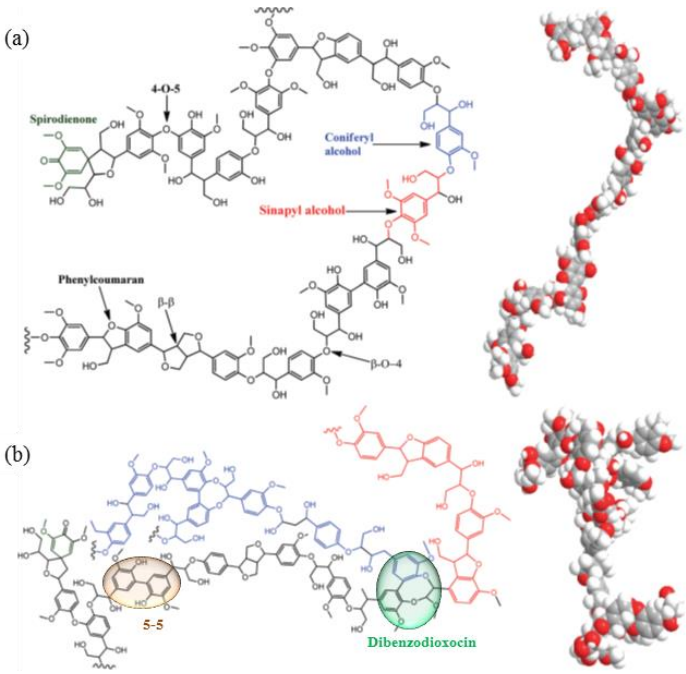

Figure 1-12 Typical structure (left) and molecular model (right) of lignin derived from hardwood (a) and softwood (b). Reprinted by permission.[85] Copyright 2015, Royal Society of Chemistry.

1.6.2 Isolation processes

During the chemical pulping processes, lignin is separated from cellulosic fibers to produce a suitable pulp for the paper manufactory and other related products.[87-89] About 98% of the lignin is burned onsite to provide steam for heat and power production.[90] Besides the influence from its botanical source, the physicochemical properties (e.g.,

molecular weight distribution, solubility, thermal properties) of lignin mostly depend on the isolation processes, also widely known as the pretreatment method. The soluble lignin products obtained from the chemical isolation methods are generally known as technical lignins. They are formed by a partial cleavage of lignin bonds, particularly ether bonds, as well as the incorporation of different functional groups onto the native lignin structure. In addition, side reactions also occur (e.g., intramolecular condensation) further increasing the complexity of the structure of isolated lignin. The most common isolation processes that are commercially available used to recover the lignin will be described. There are other isolation methods of chemical treatments such as soda, organosolv, hydrolysis, ionosolv, and ionic liquid methods to yield different properties of technical lignins, but these exceed the purpose of this discussion.

1.6.2.1 Kraft process

The Kraft lignin process originated in the early 1930s,[90] so called because of the superior strength of the resulting paper (Kraft meaning 'strength' in German).[91] It is the most predominant chemical pulping technique (about 85% of total world lignin production) and based on the use of sodium hydroxide and sodium sulfite. Both act as nucleophiles to break lignin-carbohydrate linkages. The process is performed at a temperature of around 170 °C for 2 hours in an alkali aqueous solution (Scheme 1-2), known as white liquor, of wood chips. Two main reactions take place under these conditions: the cleavage of α- and β-aryl ether bonds and condensation through the Michael addition of external sulfide and hydroxide anions. Another condensation occurs simultaneously by the addition of internal nucleophile species such as carbanions derived from phenolic structures yielding side reaction products.[92,93] As a result, the so-called dark or black liquor is obtained, containing smaller water/alkali-soluble fragments.[88] Kraft lignin is then precipitated by acidification. Normally, Kraft lignin contains a low amount of sulfur (less than 1-2%). Kraft lignin possesses several characteristic features which differ substantially from its native lignin (Figure 1-13). It contains a large amount of phenolic hydroxyl groups due to the large amount of β-aryl bond cleavage during cooking. The amount of biphenyl and other condensed structures increases as a function of the cooking time.[94] This process provides lignin with incorporated aliphatic thiols which are hydrophobic and which have a low molecular weight of between 1000 and 3000 g mol^{-1}.[95,96]

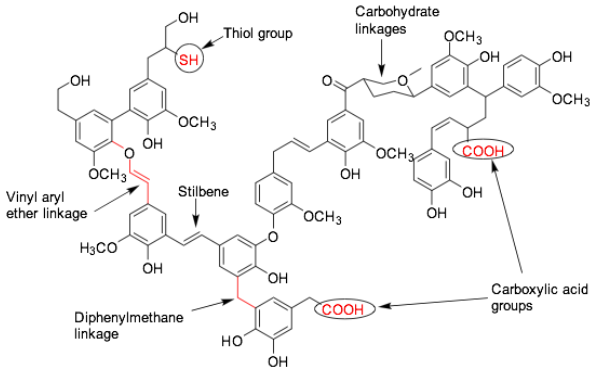

Figure 1-13 Model of the characteristic structure of the pine Kraft lignin.[90]

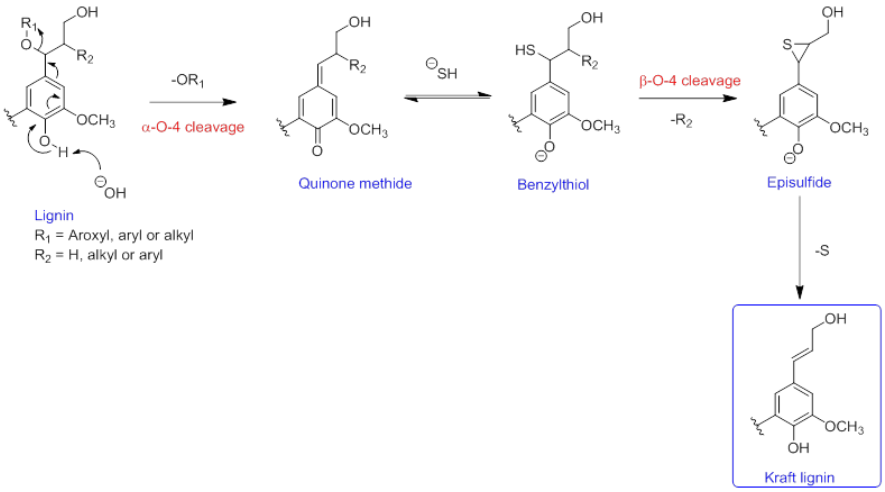

Scheme 1-2 The main reactions involved in the Kraft lignin process in alkali medium.[88,90,97]

1.6.2.2. Sulfite process

Lignosulfonates are obtained as the byproduct of sulfite pulping, which is the oldest pulping method with the first commercial sulfite pulp mill dating back to 1874.[90] The process is similar to the Kraft process, except it is conducted in acidic medium. It relies on various salts of sulfurous acid to extract the lignin from wood chips. The two main reactions during sulfite cooking are fragmentation and sulfonation with the temperature in the range of 140 ºC-160 ºC. Lignosulfonates are water-soluble, anionic polyelectrolyte polymers with sulfonate groups (sulfur content around 5%) present in their aliphatic side chains (Figure 1-14). They also have a higher molecular weight than Kraft lignin and a broad dispersity.[89,95]

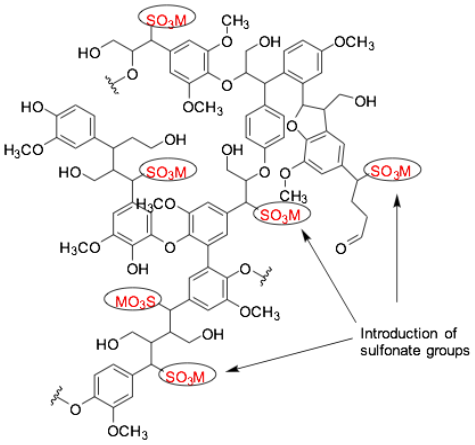

Figure 1-14 Model structure of lignosulfonate; M is metal ions.

1.6.3 Applications

As mentioned earlier, a large quantity of the lignin produced yearly around the world is considered waste product. Lignin is normally used directly as a fuel or as an additive to fuels due to its remarkable heating value or as an additive in bio-mass materials. In artificial fire logs, the addition of lignin into the cellulose materials with propane-1,3-diol can improve flame properties. Lignin is able to act as a substitute for gasoline/diesel fuel (pyrolysis oil production from lignin).[98-100] The use of lignin in various applications can potentially give the material higher value than simply burning it for heating energy. The diversity of properties of technical lignins leads to a diversity of opportunities for broad applications as summarized in Figure 1-15.[90] As evident in the structural model of lignin, it possesses many hydroxyl groups, particularly phenolic hydroxyl groups. So, lignin is known as a scavenger for free-radicals and useful for efficient antioxidant, antibiotic, and antitumor activities.[90,101,102] Lignin is applied in agriculture as binder for food pellets for feedstock, insoluble dietary fibers, additives for anti-lumping in fertilizers, and fertilizer, pesticides/herbicides controlled release.[103,104] Being a chelating agent, the use of lignin for heavy-metal removal in natural water resources or wastewater from many industries is another potential application.[105-108]

Lignin can be incorporated into polymers as a macromonomer (similar functional groups to the monomers used), or as an additive (no reaction with monomers). In the case of additives, the antioxidant properties of lignin are used to protect polymers from oxidation, light, or temperature, e.g., in rubbers, polyalkenes, polyesters, and other synthetic polymers.[90]

Figure 1-15 Various application fields of lignin.[109,110]

The incorporation of lignin into other polymers or copolymers has been employed in order to improve the mechanical properties such as lignin-reinforced polystyrene (PS),[111] poly(ethylene terephthalate) (PET),[112] polypropylene (PP),[113] and polyacrylonitrile (PAN)[114] composite for various applications, e.g., stabilizing agents, lubricants, coatings, plasticizers, and surfactants.[81,90,115] Replacement of a reagent in polymer composites with lignin not only reduces price but also improves environmental friendliness. For example, phenol is replaced by lignin in phenol-formaldehyde (PF) polymer composites for coating and adhesive applications in plywood, chipboard, particleboard, and so on.[90,116-118] In the field of bioplastic materials, lignin-polylactic acid (PLA) composites[119] and lignin-poly(ε-caprolactone)-based polyurethane[120] are used as biodegradable foam materials. In order to operate lignin for high-chemical value products, fragmentation or depolymerization processes are employed to convert the native or technical lignins into useful aromatic compounds, particularly phenolic compounds such as cresols, catechols, resorcinols, quinones, vanillin, or guaiacols. These hydroxylated aromatic compounds are the effective starting material for the synthesis of polymers, pharmaceuticals, and additives in the food and beverage industry.[90,96,121-123]

In the field of energy storage applications, lignin has been applied in various functions such as additives and active materials in electrodes (Figure 1-16). For example, lignosulfonates are a component of battery additive in lead-acid batteries. They improve battery performance at low temperature and at high discharge rate.[90,124] Lignin is also used as binder material in LIBs.[125,126]

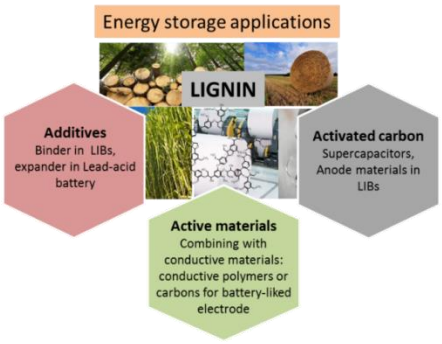

Figure 1-16 List of lignin's utilization in energy storage applications.

Lignin based carbon materials are mostly used in the synthesis of anode materials for LIBs[127-132] and supercapacitors.[133-143] Their high carbon content, availability and aromatic-rich chemical structure, combined with low cost and sustainability allows for the production of activated carbons, fibers, nanostructured and highly ordered carbons from different types of lignins.[129,143-145] Typically, there are two approaches to synthesizing lignin-based carbon: electrospinning[136-138,140] and template[135,139,146] or template-free[134,141,147] methods. There are numerous studies on lignin-based carbon materials for supercapacitors. For instance, Hu *et al.*[136] reported on the preparation of lignosulfonate-based carbon fibers through electrospinning and chemical activation. The hydrophilic and high surface area carbon fibers revealed large-size nanographites and good electrical conductivity leading to good electrochemical performance (344 F g^{-1} at 10 mV s^{-1}). Saha *et al.*[139] prepared mesoporous carbon using Pluronic F127 as a template coupled with physical and chemical activation to improve porosity and achieved capacitance in the range of 92-102 F g^{-1}. Zhang *et al.*[147] prepared lignin-based carbon *via* a template-free method using KOH particles acting as both the template and activating agent obtained a capacitance of 165 F g^{-1} at 0.05 A g^{-1}. However, porous carbon materials have limited energy densities as a result of the EDL capacitive mechanism, where the charges are stored physically through ion-adsorption at the electrode interfaces.

On the other hand, lignin can be combined with conducting materials such as conducting polymers and conductive carbon to fabricate a battery-liked electrode. Due to the poor electronic conductivity of lignin, constructing with conducting materials is a strategy to improve lignin's electrochemical performance. Milczarek *et al.* first presented a new kind of battery cathode created from lignin by the formation of electroactive quinone functionalities, which can be oxidized and reduced during cycling.[148] It was prepared by

the electrochemical polymerization of pyrrole in lignin-based solution. The synergic combination of conducting polymers and lignin biocomposites was described as forming an interpenetrating network of lignosulfonate and PPy. They proposed anion (ClO_4^-) insertion as first occurring in PPy, converting to PPy/ClO_4^- which provides a capacitive-like behavior without pronounced peaks, suggesting only the fast insertion/de-insertion of the anion into/from the PPy polymer. Then the redox activity (quinone/hydroquinone couples) in lignosulfonate is readily accessible. The obtained specific charge capacity was *ca.* 70-75 mAh g^{-1}. They found that the charge storage capacity was strongly influenced by the film thickness of composite electrodes due to diffusion limitations. Later research on PPy/lignin composites attempted to enhance the abundance of quinone groups through various strategies such as choice of alternative lignin with different S/G ratios (42 mAh g^{-1}),[149,150] introduction of extra quinones by using anthraquinone sulfonate (AQS) (180 mAh g^{-1}) during the formation of the hybrid material,[151] introduction of monolignol phenolic units through phenolation of Kraft lignin (69 mAh g^{-1}),[152] and preparation of a synthetic lignin model from homopolymers and copolymers of monolignols (94 mAh g^{-1}).[153] Even though the addition of small quinone molecules can reach a high charge storage capacity, they will diffuse out of the electrode during operation resulting in capacity loss. The complexity of the PPy chain configuration and conformation together with undefined structure, reactivity, and possible impurity of lignin derivatives result in many uncertain parameters. These parameters such as redox species, conductivity, and accessibility to the phenolic groups might affect the charge storage capability of the PPy/lignin system.[5,149-155] Other conducting polymers, such as PANI[156] and PEDOT,[157] have been used as alternatives to prepare electrodes with lignosulfonates by electrochemical polymerization or oxidative chemical techniques.

Due to their excellent electronic, mechanical, and electrochemical properties, and high specific surface area, conductive carbons have attracted attention as an alternative choice for the construction of a lignin electrode in order to obtain the synergetic effects between the redox active polymer sites and a highly conducting carbon support. Adsorption of organic molecules on the surface of carbon materials can take place by van der Waals, π-π stacking, and electrostatic interactions. CNTs can act as a network transporting electrons from the charge collector surface to redox active moieties. The interaction in CNT-lignin composites is non-covalent strong π-π stacking. With the large surface area of CNTs, the surface coverage with redox active species increases with the consequence of enhancing

the accessibility of active sites for electrolyte ions leading to the improvement of the charge storage capability. Milczarek *et al.*[5] presented the use of CNTs surface-functionalized with Kraft lignin, which resulted in a redox active biofilm of lignin randomly spreading throughout the surface of CNTs and thus causing an increase of electrode material wettability. The total charge storage was a combination of EDL charge storage of the CNTs and faradaic charge storage gained by lignin-derived quinone functionalities which showed good cycling stability. Rębiś *et al.*[153] fabricated CNTs with a synthetic lignin model providing a capacity of 72 mAh g^{-1}. The CV profile of CNTs/lignin exhibited a typical EDL capacitive response without pronounced redox peaks, which is characteristic for redox quinone moieties with different chemical environment and as such result of the complex nature of the parent lignin.[5,153] They should not be counted as pseudocapacitive materials following the definition of pseudocapacitance.

Graphene is an outstanding two-dimensional carbon material with exceptional electric conductivity and mechanical strength, and high specific surface area (2630 m^2 g^{-1}).[158,159] Lignin can be used to prevent the aggregation of graphene sheets by re-stacking. The utilization of Lignin/graphene hydrogel fabricated from a mixture of lignin and graphene oxide (GO) through a hydrothermal process, obtaining 3-D porous composite hydrogel was proposed by Xiong *et al.*[160] The composite hydrogel electrodes showed a maximum specific capacitance *ca.* 550 F g^{-1} with excellent rate capacity and cycling stability. Kim *et al.*[6] presented a series of lignin hybridized with reduced graphene oxide (RGO) nanosheets which were prepared by the reduction of amphiphilic GO sheets well-covered by lignin. Strong binding between lignin and RGO sheets occurs through π-π stacking and hydrophobic interactions resulting in an electron conducting hybrid electrode. They reported pseudocapacitor performance with a good rate and cycling stability. Due to the synergizing effect of the reversible redox charge transfer of quinone and the interplay with electron-conducting RGOs, the electrodes achieved a maximum capacitance of 432 F g^{-1} which is close to C_{thero} ~482 F g^{-1}.

*The results on this chapter based on already published material: Chaleawlert-umpon, S., Berthold, T., Wang, X., Antonietti, M., Liedel, C. "Kraft Lignin as Electrode Material for Sustainable Electrochemical Energy Storage" Adv. Mater. Interfaces. 2017, *4(23)*, 1700698.

2. Kraft lignin-carbon composite for sustainable cathode materials

2.1 Background and objective

As mentioned earlier, lignin is composed of phenolic groups. The electrochemistry of lignin is based on electroactive quinone/hydroquinone couples which can be generated by the demethylation of aromatic methoxy groups (Scheme 2-1). Quinone/hydroquinone couples are an example of organic redox systems occurring in phenolic-type compounds in nature (e.g., humic acids, flavonoids, tannic acid, and dopamine).

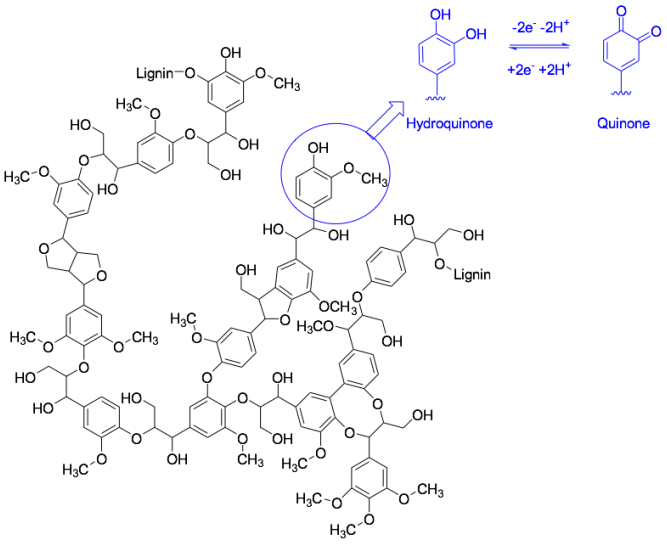

Scheme 2-1 Lignin structure with redox reaction occurring on quinone/hydroquinone couples. Reprinted by permission.[161] Copyright 2017, Wiley-VCH.

In aqueous acidic solutions, quinone/hydroquinone couples generally provide a reversible single step two-electron two-proton redox reaction ($2e^-/2H^+$) in which the reduction potential varies with pH following the Nernstian manner.[5,157,162,163] This means that two electrons and two protons are stored in a structure of 6 carbon and 2 oxygen atoms, giving a charge density of 2 Faraday per 108 g, *i.e.*, 1787 C g^{-1} or 496 mAh g^{-1}. This is a favorable value compared with standard electrochemical systems such as lithiated carbon materials (344 mAh g^{-1}), and the olivine $FePO_4$ system (170 mAh g^{-1}).[5]

As mentioned in Chapter 1.6.3, lignin has insulating characteristics. In order to improve its applicability as an electrode material, many studies have been conducted combining lignin with conducting polymers to improve charge transfer. However, many drawbacks of using conducting polymer additives have been reported. First is the degradation of the polymer during cycling leading to poor cycling stability.[154] The conductivity of the added polymer, e.g., PPy, may also be insufficient providing poor rate capabilities as well as self-discharge and inadequate charge storage density due to doping with small and mobile counteranions.[153,155] Second, even though, electrosynthesis can provide an effective and convenient one-step approach to the incorporation of lignin into a conducting polymer film, the use of toxic organic solvents or high acid concentrations during the polymerization process may be of concern in environmental issues.[149,150,152] Third, the high cost of monomers compared to the cost of the lignin biopolymer may limit the scalability. Finally, analysis of the composite materials is complicated and the mass ratio of the component is difficult to clarify, if not unknown, which means further improvements to charge storage capacity are difficult.[154,157]

Carbon materials are an alternative option to facilitate the electronic conductivity of lignin electrodes. The use of carbon material composites with lignin also provides the possibility to control the composite fraction in the final hybrid material. Thus, further improvement of the capacity by tailoring the mass ratio of all components is facile. Owing to their excellent chemical stability, especially in contrast to conducting polymers, composite electrodes with conductive carbon materials are able to perform in high electrolyte concentrations to reduce the influence of ion diffusion parameters in the system. Lignin with various conductive carbon materials such as CNTs[5] and RGO[6] incorporated was prepared for battery-like charge storage. This faradaic process features distinct redox peaks in cyclic voltammetry experiments, which are sometimes mistaken for pseudocapacitance.[15] Concerning sustainable, safe, and "green" energy storage devices, uncertainty about the health and safety aspects of CNTs and RGO limits their applications. Not only are they relatively expensive, but also large scale production still remains challenging.[159,164,165] Other conductive carbon additives have been synthesized from sustainable and renewable resources at lower cost.[166] Many researchers also reported using lignosulfonate as an electrode component, the production of which is gradually decreasing worldwide.[9] In contrast, since the emergence of the modern Kraft process, Kraft lignin has become increasingly available as a low-cost and abundant material.[167]

The aim of this chapter is to fabricate a composite electrode from readily available Kraft lignin and sustainable conductive carbon with typical blending techniques, and investigate the contribution of non-faradaic and faradaic processes to its charge storage properties. This research focuses on the influence of lignin loading and the carbon surface area on electronic properties and the ionic conductivity of the obtained electrode material in order to increase understanding of the desired lignin properties for electrochemical energy storage and the synergistic effect between lignin and conductive carbon. The surface morphology and distribution of the different electrode films are evaluated by SEM coupled with EDX. Generally, not only capacitive charge storage but also battery-like charge storage often exhibits a rectangular profile as the background in cyclic voltammetry experiments.[54,61,148,168,169] The Kraft lignin-carbon composite cathode, which combined both battery-like and capacitive-like charge storage behavior, is investigated by cyclic voltammetry and galvanostatic charge/discharge measurements to analyze the synergic combination of the lignin-carbon composite electrode. Cycling stability is performed to prove practical applicability.

2.2 Electrochemistry of Kraft lignin-carbon composites

The Kraft lignin-carbon composites were fabricated by mixing Kraft lignin and conductive carbon with different surface areas (167 m^2 g^{-1}, C^L and 858 m^2 g^{-1}, C^H) with 10 wt% of PVDF (binder) by ball-milling and film casting onto a graphite sheet (current collector). The obtained electrodes were used as working electrodes (WE) (Figure 2-1 (a)). For measurement, a three-electrode system was set up as displayed in Figure 2-1 (b) equipped with Ag/AgCl (KCl^{sat}) as a reference electrode (RE) and platinum wire as a counter electrode (CE) with 0.1-3 M $HClO_4$ aqueous solution as an electrolyte.

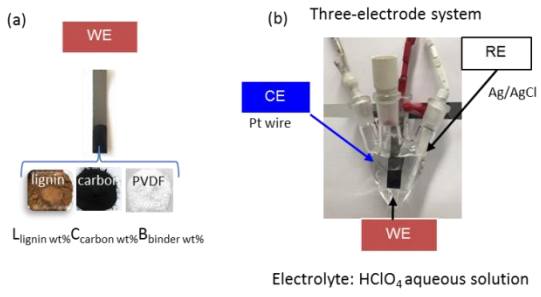

Figure 2-1 (a) electrode composition and (b) three-electrode system set up.

Two ratios of Kraft lignin and carbon were prepared, one using equal amounts of carbon and lignin, the other using less lignin than carbon. Compositions are listed in Table 2-1. The used ratios are comparable to other redox active composites for battery prototypes.[30]

Table 2-1 List of Kraft lignin-carbon composite samples.

Kraft lignin (wt%)	Carbon (wt%)	Binder (wt%)	Type of carbon	
			C^L	C^H
45	45	10	$L_{45}C_{45}{}^{L}B_{10}$	$L_{45}C_{45}{}^{H}B_{10}$
15	75	10	$L_{15}C_{75}{}^{L}B_{10}$	$L_{15}C_{75}{}^{H}B_{10}$

Their surface morphologies were analyzed by SEM as presented in Figure 2-2. All composite samples showed porous morphologies with unidentified individual components.

To observe the distribution of each composition, EDX of SEM images was employed on the $L_{15}C_{75}{}^{L}B_{10}$ and $L_{45}C_{45}{}^{L}B_{10}$ samples (Figure 2-3). It was not possible to see individual lignin and carbon particles since both of them mix well together during electrode fabrication. In the case of the binder, its distribution differs from lignin and carbon to hold the mixed lignin-carbon particles together.

All samples (as listed in Table 2-1) were investigated by CV measurements. Figure 2-4 presents the total capacity of all samples increasing with $HClO_4$ concentration.

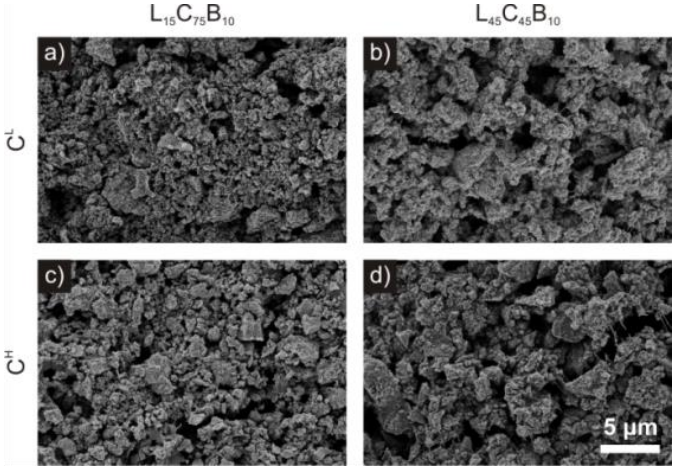

Figure 2-2 SEM micrographs showing the surface of composite electrodes a) $L_{15}C_{75}{}^{L}B_{10}$; b) $L_{45}C_{45}{}^{L}B_{10}$; c) $L_{15}C_{75}{}^{H}B_{10}$; d) $L_{45}C_{45}{}^{H}B_{10}$. The scale bar in d) applies to all sub-figures. Reprinted by permission.[161] Copyright 2017, Wiley-VCH.

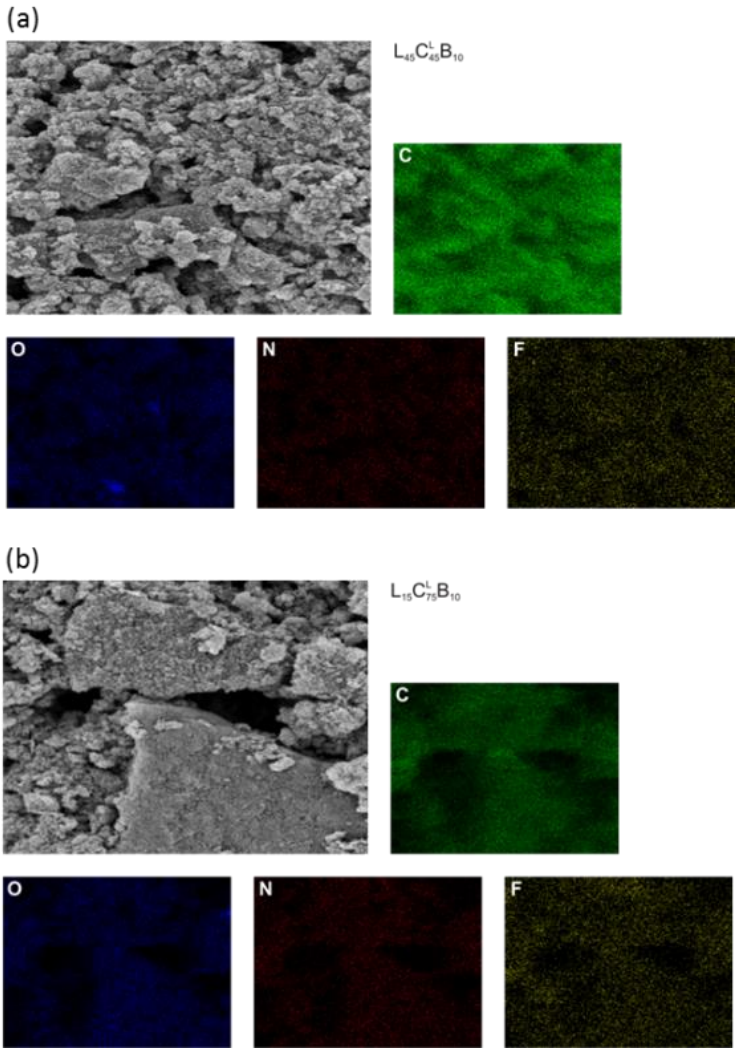

Figure 2-3 EDX data for (a) $L_{45}C_{45}{}^{L}B_{10}$ and (b) $L_{15}C_{75}{}^{L}B_{10}$ electrodes including the elemental distribution of carbon, oxygen (present mainly in lignin), nitrogen (present mainly in N-doped conductive carbon), and fluorine (present mainly in the binder). Reprinted by permission.[161] Copyright 2017, Wiley-VCH.

Comparing samples with the same conductive carbon, C^{L}, both compositions show almost the same capacity between electrolyte concentrations of 0.1-3 M. This indicates that capacity is independent of the compositions. In the case of C^{H}, a significant capacity difference was revealed. The low lignin content exhibits the highest capacity. Only at the highest electrolyte concentration, the capacity values for the low and high lignin content (with C^{H}) are almost the same. This may be explained by the formation of a layer of lignin on the larger surface area of conductive carbon. A thin layer of lignin is formed on the conductive carbon surface for the less lignin composite sample. The thinner lignin film facilitates charge transfer by a shortened pathway from insulating lignin to conductive carbon. In this case, it may be possible that the accessibility of redox active sites in lignin

for electrolyte ions is improved. However, increasing capacity with acidic aqueous electrolyte concentration indicates that the electrochemical performance strongly depends on the concentration of ions in the system as expected for a proton-dependent process.

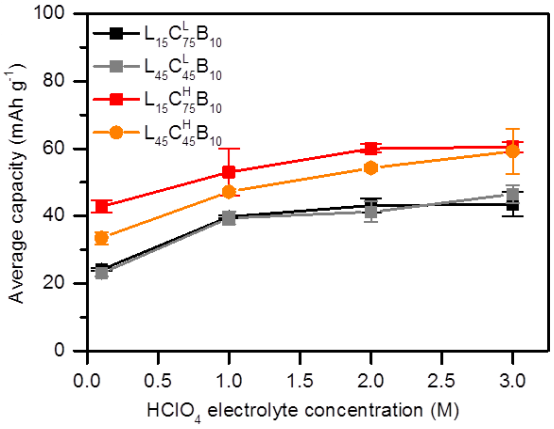

Figure 2-4 Capacity of different composite electrodes with various concentrations of the electrolyte, measurements at 5 mV s^{-1}. Reprinted by permission.[161] Copyright 2017, Wiley-VCH.

Figure 2-5 presents the CV profiles of all samples. It also reveals the similarity of the CV curves of neat conductive carbon and the rectangular background in the CV curves of the composites. This indicates that the total specific surface area in the composite systems does not significantly change even if lignin film forms upon the surface of the conductive carbon. This information also supports the assumption of the formation of a thin lignin film on the carbon surface.

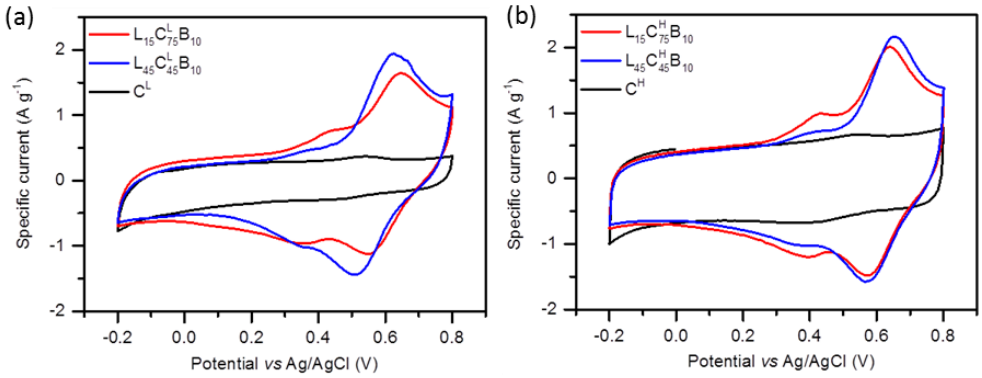

Figure 2-5 Cyclic voltammograms of composite electrodes and comparable electrodes without lignin as indicated. (a) Electrodes featuring low surface area conductive carbon C^L; (b) electrodes featuring high surface area conductive carbon C^H**,** measurements in 1 M $HClO_4$ at 5 mV s^{-1}. Reprinted by permission.[161] Copyright 2017, Wiley-VCH.

Furthermore, cyclic voltammograms exhibit a clearly observable difference between faradaic and non-faradaic charge storage contribution, resulting from the redox active

groups and the electrochemically active surface of the used lignin and carbons, respectively. For visualization, Figure 2-6 (a), which is the resulting cyclic voltammogram (CV) corresponding to the $L_{45}C_{45}{}^{L}B_{10}$ composite, shows a large separation of the oxidative and reductive scan with a couple of redox peaks and reveals the influence of EDL and faradaic charge storage. The peaks are separated from the rectangular area (see dashed line) indicative of EDL. The two redox peaks are revealed around 0.4 V and 0.6 V which is in good agreement with quinone/hydroquinone conversion in lignin. The main peak at 0.6 V is attributed to G groups and the small peak around 0.4 V is indicated as being caused by S groups.[150,153] As obtained from ^{31}P NMR measurements (Figure 2-6 (c)) and listed on Table 2-2, the amount of S groups (0.48 mmol g^{-1}) is lower than G groups (3.29 mmol g^{-1}, included G and C5 substituted G together) which is in good agreement with their peak area contributing to a lower influence to charge storage in the Kraft lignin-carbon composite.

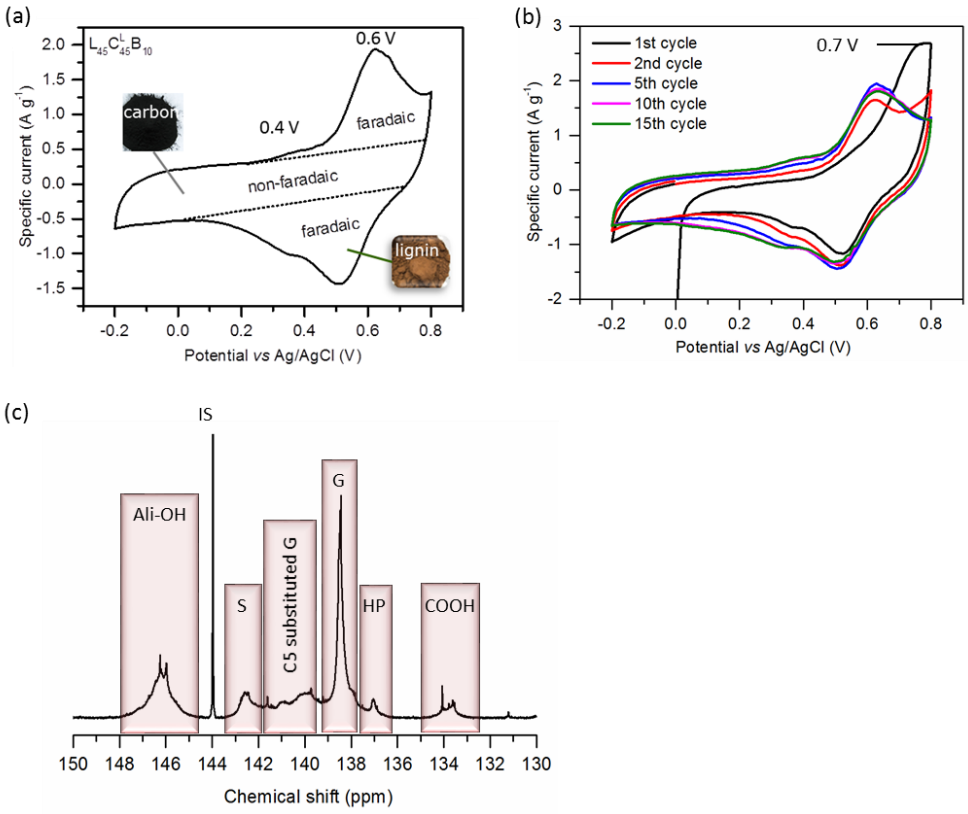

Figure 2-6 Cyclic voltammogram of an $L_{45}C_{45}{}^{L}B_{10}$ working electrode at 5 mV s^{-1} in 1 M $HClO_4$ with indicated contributions by faradaic and non-faradaic processes to charge storage (a, reprinted by permission,[161] Copyright 2017, Wiley-VCH) and with first and latter cycles (b). ^{31}P NMR spectrum of Kraft lignin after phosphitylation showing the peaks of aliphatic hydroxyl (Ali-OH) functionalities, the internal standard (IS), S, G, HP groups and carboxylic (COOH) functionalities (c). Adapted by permission.[161] Copyright 2017, Wiley-VCH.

The position of a given monolignol on the potential scale in CV depends on the number of oxygen containing groups substituted on the aromatic ring. For the S groups, which possess a higher substitution degree, redox couples with lower potential values are obtained due to the influence of electron donating groups.[150,153] In the first scan an irreversible oxidation wave is evident at 0.7 V (Figure 2-6 (b)) which is attributed to the demethylation of methoxy phenol groups followed by the development of quinone/hydroquinone redox couples positioned at lower potentials in subsequent scans.[153,170]

Figure 2-7 presents the total capacity and charge storage contributions of $L_{45}C_{45}{}^{L}B_{10}$ composites as derived from CV measurements in various electrolyte concentrations. The total capacity of the composite improves with increasing electrolyte concentration, indicating the significant proton-dependency of the process. Considering the individual charge storage contribution, non-faradaic contribution remains mostly unchanged with increasing electrolyte concentration. Most of the increase in total charge storage capacity results from the faradaic contribution. This might be the case due to the increasing accessibility of electrolyte ions to redox active sites in lignin, leading to faradaic charge storage improvement.

Table 2-2 List of amount of hydroxyl functional groups in Kraft lignin calculated by ^{31}P NMR Figure 2-6 (c).

Amount of hydroxyl groups (mmol g^{-1})					
Ph-OH				Ali-OH	
S	G	C5 substituted G	HP	Ali-OH	COOH
0.48	2.13	1.16	0.2	1.36	0.25

Even though high concentrations of electrolyte provide the highest capacity, 1 M $HClO_4$ was selected (because a higher concentration of $HClO_4$ may damage the electrode) to investigate the influence of the ratio of the lignin-carbon composite and surface area conductive carbon in the following experiments.

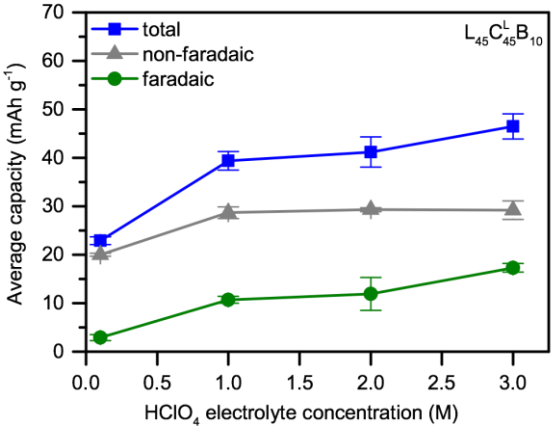

Figure 2-7 Capacity of $L_{45}C_{45}{}^{L}B_{10}$ working electrodes in different electrolyte concentrations and contributions to the capacity by faradaic and non-faradaic processes as estimated from cyclic voltammetry measurements at 5 mV s^{-1}. Reprinted by permission.[161] Copyright 2017, Wiley-VCH.

The charge storage contributions were determined from CV measurements as presented in Figure 2-8. Generally, using the higher surface area conductive carbon in composite samples exhibits higher non-faradaic charge storage (*ca.* 34-36 mAh g^{-1}) compared with using the lower surface area conductive carbon samples (*ca.* 25-29 mAh g^{-1}). For the same type of conductive carbon, the non-faradaic charge storage is within the same range, but the faradaic charge storage contributes to additional charge storage. These results indicate that the EDL charge storage ability of conductive carbon does not significantly decrease by covering the carbon surface with a thin lignin film. However, the capacity contribution of all composite samples using C^{L} is the same, indicating that the higher lignin content does not enhance faradaic charge storage. One possible explanation is the high content of lignin leading a thick film of lignin in either composition which causes the insufficient accessibility of electrolyte ions. This means the bulk of lignin does not contribute to the faradaic charge storage.

In contrast, the composite samples with C^{H} reveal the opposite result. The lower lignin content of the composite sample, $L_{15}C_{75}{}^{H}B_{10}$, provides higher faradaic capacity contribution. The explanation here is that the charge transfer and charge storage process are more efficient in the case of a composite with a thinner lignin film on a high surface area conductive carbon.[5,6] The better electronic conductivity in the composite electrode fabricated using a higher content of conductive carbon promotes a better electron transfer process between the graphite current collector and the electroactive sites of lignin. In addition, a low content of lignin on a high surface area conductive carbon causes the

formation of a thin film inducing even better ionic conductivity as a result of interfacial interaction between electrolyte ions and the redox active moieties in lignin. Using higher content of lignin in the composite causes the formation of a thicker film on the surface of conductive carbon leading to a less efficient charge transfer process and a resistance of ionic transfer at the electrode-electrolyte interface. As a consequence, the faradaic charge storage is less efficient.

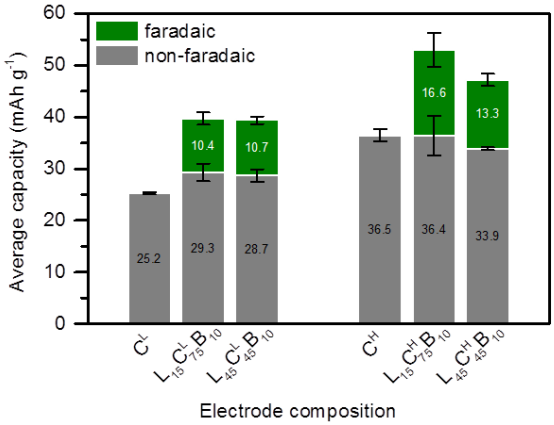

Figure 2-8 Faradaic and non-faradaic contributions to the total capacity as estimated from cyclic voltammetry measurements in 1 M $HClO_4$ at 5 mV s^{-1} of different composite electrodes as indicated. Reprinted by permission.[161] Copyright 2017, Wiley-VCH.

According to the theoretical charge density of quinones, they can store 2 Faradays per 108 g, or 496 mAh g^{-1}. S and G moieties in lignin give the same redox contribution as quinones. Thus, 1 mmol of S or G per weight of lignin gives a charge capacity of approximately 2 milliFaraday g^{-1} of lignin or 53 mAh g^{-1}, following the eqn (2).[148,150] The highest faradaic charge storage is obtained from the $L_{15}C_{75}{}^{H}B_{10}$ composite electrode at 16.6 mAh g^{-1} (total mass) or 111.1 mAh g^{-1} (lignin mass), approximately 55% C_{theor} of lignin (3.77 mmol g^{-1} of S and G groups, 200 mAh g^{-1} theoretical capacity, calculated by eqn (2)). This indicates that half of the electroactive site groups of lignin contribute to faradaic charge storage.

$$C_{theor\ of\ lignin}(mAhg^{-1}) = amount\ of\ S\ or\ G \times 53 \quad \text{eqn (2)}$$

Electrochemical impedance spectroscopy (EIS) was employed to determine the internal resistance and ion diffusion performance of the lignin-carbon composite. A Nyquist plot is shown in Figure 2-9 in the frequency range of 0.02 to 20,000 Hz, presenting the equivalent series resistance (ERS) which is the sum of system resistance performed at high-frequency.

The semicircle at the high to middle-frequency region is indicative of the charge transfer resistance of the electrode material, and the low-frequency region shows the Warburg resistance, indicative of the ion diffusion ability.

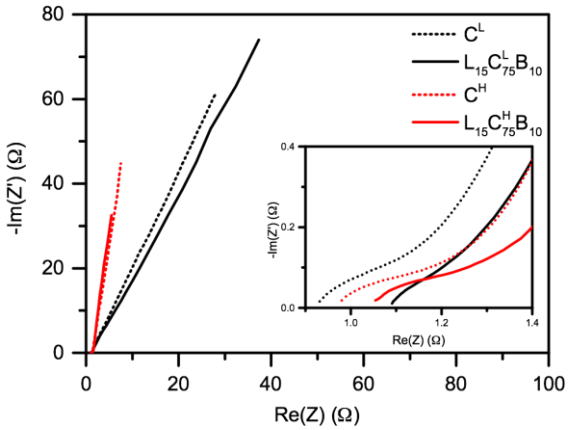

Figure 2-9 A Nyquist plot of composite electrodes and carbon electrode (without lignin). The insert shows the high frequency region enlarged. Reprinted by permission.[161] Copyright 2017, Wiley-VCH.

Small ESR values at 0.93 Ω and 0.98 Ω were observed from neat C^L and C^H electrodes, respectively while the corresponding lignin-carbon composite electrodes possess higher ESR values of 1.09 Ω and 1.05 Ω, respectively. This indicates the insulating influence of lignin inhibiting the electric conductivity of the composite electrode. Sample $L_{15}C_{75}B_{10}$, (with C^H) reveals a slightly larger semicircle at high frequency than the ones with C^L. This is attributed to the higher charge transfer resistance. In the low frequency region, the sloping line represents the Warburg impedance which is indicative of mass transfer. The composite with C^H has the least sloping line and thus facilitates ion diffusion. EIS data provide evidence of good mass transfer through the electrode/electrolyte interface due to the easy accessibility of the electrode surface and good conductivity of the composite electrode. This further supports the assertion that the formation of a thin layer of lignin on a high surface area conductive carbon leads to shortened pathways of charge transfer and the compensation of the insulating character of lignin. To further investigate the influence of the surface area of conductive carbon, the $L_{15}C_{75}B_{10}$ composite electrodes with different conductive carbons were subjected to galvanostatic charge/discharge performance tests at different current densities. Figure 2-10 summarizes the resulting curves. They significantly deviate from both a triangular shape and a plateau shape. This indicates the contribution of both redox reactions in lignin as well as the EDL charge storage of conductive carbon. Furthermore, the information obtained from the application of various current densities

exhibits a slow decrease of capacity at high current densities due to fast charge diffusion in electrode materials.

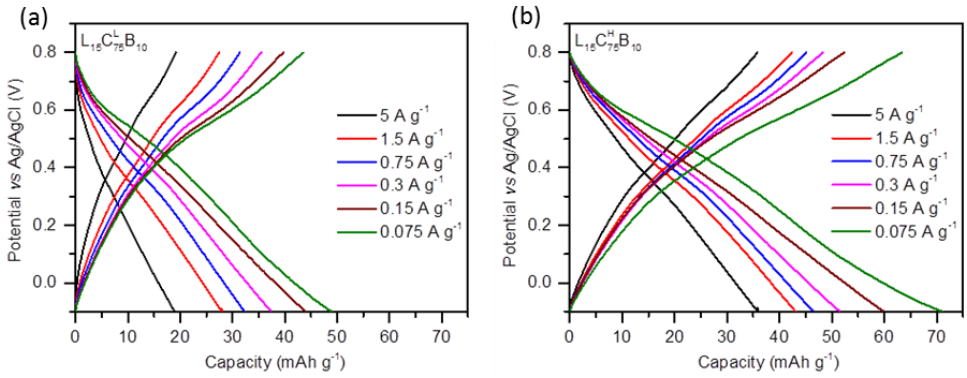

Figure 2-10 Galvanostatic charge/discharge curves at various current densities as indicated for (a) $L_{15}C_{75}{}^{L}B_{10}$ and (b) $L_{15}C_{75}{}^{H}B_{10}$ composite electrodes. Reprinted by permission.[161] Copyright 2017, Wiley-VCH.

The influence of the EDL charge storage of the conductive carbon is stronger than the battery-like charge storage of the lignin which leads to a belly slope like shape of the curve. These results are in good agreement with the charge storage contributions derived from the CV measurement described earlier. The decrease of the curve's slope is observed in the potential range of 0.3-0.6 V which is in good agreement with the potential of the reversible redox reactions present in lignin.

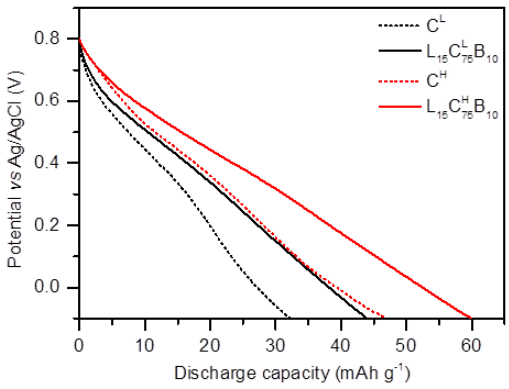

Figure 2-11 Galvanostatic discharge curves at a current density of 0.15 A g^{-1} for composite and carbon electrodes as indicated. Reprinted by permission.[161] Copyright 2017, Wiley-VCH.

To prove the influence of redox reaction on the charge storage capacity, the composite electrode without lignin was evaluated for comparison as seen in Figure 2-11. It is clear that a significantly lower capacity is achieved compared to the lignin-carbon composite electrodes which have additional charge storage by lignin. The composite samples with

high surface area conductive carbon as expected provide higher capacity than those with low surface area conductive carbon.

To more accurately evaluate their performances, the rate and cyclic capabilities for practical applications were tested by stepwise galvanostatic cycling measurement at various current densities as demonstrated in Figure 2-12 (a). Both composite electrodes show good rate performance. At about half of the low-rate capacity retained at the highest rate, and for 10 cycles at each discharge rate the capacity remained constant except in the first 10 cycles at 0.075 A g^{-1}. This may be attributed to the initial demethylation reactions as shown in Figure 2.6 (b). When the current density gets back to 0.075 A g^{-1}, the capacity is almost the initial one after the conditioning phase (around 74-77 mAh g^{-1}). The CV profile before and after stepwise galvanostatic cycling with different current density is presented in Figure 2-12 (b), indicating fully reversible charge/discharge behavior. It is found that a CV curve after cycling reveals significantly broadened redox peaks at around 0.4 V without significant capacity loss.

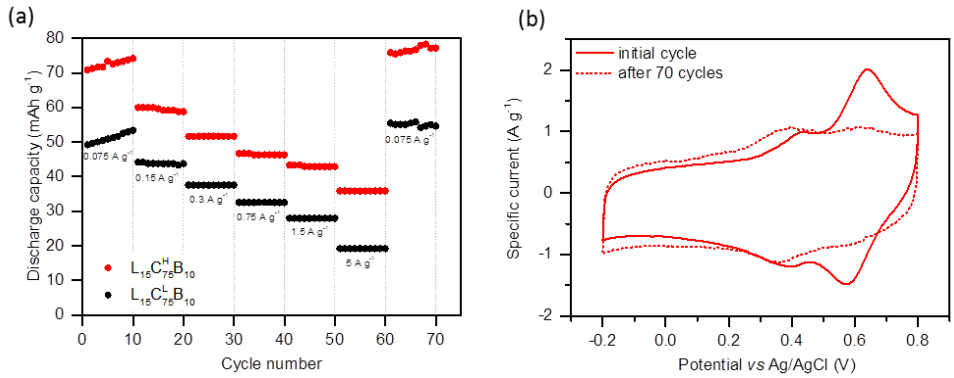

Figure 2-12 (a) Rate capability with cycling performance of $L_{15}C_{75}{}^{L}B_{10}$ and $L_{15}C_{75}{}^{H}B_{10}$ composite electrodes and (b) Cyclic voltammograms of $L_{15}C_{75}{}^{H}B_{10}$ working electrode before and after 70th galvanostatic cycling. Reprinted by permission.[161] Copyright 2017, Wiley-VCH.

The broadened redox-peak in the CV profile may indicate enhanced coupling between different electrochemically active groups in lignin. During the charge/discharge cycling, reorganization of the phenolic groups in lignin towards a stacking feature may be indicated. Consequently, the charge transfer between redox active groups in lignin polymer becomes more efficient. The shift towards lower potential may also indicate partial crosslinking which can increase the average number of phenolic groups per aromatic ring. In order to characterize the change of functional groups after cycling performance, FTIR was carried out as presented in Figure 2-13.

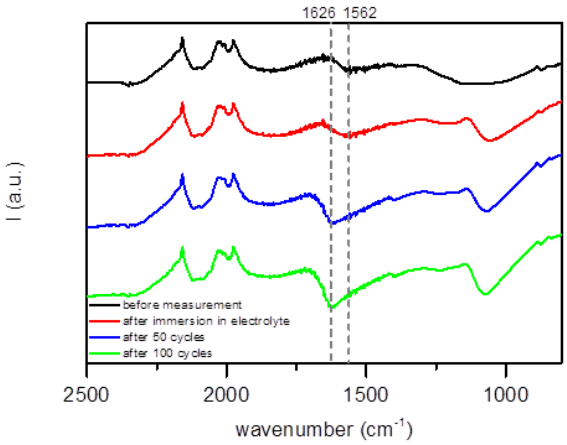

Figure 2-13 FTIR spectra of an $L_{15}C_{75}{}^{H}B_{10}$ working electrode before and after galvanostatic cycling. Reprinted by permission.[161] Copyright 2017, Wiley-VCH.

Because the composite electrode contains a high amount of carbon (75%), signal intensity is not clearly observed. Comparing the composite electrode before measurement and after immersion into the electrolyte, there is only one additional broad peak in the range of 1000-1250 cm^{-1} which could be attributed to the Cl-O stretching of the electrolyte. After the cycling measurement, a peak at around 1626 cm^{-1} appears which corresponds to C=O stretching in quinones. Aromatic stretching vibrations in the range of 1500-1600 cm^{-1} remain unchanged. This result indicates the presence of quinones after charge/discharge cycling for at least 50 cycles. Therefore, FTIR of the composite electrodes at varying stages of cycling can be used to support the stability of the electrode during cycling performance and the continued presence of the redox active sites after cycling even though the CV profile shows a broadened redox peak.

2.3 Conclusion

In summary, biopolymer electrodes from commercial Kraft lignin and sustainable conductive carbon were fabricated. The combination of lignin and carbon plays a key role in enhancing EDL capacitance with additional faradaic charge storage contribution. Since EDL charge storage mainly depends on the surface area and lignin is an insulator, the charge storage capability of their composite devices depends on the surface area and the mixing ratio between lignin and conductive carbon. The highest specific capacity of up to 80 mAh g^{-1} (total material mass) at discharge rate of 0.075 A g^{-1} from combined faradaic and non-faradaic capacity, is reached in the electrodes which are composed of a thin layer of lignin covering a high surface area conductive carbon. Therefore, we can conclude that

the relevant factors are high surface area, accessibility of redox active sites in lignin to the electrolyte, and good mixing during preparation to provide the highest charge storage capability of these biopolymer electrodes. These electrodes represent a promising alternative prototype of renewable and sustainable energy storage devices.

*The results on this chapter based on already published material: Chaleawlert-umpon, S. and Liedel, C. "More sustainable energy storage: lignin based electrodes with glyoxal crosslinking" J. Mater. Chem. A **2017**, *5*, 24344-24352.

3. Modification of Kraft lignin with dialdehyde crosslinkers for cathode materials

3.1 Background and objective

As mentioned earlier, lignin can be applied as an adhesive, one of the most investigated industrial applications, inspired by its natural function to glue and hold cellulose fibers together in plants. In several studies, lignin has been added to or even replaced broad resin products, such as polyurethane, phenol-formaldehyde (PF) and epoxy resins[171,172] in order to reduce health issues.

In battery electrode processing, a binder is a necessary component for holding all electrode components (active materials and conductive carbon additives) together and fixating them on a current collector. Ideally, a high adhesion ability between the electrode materials and the current collectors and a good electric-network formation ability between the active material and conductive carbon to facilitate electron transport and ion diffusion are required. Thus, the binder plays a crucial role in electrode fabrication. The impact of binders is not only apparent in the resulting mechanical property but also highly relevant for the cycling stability, safety and environmental impact of the devices.[173] So far, fluorinated polymeric binders, such as polytetrafluoroethylene (PTFE), PVDF, and perfluorosulfonic acid-PTFE copolymer (Nafion) are commercially available and widely used for LIBs and supercapacitors.[96,173] They exhibit excellent electrochemical stability and binding capability; however, some drawbacks have been recognized such as the limited surface activity to bind all electrode components, defluorinating side reactions releasing harmful products, difficult recycling, and high price.[126,174,175] In addition, their hydrophobicity is unfavorable for the wettability of the electrode with the electrolyte due to the ion-blocking property and insulating properties leading to high internal resistance.[176-178] Even the conventionally low amount of binder (*ca.* 5-10 wt%) often impedes porosity of the electrode surface. Various alternative binders such as the sodium salt of carboxymethyl cellulose (CMC)[179,180] polyacrylic acid (PAA),[180,181] poly(methyl methacrylate) (PMMA),[181] or poly(ionic liquid)s[182] have been reported as promising new binder systems. Among them, CMC is the most attractive due to its environmental

friendliness and low price. Even though its performance is comparable with that of electrodes based on conventional fluorinated binders,[41,183] the water-solubility of CMC hinders the applications in an aqueous electrolyte system. On the other hand, binder-free electrodes perform well, but they often require expensive CNTs[184,185] and specific processes (fibrous carbon).[186]

Lignin is not only utilized as an active component (as discussed in Chapter 2), but it is also applicable as the binder in low-cost and environmentally friendly LIBs.[125,126,187] For example, Lu *et al.*[126] investigated the possibility of using lignin as the binder material in electrode fabrication. They reported a fairly good rate capacity with good binder functionality after lignin was pretreated to remove small dissoluble fractions. Domínguez-Robles *et al.*[187] presented lignin acting as a substitute for PVDF binder in LIBs with comparable performance to PVDF in terms of cycling stability.

Reducing the amount of binder also reduces the ion blocking on the surface of the electrode film in addition to reducing the amount of inactive material within the electrode. The use of lignin acting as the electroactive materials of the electrode coupled with its binder functionality could be promising to improve the electrochemical performance of the composite electrode. The low molecular weight fractions of lignin may be dissolved partially during charging/discharging cycles causing capacity loss. The high molecular weight fraction of lignin polymer is favorable because it shows increased binder property, but may also limit the adsorption of a thin lignin film on the surface of conductive carbon which is a key role for charge transfer improvement.[161]

The most reactive groups in the lignin structure, phenolic groups and noncyclic ether groups, are subjected to condensation reaction under acidic and alkaline conditions. Since another important dominant functional group in lignin is the phenolic hydroxyl groups, this group has also been used for crosslinking with various reagents[84] such as diacids,[188] isocyanate,[189] and epichlorohydrin.[190] The use of laccase enzyme[191,192] and ultrasonication[193] has also been proposed. Furthermore, polymerization of lignin is also achieved by the crosslinking of electron-rich sites on the aromatic rings of lignin. Methylolation or hydroxymethylation is a conventional chemical modification method of lignin with crosslinking agents such as formaldehyde in alkaline solution. During the methylolation, hydroxylmethyl groups are introduced to the reactive positions of lignin, mainly in *ortho* positions of phenolic groups. The hydroxymethylated lignin can be further

crosslinked *via* the formation of methylene bridges (condensation reaction) in an alkaline medium.[194] Concerning safety and health issues, the substitution of formaldehyde with glyoxal, a nontoxic dialdehyde obtained from several natural sources has been reported.[195-198]

The aim of this chapter is the fabrication of a halogenated-binder-free, environmentally friendly, and sustainable composite electrode based on high surface area carbon containing crosslinked Kraft lignin which is used for both the functions of electroactive compound and binder. The composite electrodes were fabricated by a facile two-step process; adsorption of low molecular weight lignin on the large surface of carbon and then crosslinking it with glyoxal by application of heat. The influence of temperature and the amount of glyoxal was studied, and the crosslinked lignin was investigated by FTIR, SEC, ^{31}P and ^{1}H NMR, and TGA techniques. The electrochemical performance of binder-free lignin composite electrode was evaluated in terms of faradaic and non-faradaic charge storage contribution.

3.2 Characterization

The characterization of modified lignin obtained from heat treatment under air atmosphere was first performed by solubility and molecular weight testing (Figure 3-1). The untreated lignin is easily soluble in high polarity solvents such as dimethylsulfoxide (DMSO), *N*-methyl-2-pyrrolidone (NMP), and dimethyl formamide (DMF) as well as tetrahydrofuran (THF), while it is partially soluble in acetronitrile (ACN), ethanol (EtOH), and chloroform ($CHCl_3$) (Figure 3-1 (a)). The solubility slightly decreases in ACN, EtOH, and THF solvents after heat treatment at 60 ºC, 80 ºC, and 100 ºC for 18 h as seen in Figure 3-1 (b-d), respectively. This may imply some minor condensation or crosslinking occurring during the heat treatment of lignin.[195]

Figure 3-1 (e) presents the molecular weight of the heated lignin determined by size-exclusion chromatography (SEC). Compared to the untreated lignin, both the M_w and M_n of 60 ºC and 80 ºC heat-treated products slightly increases, particularly at 80 ºC, while further increasing the temperature to 100 ºC results in a significant drop of the molecular weight. This may indicate that crosslinking is induced at moderate temperature and some decomposition starts at elevated temperature.

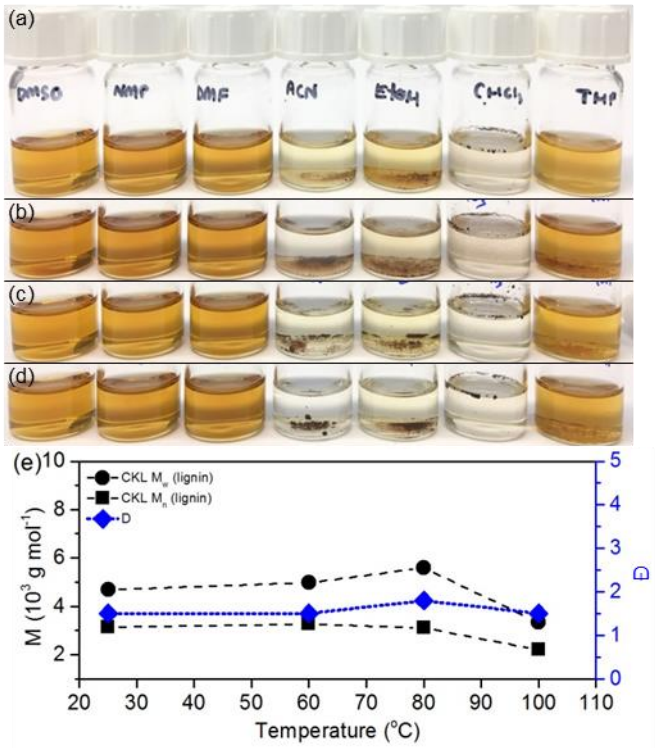

Figure 3-1 Photographs of solutions (1 mg mL^{-1}) of the original lignin (a) and the treated lignin at different temperatures of 60 ºC (b), 80 ºC (c), 100 ºC (d) for 18 h (from left to right: solution in DMSO, NMP, DMF, ACN, EtOH, $CHCl_3$, and THF). Molecular weight as determined by SEC in NMP of these modified lignins (e). Reprinted and adapted by permission.[199] Copyright 2017, Royal Society of Chemistry.

To further understand the thermal behavior of the original lignin and its derivatives, TGA was measured. The thermal behavior of lignin depends on its sources and the involved extraction processes. The unmodified lignin thermally decomposes over a broad temperature range due to its complex structure with various oxygen functional groups on aromatic ring and side chains. The results from TGA measurement and DTG (derivative thermogravimetry) of the unmodified lignin are exhibited in Figure 3-2 (a-b) with three events taking place during measurement. The first DTG peak corresponds to the moisture evaporation around 50-100 °C with 6% weight loss. The second DTG peak was recorded in the range of 100 °C to 300 °C. This may be attributed to the lower molecular weight fraction of lignin, which is less thermally stable or the elimination of volatile species (e.g., formic acid, formaldehyde, and carbon dioxide) from the degradation of the phenylpropane side chains during the solid-content test.[200,201] The third DTG peak (in the range of 300-450 °C), the maximum mass loss (44%), is mainly attributed to the decomposition of the remaining lignin polymers.

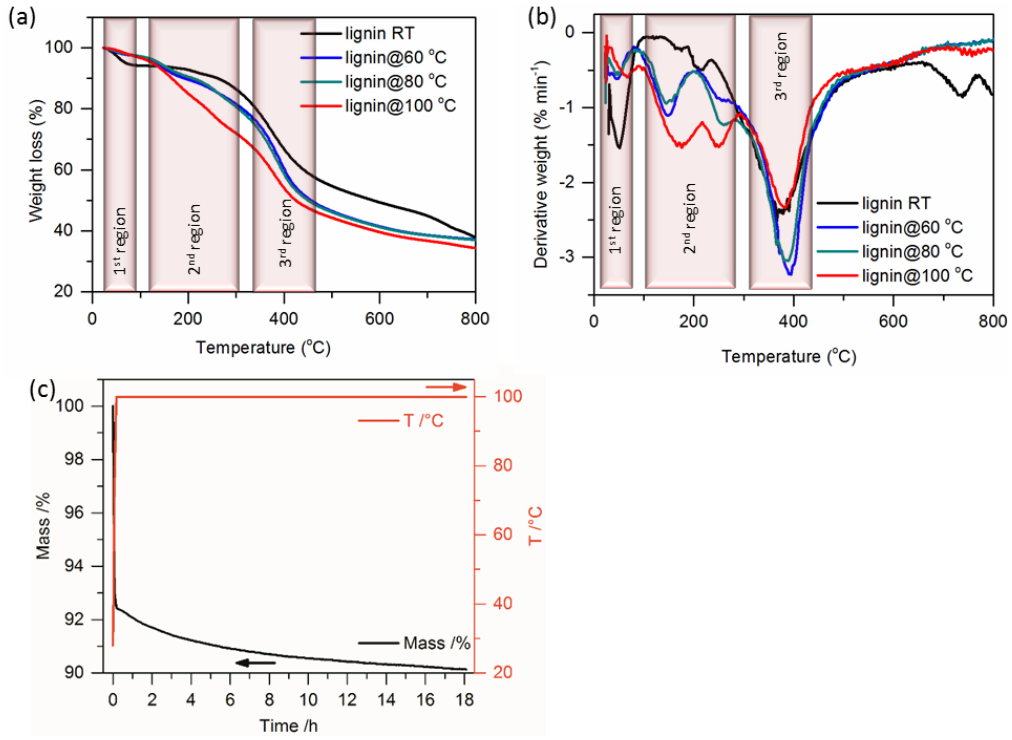

Figure 3-2 TGA results of lignin after heat treatment at various temperatures for 18 h (a), the corresponding DTG curves (b), and TGA result of lignin while keeping the temperature at 100 ºC for 18 h under synthetic air (c). Reprinted and adapted by permission.[199] Copyright 2017, Royal Society of Chemistry.

After heat treatment of lignin, there is a change of thermal behavior. The amount of mass lost in the first step is reduced indicating a lower water content in all heat-treated lignin samples. The second DTG peak region shows a significant increase of mass loss. This might be due to some inner changes in the lignin structure after heat treatment causing some less thermal stable products, particularly more pronounced at 100 °C. In addition, the main decomposition peak in the third DTG region was observed to have lower mass loss due to greater decomposition occurring in the second region leading to the less amount of material left. Figure 3-2 (c) presents the TGA result of lignin measured by keeping the temperature at 100 ºC for 18 h. The sample continuously loses weight during the whole 18 h measurement indicating some modifications in the structure leding to weight loss.

FTIR spectroscopy was also employed to characterize the change of functional groups in lignin after heat treatment compared to unmodified lignin (Figure 3-3 (a-b)). The characteristic peaks of lignin are presented by a broad band around 3430 cm^{-1}, which corresponds to the hydroxyl groups in the phenolic and aliphatic structures, followed by the bands of C-H stretching in the aromatic methoxy groups and the methyl and methylene groups of the side chains (around 2942 cm^{-1} and 2835 cm^{-1}). The weaker carbonyl group

band is located at 1704 cm^{-1}. The aromatic skeleton C-C stretching can be seen at 1603 cm^{-1}, 1514 cm^{-1}, and 1430 cm^{-1}. The peaks of the phenolic hydroxyl groups appears at 1370 cm^{-1} and 1270 cm^{-1}. The presence of aliphatic OH and ether groups is visible at 1060 cm^{-1}. The last characteristic signals of lignin consist of aromatic C-H stretching at 1140 cm^{-1} and aromatic C-H bending at 858 cm^{-1} and 805 cm^{-1}.[196,202-204]

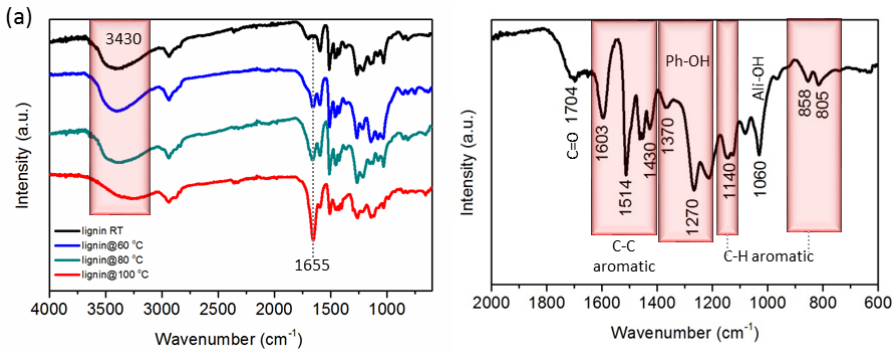

Figure 3-3 FTIR spectra of lignin after heat treatment at various temperatures for 18 h (a) and FTIR spectrum with expansion region of the untreated sample (lignin RT) (b). Reprinted and adapted by permission.[199] Copyright 2017, Royal Society of Chemistry.

After heat treatment, the modified lignin samples present decreased absorption of the broad OH vibration at around 3430 cm^{-1} with an increase in the temperature of heat treatment. It is assumed that this is a consequence of the condensation, which causes the loss of some hydroxyl groups in lignin.[195] The presence of the peak at 1655 cm^{-1} along with the increase in temperature indicates the formation of quinone methide by air oxidation reaction during heat treatment under air atmosphere.[116,205]

When treating lignin with glyoxal, crosslinking can be performed between lignin and a dialdehyde crosslinking agent at elevated temperature.[195,196,206] During the reaction of lignin with glyoxal, a number of different glyoxalated lignin structures may be formed. Some reports proposed a reaction pathway of the reaction of lignin with glyoxal as summarized in Scheme 3-1. First is the glyoxalation or substitution reaction of glyoxal to phenolic ring (i) to form a benzyl alcohol type group at the *ortho* site of phenolic groups (i-a).[207] At the same time, the heating of lignin in air during glyoxalation may cause the generation of quinone methide and incorporation of glyoxal (i-c).[116,208] The subsequent condensation reaction with another phenolic rings is induced by temperature or pH.[209,210] The crosslinked products might be in the form of ii-a,[141,207] ii-b, ii-c,[198] ii-d,[198] to only name a few possibilities.

Here the lignin was treated with glyoxal (0.82 mol eq. of phenolic hydroxyl (Ph-OH) in lignin, 2.33 mmol g^{-1}) at elevated temperature and the solubility of the product was tested. It was found that treatments at 60 ºC and 80 ºC provide glyoxalated lignin products with a significantly decreased solubility, particularly in DMSO, NMP, DMF, and THF which are good solvents for untreated lignin and the lignin modified by heat treatment. However, at a temperature of 100 ºC, the lignin product which was treated in the presence of glyoxal exhibits a solubility resembling the untreated lignin with a slightly lower solubility in THF (Figure 3-4 (a-d)).

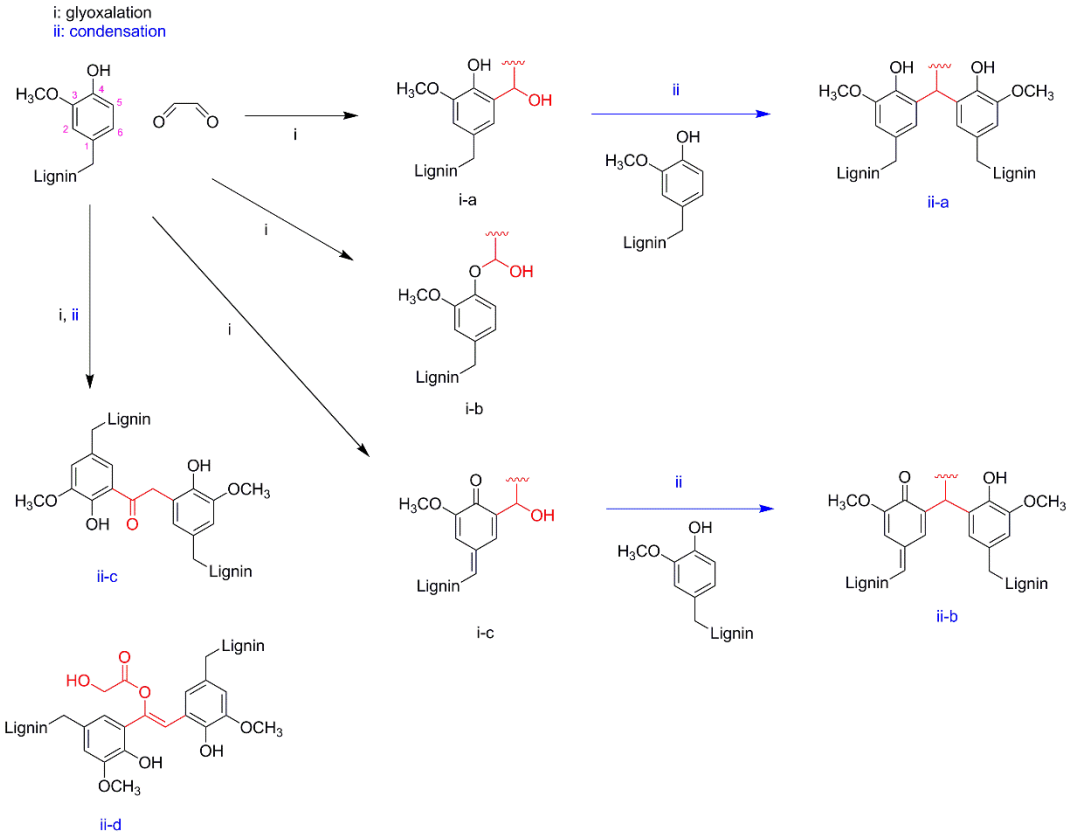

Scheme 3-1 Possible products from the glyoxalation and condensation reaction of lignin. Glyoxalated lignin products with incorporation of a benzyl alcohol type group and crosslinked lignin products.

Because of the solubility limitation of the glyoxalated lignin samples in any solvent, only the molecular weight of the soluble fraction in NMP was evaluated by SEC. So, the observed molecular weight may be lower than the actual value. The observed molecular weight of the glyoxal treated lignin (Figure 3-4 (e)) significantly increases with the increasing temperature of the heat treatment reaching a peak at 80 ºC before slightly dropping at 100 ºC. This may be attributed to thermal decomposition induced by heat treatment at 100 ºC over a long period (18 h), cf. Figure 3.2 (c). At 60 ºC and 80 ºC,

however, the glyoxalated lignin products demonstrate a higher M_w and M_n than those obtained from heat treatment in the absence of glyoxal. Thus, the observation of partial solubility of lignin product after glyoxalation agrees with the assumption of successful crosslinking at 60 °C or 80 °C.

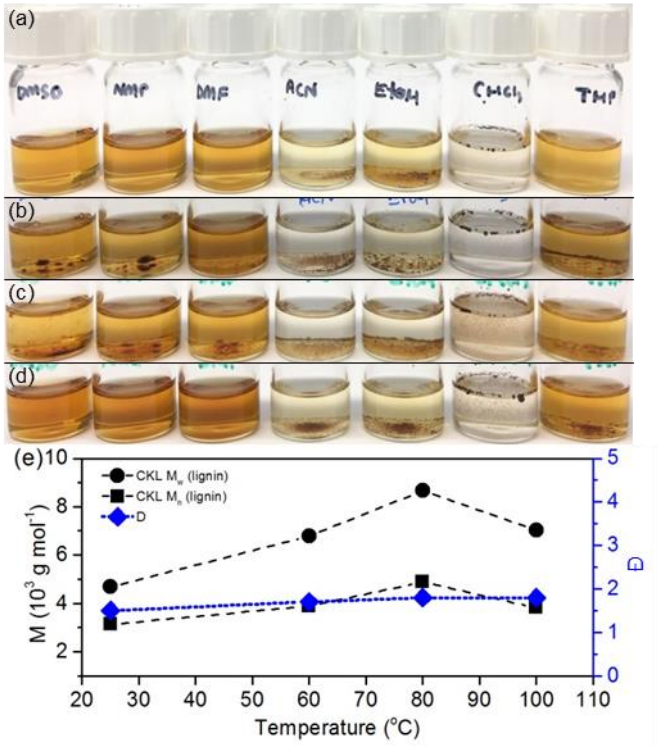

Figure 3-4 Photographs of solutions (1 mg mL^{-1}) of the original lignin (a) and the glyoxal-treated lignin at different temperatures of 60 °C (b), 80 °C (c), 100 °C (d) for 18 h (from left to right: solution in DMSO, NMP, DMF, ACN, EtOH, $CHCl_3$, and THF). Molecular weight as determined by SEC in NMP of these modified lignins (e). Reprinted and adapted by permission.[199] Copyright 2017, Royal Society of Chemistry.

A heterogeneous polymer chain length is probably the result of various possible reactions induced by glyoxal addition including depolymerization, cleavage of lignin units, condensation with glyoxal, and polymerization.[207] The glyoxal treated lignin samples reveal a slightly higher dispersity (Đ) compared to the heat treated lignin samples. This observation might be caused in parts by the limited solubility in any solvent of the samples so only the soluble fraction was evaluated by SEC, and especially by the different possible reactions as described above.

Figure 3-5 (a-b) shows the TGA and DTG curves of unmodified and glyoxal treated lignin prepared at different temperatures. The initial weight loss (temperature range < 100 C°) is attributed to moisture evaporation and less intense for glyoxal treated lignin samples

compared to untreated lignin. The second stage occurs in the temperature range of 100 °C to 300 °C with the influence of the postcuring of glyoxalated lignin as generally occurrs in phenol-formaldehyde resin behavior.[194,211,212] Thus, the mass loss in this region is a result of the loss of water, formaldehyde, or glyoxal molecules. The condensation reaction (ii) as shown in Scheme 3-1 of glyoxalated lignin to form crosslinked lignin contributes to a process of losing water molecules, while the breaking of benzyl alcohol type groups in glyoxalated lignin leads to the release of formaldehyde or glyoxal molecules.[211,212]

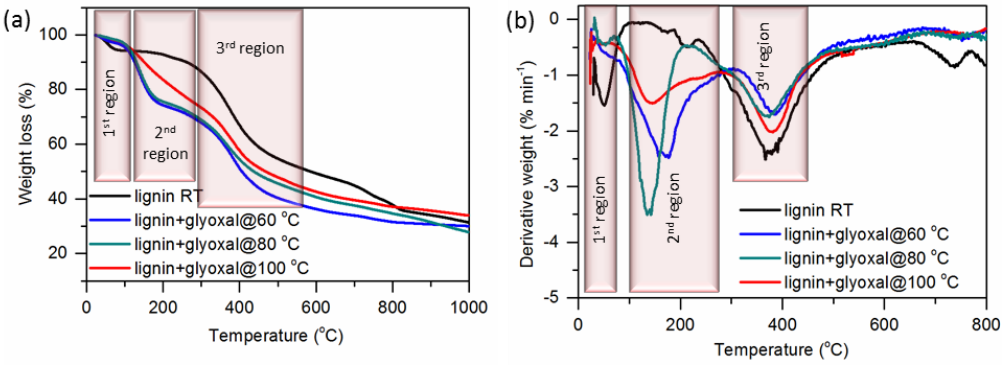

Figure 3-5 TGA result of crosslinked lignin in the presence of glyoxal after heat treatment at various temperatures for 18 h (a) and the corresponding DTG curves (b).

Mass loss in this temperature range is more intense for samples which were treated at 60 °C or 80 °C. However, treatment at 100 °C presents a different behavior; weight loss in this region is lower. This may be due to the volatility of glyoxal at elevated temperature leading to less glyoxalated lignin product after this heating protocol. The third thermal degradation step is the main weight loss of lignin. In this step, the amount of weight loss of the glyoxalated lignin samples is lower since greater decomposition occurs in the earlier stage. The influence of glyoxal on thermal behavior in this range might be more obvious when comparing between heat treated and glyoxalated lignin samples at the same annealing temperature as will be discussed later.

The FTIR spectra of all glyoxal treated lignins are presented in Figure 3-6 in comparison to unmodified lignin. It was found that an increase in the absorbance intensity of the OH band (3430 cm^{-1}) and C-H stretching band in aromatic and aliphatic side chains (2942 cm^{-1}) correlates to an increase in the treatment temperature. This indicates the incorporation of CH_2OH groups into the lignin polymer through a glyoxalation reaction.[196] This result supports the TGA results shown above. The band at around 1255 cm^{-1} to 1081 cm^{-1} mainly arises from C-O-C stretching, and C-O vibration in primary alcohols. The two peaks at

1655 $cm^{-1}$and 1141 cm^{-1} are attributed to carbonyl groups (conjugate C=O) and ether linkage (C-O-C) which increase similarly to the result of heated-treat lignin samples. The slightly increased band at 1081 cm^{-1} is ascribed to the out-of-plane stretching of phenols or C-O deformation of secondary alcohol and aliphatic ethers.[155]

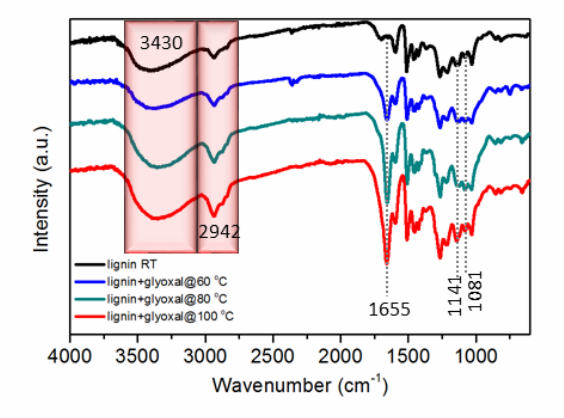

Figure 3-6 FTIR spectra of unmodified lignin (RT) and crosslinked lignin with glyoxal samples at various treatment temperatures for 18 h. Adapted by permission.[199] Copyright 2017, Royal Society of Chemistry.

In order to prove the existence of incorporated glyoxal in lignin after annealing in a vacuum oven, gravimetric experiments were performed. Figure 3-7 displays the photographs of lignin carbon composite without and with glyoxal coated on Al foil substrate after annealing at elevated temperature. It is clear that the composite film with glyoxal is smoother and more stable after annealing at 60 °C for 18 h in vacuum; the one without glyoxal on the contrary is brittle. This is good indication proving the improvement of the stability of the composite film by glyoxal. The summarized results of the gravimetric determination are shown in Table 3-1.

After 18 h in a vacuum oven at 60 °C, some NMP remains in the composite electrode. Even after keeping the sample under vacuum conditions for 2 weeks, there is approximately 1.06 mg (Δm (14 days)-m^c = 32.90-31.84 mg) NMP left in the electrode material made of lignin and carbon samples (31.84 mg). The amount of NMP in the sample containing glyoxal is higher, with 2.48 mg (Δm (14 days)-m^c = 35.46-32.98 mg) remaining. This implies that the existence of glyoxal in the composite film causes the higher amount of mass to be present. Thus, this also indicates that the glyoxal did not evaporate or unbound during thermal annealing under vacuum but that it was incorporated into the lignin. Otherwise, the film would be lighter than the calculated initial dry mass (32.98 mg) due to the evaporation of glyoxal (boiling point *ca.* 50 °C).

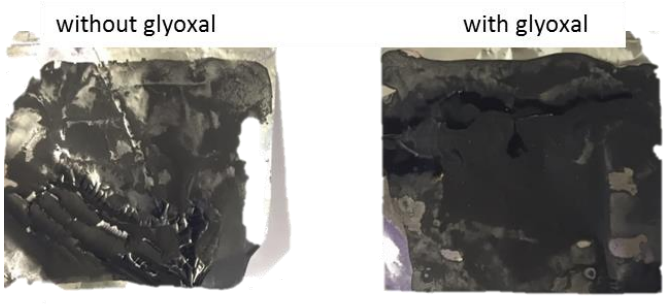

Figure 3-7 Photographs of lignin carbon composite without and with glyoxal coated on Al foil substrate after annealing at 60 °C for 18 h. Reprinted by permission.[199] Copyright 2017, Royal Society of Chemistry.

Table 3-1 Electrode mass after annealing at 60 °C for 18 h and subsequently drying in vacuum at room temperature in order to remove traces of remaining solvent. Reprinted and adapted with permission[199] from The Royal Society of Chemistry.

	m^a (substrate) /g	m^b (coated substrate) /g	m^c /mg	m^b (coated substrate) /g	Δm /mg	m^b (coated substrate) /g	Δm /mg	m^b (coated substrate) /g	Δm /mg
Time	-	before annealing		after 18 h		after 7 days		after 14 days	
lignin + carbon (three samples)	0.10136	0.27455	31.34	0.13910	37.74	0.13360	32.24	0.13345	32.09
	0.10200	0.27950	32.12	0.14150	39.50	0.13606	34.06	0.13585	33.85
	0.10166	0.27890	32.07	0.14050	38.84	0.13460	32.94	0.13441	32.75
average			31.84		38.69		33.08		32.90
lignin + carbon + glyoxal (three samples)	0.10225	0.28300	33.52	0.14338	41.13	0.13855	36.30	0.13815	35.90
	0.10236	0.28198	33.31	0.14348	41.12	0.13921	36.85	0.13879	36.43
	0.10123	0.27436	32.11	0.14188	40.65	0.13535	34.12	0.13529	34.06
average			32.98		40.97		35.76		35.46

m^a: mass of Aluminium foil substrate
m^b: mass of composite coated substrate
m^c: initial dry mass of composite calculated from solid content at 120 mg in NMP 500 µL which is used for slurry preparation: lignin+carbon (solid content: 114.1 mg in total slurry mass: 630.6 mg), lignin+carbon+glyoxal (solid content: 119.7 mg in total slurry mass: 645.5 mg)

To further understand the change of lignin behavior after different treatments, Figure 3-8 summarizes the results of thermal and FTIR analysis of the lignin samples with heat treatment at 60 °C (with and without glyoxal) compared to untreated lignin. TGA and DTG curves are presented in Figure 3-8 (a-b). In the presence of glyoxal, the weight loss is more pronounced in the second region. This indicates the further curing reaction of glyoxalated lignins happening during measurement as mentioned before.

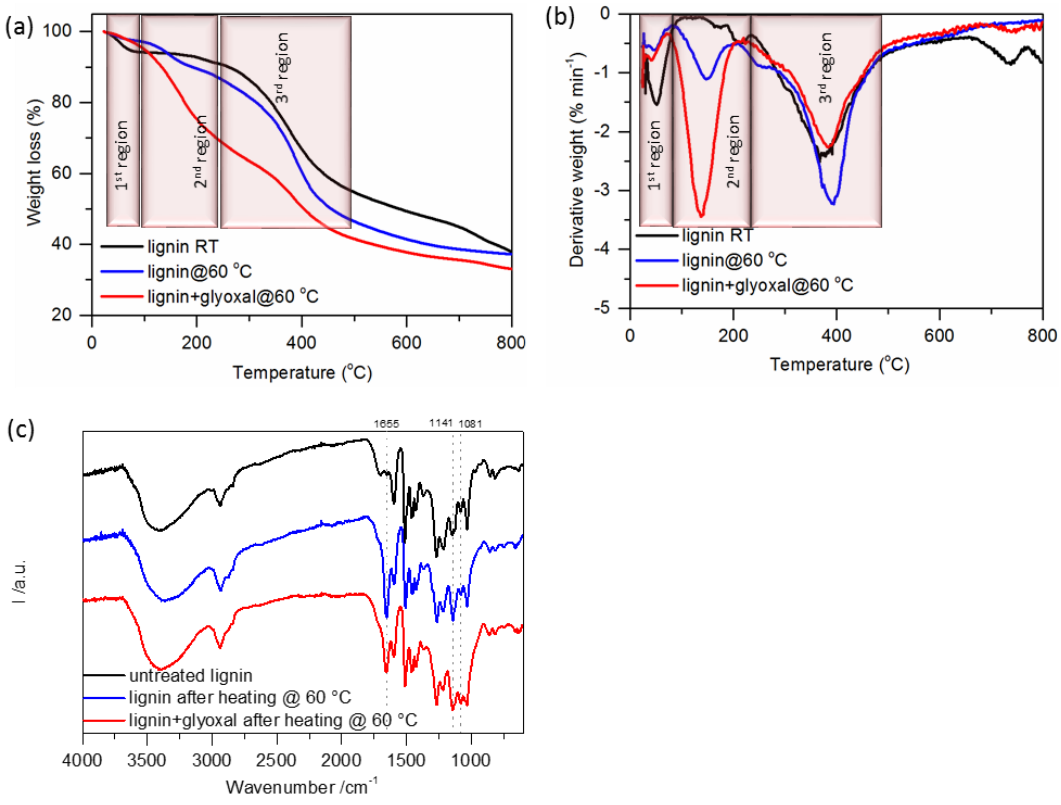

Figure 3-8 TGA (a), DTG (b), and FITR (c) spectra of different lignin samples (untreated, heat treated at 60 ºC in the absence and presence of glyoxal). Reprinted and adapted by permission.[199] Copyright 2017, Royal Society of Chemistry.

Figure 3-8 (c) displays a comparison of FTIR spectra between different lignin samples: untreated, heat treated at 60 ºC (in the absence and presence of glyoxal). It shows that heat treatment leads to a strong peak at around 1655 cm^{-1} and an increase in the intensity of the peak at around 1141 cm^{-1} with a slight decrease of intensity of OH broad band at around 3430 cm^{-1} as described above. This suggests that partial oxidation of phenolic groups induced by heat treatment in the air atmosphere is independent of glyoxal. In case of glyoxal present in the reaction, there is partial substitution of the benzyl alcohol type groups into free C5 positions of the lignin aromatic groups indicated by an increase of the OH band and CH stretching at 2942 cm^{-1} of the aliphatic side chains. This enhances the reactivity of the lignin and links the lignin molecules together.[195,207,213] Furthermore, the intensity of the peak at around 1080 cm^{-1} significantly increases, suggesting secondary alcohols and aliphatic ethers. Therefore, the information obtained from FTIR and TGA are in good agreement with the assumption of successful glyoxalation under the tested conditions.

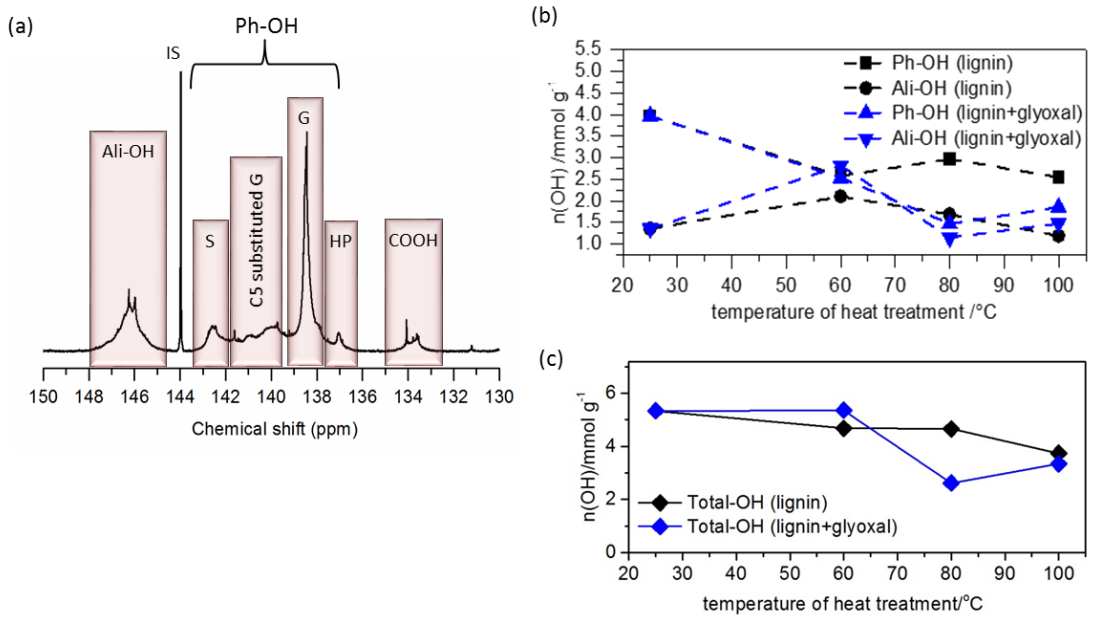

Figure 3-9 ^{31}P NMR spectrum of unmodified lignin after phosphitylation with peak analysis (a), amount of different hydroxyl groups (b), and total amount of hydroxyl groups (c) depending on the temperature of heat treatment both with and without glyoxal; calculated from the integral area of ^{31}P NMR spectra compared with an internal standard (IS) as shown in Appendix C (supplementary information). Reprinted and adapted by permission.[199] Copyright 2017, Royal Society of Chemistry.

NMR spectroscopy is a useful technique to follow the evolution of functional groups. Two types of NMR technique were employed: ^{31}P and ^{1}H NMR. The phosphitylation method (see Appendix) was used to detect variations of the hydroxyl functional groups existing in lignin samples, providing valuable chemical structure evidence. The ^{31}P NMR spectrum of an unmodified lignin sample is presented in Figure 3-9 (a). The different OH-bearing groups are quantified in the presence of an internal standard following previous reports.[152,214,215] The results of all modified lignin samples are summarized in Figure 3-9 (b-c), and ^{31}P NMR spectra are shown in Appendix C (supplementary information). The amount of Ali-OH appears to slightly increase after heat treatment at 60 ºC but drops after treatment at higher temperatures in the absence of glyoxal compared to unmodified lignin. While the amount of Ph-OH first decreases after heat treatment at 60 ºC, it remains at almost constant value after heat treatment at higher temperature. The increase in the amount of the Ali-OH of the lignin sample which was heat treated at 60 ºC might be because of large potential errors obtained from NMR analysis and peak fitting. In general, the NMR technique is good enough for qualitative structural study; however, it is not good enough for precise quantitative work such as in the case of overlapping bands or an unflattened baseline. For this reason, it can be reasonably concluded that a reduced amount

of hydroxyl groups with increase in heat treatment temperature may be attributed to thermally induced condensation reactions which is consistent with FTIR and TGA results. The samples present different properties after heat treatment with glyoxal. The heat treatment was conducted in NMP solvent possessing an alkaline solvent character,[216] which should limit the formation of acetal with glyoxal. An increase of Ali-OH at 60 ºC treatment (more pronounced than in the samples without glyoxal) may be a result of the incorporation of glyoxal into lignin; however, a decrease of the amount of Ali-OH when annealing at a higher temperature (at 80 ºC) is explained by a condensation reaction taking place to form crosslinked lignin. The amount of Ph-OH is greatly reduced at high temperature which may indicate that crosslinking occurs through Ph-OH. In addition, crosslinking may occur through the free *ortho*-position in the phenolic ring.[116] The total number of hydroxyl groups (Total-OH) in heat treated lignin slightly decreases with increasing temperature while glyoxalated lignin shows a significant decrease of Total-OH due to thermally induced condensation accompanied by the crosslinking reaction. The amount of Total-OH appears to slightly increase when further heating at 100 °C, regardless the presence of glyoxal. This might be because some decomposition occurred or an error from NMR measurement as mentioned above.

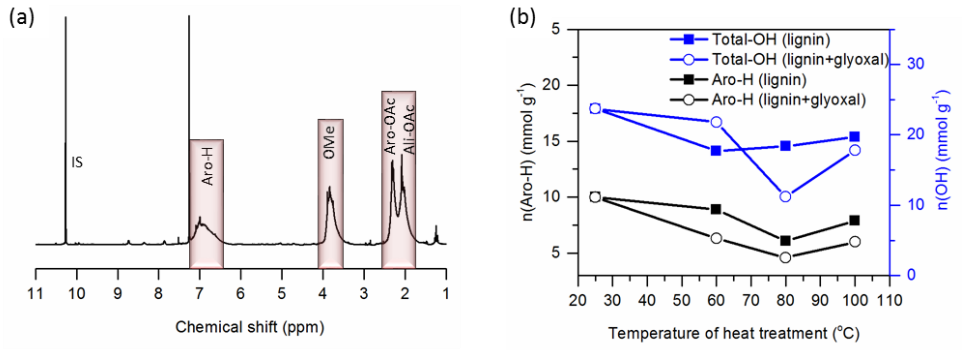

Figure 3-10 ^{1}H NMR spectrum of unmodified lignin after acetylation with peak analysis (a) and amount of aromatic protons and total hydroxyl groups depending on the temperature of heat treatment both with and without glyoxal (b), calculated from the integral area of ^{1}H NMR spectrum (as shown in Appendix C (supplementary information)) compared with an internal standard (IS).

Furthermore, ^{1}H NMR yields useful information to support the ^{31}P analysis. Figure 3-10 (a) demonstrates the ^{1}H NMR spectrum of unmodified lignin sample with peak analysis. The number of functional groups is estimated from the intensity of the proton signals corresponding to each functional group in reference to the internal standard (2,3,4,5,6-

pentafluorobenzaldehyde).[217] The quantitative results of all modified lignin samples are exhibited in Figure 3-10 (b).

The peaks of aliphatic-acetate's (Ali-OAc) and aromatic-acetate's (Aro-OAc) protons, corresponding to Ali-OH and Ph-OH, are not separated well enough for quantitative analysis, and so are determined in terms of Total-OH. The decreasing number of Total-OH in the glyoxalated lignin samples correlates to increasing the temperature of heat treatment in good agreement with ^{31}P NMR analysis. It remains almost unchanged when heating to 60 °C, then substantially decreases as the temperature further increases to 80 °C. This might be attributed to the competitive reactions between glyoxalation and condensation reactions leading to nearly constant value as described above. Samples without glyoxal present a decrease of Total-OH, then stay approximately constant with increasing temperature. In addition, the ^{1}H NMR of acetylated lignin samples could provide additional information concerning the amount of aromatic protons (Aro-H). Unfortunately, the results might be influenced by an imprecise estimation stemming from the integral area of overlapping peaks and unflattened baseline as a result of the uncredible results of the decreased amount of Aro-H independent of whether the sample contained glyoxal or not. Finally, only the amount of Total-OH estimated from acetylated lignin samples is in good agreement with ^{31}P NMR analysis.

Further experiment was attempted to improve the crosslinking of lignin with glyoxal by keeping the amount of Ph-OH as high as possible. From the crosslinking results, at treatment at 80 ºC the glyoxalated lignin revealed the highest molecular weight. The highest amount of Ph-OH was observed from the glyoxalated lignin which was annealed at 60 ºC. Therefore, the heat treatment condition was slightly modified by adding a further short annealing step, 80 ºC for 2 h, after annealing at 60 ºC for 18 h. The solubility behavior does not significantly change as shown in Figure 3-11 (a) when comparing with glyoxalated lignin samples annealed at 60 ºC and 80 ºC, (Figure 3-4 (b-c)). To further prove the assumption of the successful crosslinking, lignin was treated with two or four times as much glyoxal with the modified annealing treatment (annealing at 60 ºC for 18 h then short annealing at 80 ºC for 2 h). As regards solubility, the obtained products were almost completely insoluble in any solvent (Figure 3-11 (b-c)). However, SEC analysis determined only the soluble fraction which might yield significant difference between observed molecular weight and real molecular weight. Still, even the observed molecular

weight and dispersity greatly increase with an increasing of amount of glyoxal (Figure 3-11 (d)).

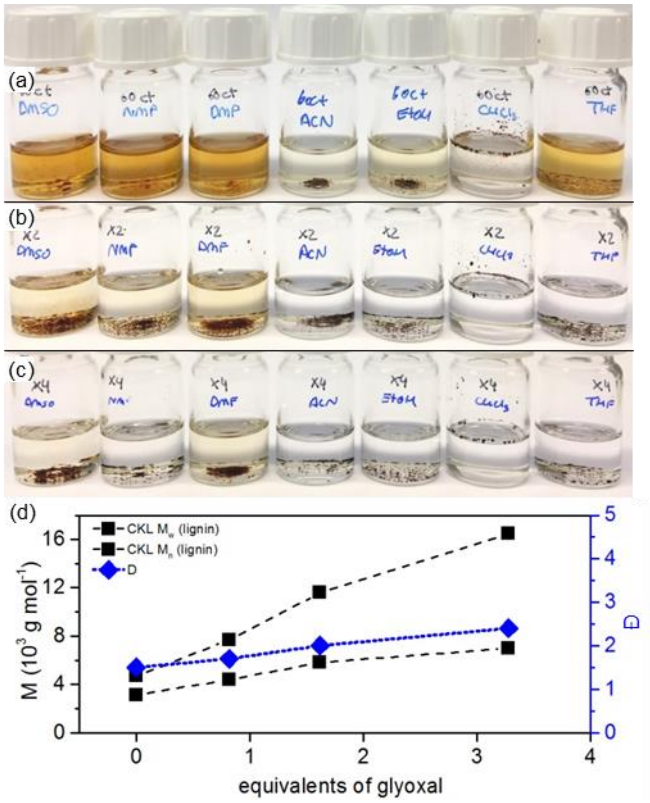

Figure 3-11 Photographs of solutions (1 mg mL^{-1}) of lignin which was treated with glyoxal (a) at elevated temperature of 60 °C for 18 h and subsequently at 80 °C for 2 h (from left to right: solution in DMSO, NMP, DMF, ACN, ethanol, chloroform, and THF). The amount of glyoxal was twice (b) or four times (c) as high as in (a). Molecular weight as determined by SEC in NMP of these modified lignins (d). Reprinted and adapted by permission.[199] Copyright 2017, Royal Society of Chemistry.

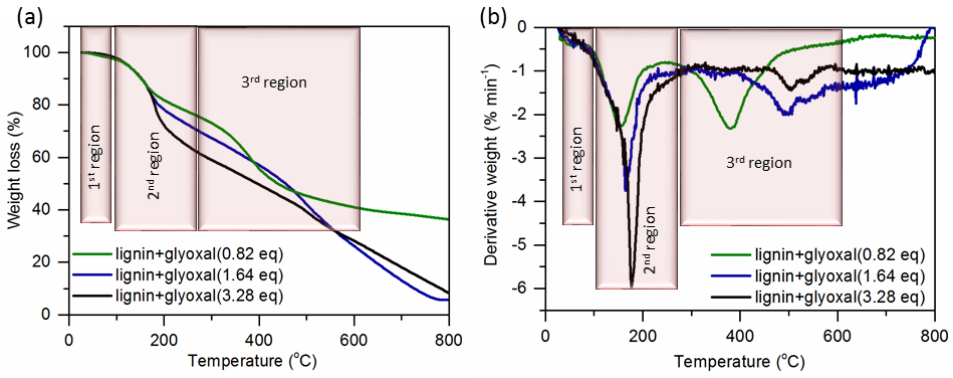

Figure 3-12 TGA (a) and DTG (b) curves of the heat-treated lignin samples at 60 °C for 18 h and subsequently at 80 °C for 2 h with various amounts of glyoxal.

The TGA and DTG curves are shown in Figure 3-12 (a-b). Increasing the amount of glyoxal contributes to the increasing amount of mass loss in the second region and a shift in the decomposition temperature of lignin in the third region to higher temperature (shift to above 400 °C) with decreased mass loss. As described earlier, mass loss in the second region of mass loss is a result of the condensation and bond breaking of glyoxalated lignin. There is even further mass loss when increasing the amount of glyoxal. These results give strong support to the explanation of successful glyoxalation. The significant increase in decomposition temperature is due to the increase of crosslinking in the samples during measurement.[195,198]

3.3 Charge storage properties of a binder-free lignin composite electrode

The electrodes were fabricated from glyoxalated lignin-based materials and high surface area carbon. The charge storage was investigated by cyclic voltammetry including capacity contributions from faradaic and non-faradaic processes as described in Chapter 2. Two different means of electrode preparation were employed in order to investigate the influence of crosslinked lignin. First, electrodes were prepared from lignin that was heat treated in the presence of glyoxal at various temperatures prior to blending with high surface area carbon (equal amounts of both). In an alternative approach, a slurry of lignin, glyoxal and high surface area carbon (same weight ratio as in the first approach) was prepared and casted onto a graphite sheet and annealed at different temperatures.

The first approach is demonstrated in Figure 3-13 (a). The result of the charge storage contribution is revealed in Figure 3-13 (c) and the corresponding CV curves in Figure 3-13 (b). The samples crosslinked at 60 ºC and 80 ºC show the same charge storage behavior, but the capacity is higher than the samples in which lignin was crosslinked at 100 ºC or without heat treatment (RT). Faradaic charge storage change is found only if the lignin samples are crosslinked. In spite of the different amounts of Ph-OH groups (estimated from ^{31}P NMR), the crosslinked lignin samples annealing at 60 ºC and 80 ºC reveal approximately the same faradaic charge storage. The explanation is that only redox reactions at the electrode-electrolyte interface are attributed to charge storage. During crosslinking, a change in the structure of lignin may reduce the contact between electroactive moieties and carbon. The pathway of electron transfer from active sites of lignin to the current collector might be interrupted and as a consequence, faradaic charge

storage is less efficient. Therefore crosslinked lignin with a higher molecular weight may not be beneficial for charge storage in this system.

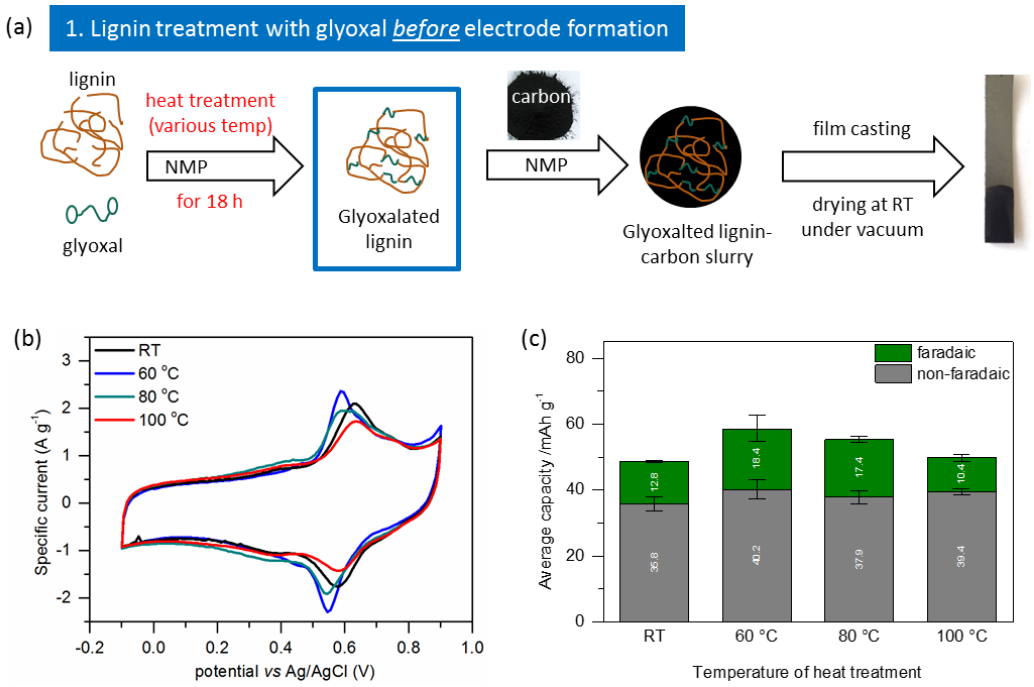

Figure 3-13 Electrode fabrication with glyoxalated lignins which were synthesized at different temperatures *before* electrode preparation (a), CV curves recorded at 5 mV s^{1} in 1 M $HClO_4$ (b) and capacity of the corresponding samples (c). Reprinted and adapted by permission.[199] Copyright 2017, Royal Society of Chemistry.

Nevertheless, the composite electrodes which were prepared using the same approach but different annealing conditions, namely room temperature and 100 ºC, present even worse faradaic charge storage capacity. Even though the amount of Ph-OH is higher in the lignin based electrode without heat treatment (RT), the faradaic charge storage capacity is lower than those electrodes annealed at 60 °C and 80 °C. One possible explanation might be the lignin not reacting with glyoxal under room temperature treatment. As a consequence, the remaining chemicals adsorbed on the electrode film such as unreacted gloxal and NMP cause a less efficient faradaic contribution. Similarly, there seems to be no crosslinked structure at 100 ºC of treatment, but the reason for yielding a low faradaic capacity might differ. The heat treatment at high temperature over a long period may probably lead to some changes in lignin structure (as discussed before) causing a lower faradaic charge storage capability.

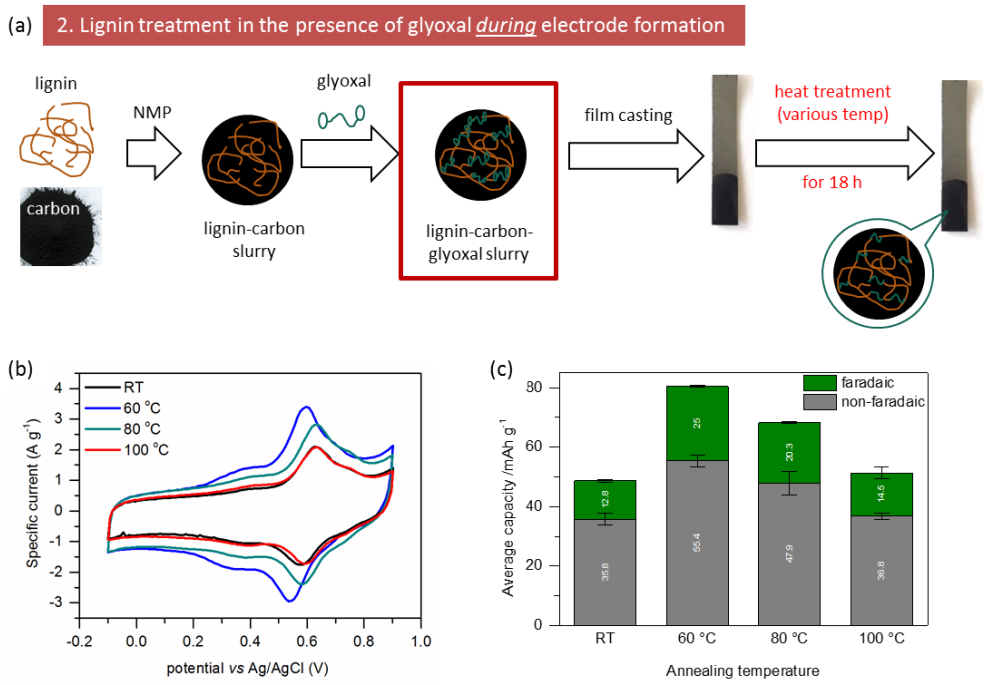

Figure 3-14 Electrode fabrication from crosslinking lignin in the presence of glyoxal (annealing at different temperatures) *during* electrode preparation (a), CV curves recorded at 5 mV s^1 in 1 M $HClO_4$ (b), and capacity of the corresponding samples (c). Reprinted and adapted by permission.[199] Copyright 2017, Royal Society of Chemistry.

In order to prove the efficiency of crosslinking lignin for capacity improvement, another fabrication approach was investigated. The process sequence is displayed in Figure 3-14 (a). The unmodified lignin was first mixed with high surface area carbon, and glyoxal was subsequently added into the mixture. Crosslinking was conducted *via* heat treatment at different temperatures (in a vacuum oven). The amount of glyoxal used was the same as in the approach utilizing crosslinking in solution, and the ratio of crosslinked lignin and carbon was also to the same as in the first approach. Figure 3-14 (c) exhibits the total charge storage capacity of all samples. Both electrodes which were crosslinked at 60 ºC and 80 ºC show a higher charge storage capacity compared to those using previously crosslinked lignin. Figure 3-14 (b) presents the CV curves of all samples. A comparison of the CV scans of lignin composite electrode with different electrode fabrication approaches annealing at 60 °C with a carbon electrode (without lignin) is presented in Figure 3-15. It obviously reveals an additional redox peak to a capacitive background of the carbon electrode (black line). Particularly, a more pronounced redox couple peak appears in the lignin composite electrode prepared by performing crosslinking with glyoxal during electrode formation (red line).

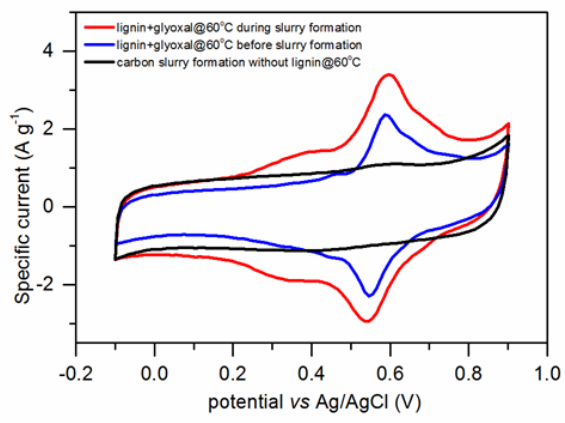

Figure 3-15 Cyclic voltammetry scans of glyoxalated lignin based electrodes (with high surface area carbon) (red, blue) and comparable samples of high surface area active carbon (black). Before measurements, the carbon sample was heat-treated at 60 °C for 18 h (black). Red: lignin was glyoxalated in solution at 60 °C for 18 h before electrode slurry formation; blue: a slurry of lignin, glyoxal, and high surface area active carbon was annealed at 60 °C for 18 h. Reprinted by permission.[199] Copyright 2017, Royal Society of Chemistry.

As discussed in Chapter 2, a good electrical and ionic conductivity are important factors for the improvement of the faradaic charge storage capacity of a lignin composite electrode. The formation of a thin lignin film covering the carbon surface provides a good contact. The use of crosslinked lignin (before slurry formation) is the reason for a worse charge transfer process due to a reduced contact area between the high molecular weight of crosslinked lignin and carbon. Consequently, a lower faradaic charge storage is obtained. In contrast, the lignin composite electrode which was prepared by crosslinking lignin during electrode fabrication benefits from the adsorption of low molecular weight lignin on the carbon surface before crosslinking, leading to the facilitation of electron transportation as shown in Scheme 3-2.

After crosslinking with glyoxal during the heat treatment, the stability of the film improves as a result of the high molecular weight lignin network covering the carbon particles. As the temperature of heat treatment is increased, capacity gradually drops in faradaic charge storage contribution. This may be the result of a decrease of the amount of Ph-OH groups in the samples which were treated at high temperature. Considering the nonfaradaic charge storage contribution, increasing temperature leads to a slightly lower value which is attributed to the greater inflexibility of the electrode film. At 100 ºC heat treatment condition, some decomposition compounds which occur during heat treatment might reduce the accessibility of the surface by the electrolyte.

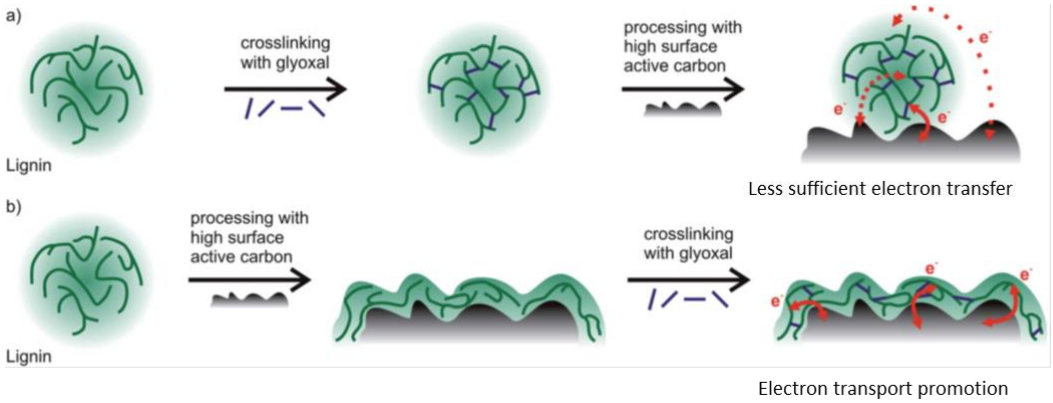

Scheme 3-2 Schematic drawing shows the influence of the order of the processing steps on the capacity of the system. (a) Glyoxalated lignin with high molecular weight is used to form composite with high surface area active carbon. Charge transfer is limited. (b) Electrodes from the components are formed, and afterwards lignin is crosslinked by glyoxal. Charge transfer is facilitated. Reprinted by permission.[199] Copyright 2017, Royal Society of Chemistry.

Even though capacity is lower, crosslinking by glyoxal at 80 ºC results in better stability of sample compared to samples annealed at 60 ºC. To combine both advantages, the electrode formation was slightly modified by adding a further short 2 h annealing step at 80 ºC after 18 h at 60 ºC. The modified crosslinked process (additional annealing at 80 C for 2 h) reveals a slight increase in charge storage capacity as shown in Figure 3-16.

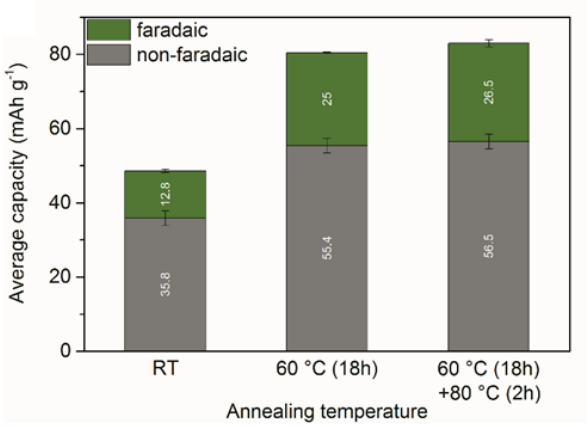

Figure 3-16 Capacity of glyoxalated lignin based electrodes (with high surface area carbon) in dependence of the annealing temperature. Reprinted by permission.[199] Copyright 2017, Royal Society of Chemistry.

Next, the amount of glyoxal is studied with varying amounts (0, 5, and 10 wt%) by following the 2-step electrode fabrication procedure (crosslinking in the presence of glyoxal during the electrode fabrication, annealing at 60 ºC for 18 h and additionally at 80 ºC for 2 h). Another two lignin carbon composite electrodes were fabricated for comparison: one using PVDF as the binder and one without a binder or crosslinker (only

lignin and carbon). Figure 3-17 summarizes the resulting capacity. It was found that the electrode film without the binder or crosslinker is less stable. Even though there is 50 wt% of lignin, the composite film is brittle and it peels off during measurements. This indicates that the addition of a binder or crosslinker is necessary for the stability of the electrode.

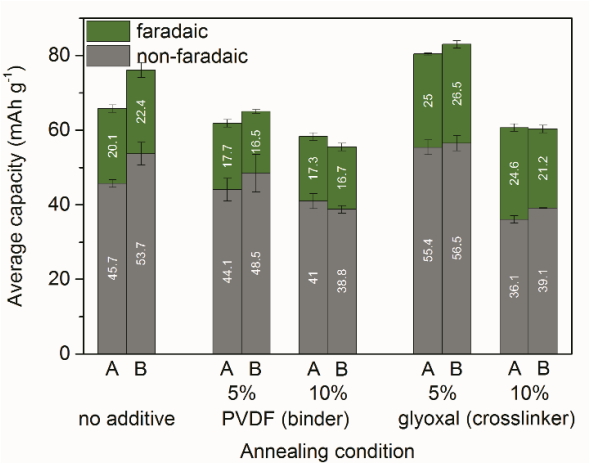

Figure 3-17 Capacity of lignin based electrodes (with high surface area carbon) in dependence on the annealing conditions of the electrodes and of the electrode composition. Lignin and high surface area carbon were blended without any additive or with PVDF (5% or 10% of the total electrode dry weight) or with glyoxal (5% or 10% of the total electrode dry mass) before annealing. A: Annealing at 60 °C for 18 h; B: additional annealing at 80 °C for 2 h. Reprinted by permission.[199] Copyright 2017, Royal Society of Chemistry.

All samples prepared by a further short annealing step provided similar results or an increase in capacity. The use of PVDF at 5 wt% and 10 wt% as binder leads to a decrease in charge storage capacity, particularly the faradaic charge storage contribution, in comparison to the electrode without additive. This is due to a loss of some active component (lignin) by a substitution to the inactive component (PVDF). In contrast, the use of 5 wt% glyoxal as a crosslinker leads to increasing capacity and stability. In the case of the use of 10 wt% glyoxal, the opposite behavior is observed. The capacity significantly decreases, possibly due to a pore blocking by the insufficient flexibility of the material.

In order to investigate different crosslinking agents, glyoxal was replaced by glutaraldehyde (GA), thiophene-2,5-dicarboxaldehyde (ThA), terephthaldehyde (TA), or 5-hydroxymethyl-2-furfuraldehyde (FA). Figure 3-18 summarizes the resulting capacity in comparison to the use of 5 wt% glyoxal. All samples had approximately the same value for non-faradaic charge storage contribution. The faradaic charge storage contribution of the

glyoxal sample was the highest, while the ThA sample exhibited the lowest faradaic charge storage contribution among the tested dialdehyde reagents. Thus, glyoxal, the most sustainable of the tested compounds, also provided the highest capacity.

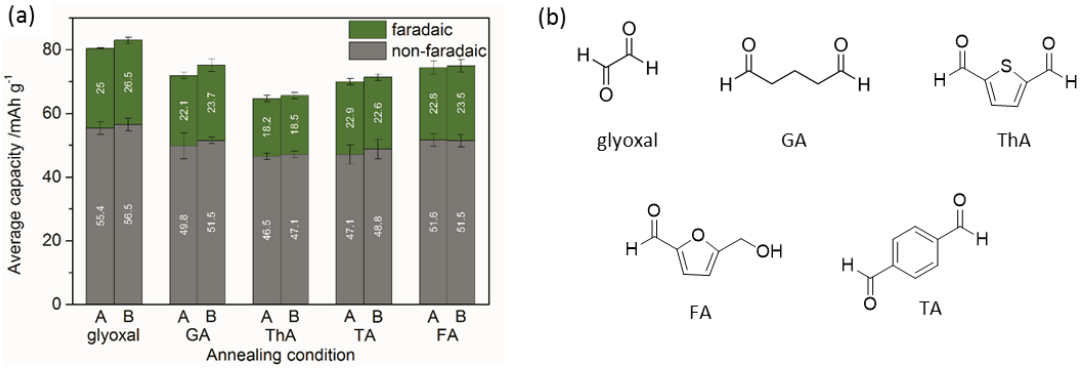

Figure 3-18 Capacity of lignin based electrodes (with high surface area carbon and a crosslinker) in dependence on the electrode composition and the annealing conditions of the electrodes (a). Electrode composition: lignin and high surface active carbon were blended with 5 wt% crosslinker: glyoxal, glutaraldehyde (GA), thiophene-2,5-dicarboxaldehyde (ThA), terephthaldehyde (TA), or 5-hydroxymethyl-2-furfuraldehyde (FA) (b). Annealing conditions, A: Annealing at 60 °C for 18 h; B: additional annealing at 80 °C for 2 h. Reprinted and adapted by permission.[199] Copyright 2017, Royal Society of Chemistry.

The rate performance and stepwise cycling stability were tested by galvanostatic charge-discharge measurements. The electrode based on glyoxalated lignin was selected for comparison of two different electrode formations: lignin crosslinking with glyoxal before and during electrode fabrication. Figure 3-19 (a-b) presents the charge-discharge curves at different current densities. The curves exhibit a nonlinear potential as a function of capacity indicating the influence of the battery-like charge storage accompanied with the EDL charge storage. The hint of a slight plateau region is around 0.4 V to 0.6 V which is in good agreement with the redox couple peak in the CV profiles originating from the quinone/hydroquinone couple. The highest capacity was observed in the glyoxalated lignin based electrode crosslinked during electrode fabrication with approximately 80 mAh g^{-1} at a discharge rate of 0.2 A g^{-1}. Electrodes of the same composition but different fabrication approach show a lower capacity of approximately 45 mAh g^{-1} at the same discharge rate. Figure 3-19 (c-d) reveals the rate performance and cycling stability for 100 cycles of the glyoxalated lignin based electrodes with the same composition fabricated using both approaches.

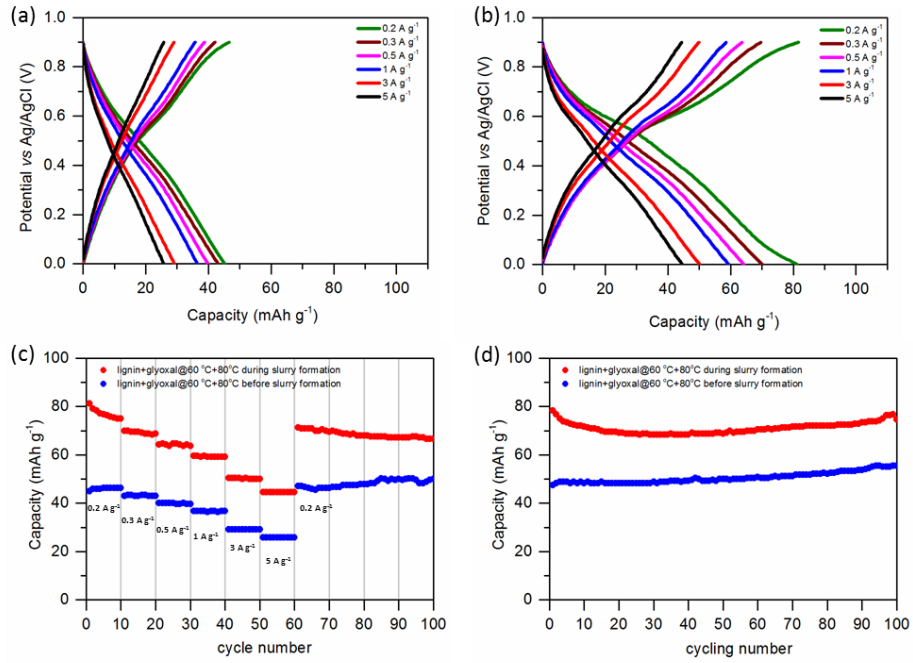

Figure 3-19 Galvanostatic charge-discharge measurements of glyoxalated lignin based electrodes, which were annealed at 60 °C for 18 h before electrode formation (a) and in which lignin was heat treated with glyoxal at 60 °C for 18 h and at 80 °C for 2 h during electrode formation (b). Rate performance at different current densities as denoted in the figures (c) and cycling stability at a current density of 0.2 A g^{-1}. Reprinted by permission.[199] Copyright 2017, Royal Society of Chemistry.

The glyoxalated lignin based electrode which is crosslinked during electrode fabrication exhibits good rate performance at a high discharge rate of 5 A g^{-1} (still giving a capacity of 44 mAh g^{-1}) and remaining constant capacity after cycling for 100 cycles. This indicates the stability of crosslinked lignin with glyoxal during the electrode formation approach. Comparing with the other electrode fabrication approach (crosslinking lignin before electrode formation), an enhanced performance is clearly observed.

To further prove the influence of the redox reaction in lignin, a comparison of charge storage capacity between crosslinked lignin based composite electrodes and carbon electrode is shown in Figure 3-20. The crosslinked lignin based composite electrode (crosslinking with glyoxal during electrode preparation) obviously presents a significantly higher capacity (62 mAh g^{-1} at current density of 0.5 A g^{-1}) than the electrode without lignin (50 mAh g^{-1} at current density of 0.5 A g^{-1}). In contrast, a substantially lower capacity is presented in the case of the crosslinked lignin based electrode in which lignin was crosslinked before electrode formation. This shows that the crosslinking the lignin before the electrode preparation is an inferior process due to the reduction in the efficiency

of charge storage on the surface of carbon. As discussed above, this is a result of insufficient contact of the crosslinked lignin to the carbon surface and partial pore blocking by the large particles of crosslinked lignin with high molecular weight.

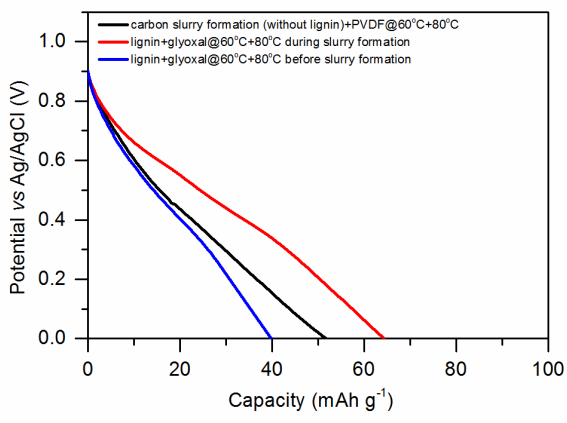

Figure 3-20 Galvanostatic discharge curves of glyoxalated lignin based electrodes with two approaches of electrode formation and a carbon electrode (without lignin) as indicated at current densities 0.5 A g^{-1}. Reprinted by permission.[199] Copyright 2017, Royal Society of Chemistry.

3.4 Conclusion

A new route to the fabrication of a binder-free lignin carbon composite electrode with a more benign crosslinker was successful with a facile two-step process. High molecular weight of lignin was achieved by crosslinking with glyoxal, a sustainable dialdehyde crosslinkers, under air atmosphere and mild conditions. The order of steps in electrode fabrication is important to improve stability and charge storage capacity. Crosslinking lignin during slurry formulation yields a higher charge storage capacity compared to the use of crosslinked lignin, which was synthesized prior to blending with carbon, since the use of lignin crosslinked prior to slurry formulation leads to insoluble lignin particles and an overall low capacity of the resulting electrode. A glyoxalated lignin composite electrode benefits from a combination of faradaic and nonfaradaic charge storage contributions and reaches a capacity of 80 mAh g^{-1} at a discharge rate of 0.2 A g^{-1} with a good rate performance and cycling stability over 100 cycles.

4. Oxidation of Kraft lignin for cathode materials

4.1 Background and objective

Even though lignin possesses many phenolic functional groups, most of them are not in an electroactive form. While hydroquinone or quinone groups contribute to charge storage, most functional groups in lignin are in the form of methyl phenyl ethers or even diphenyl ethers. Free methoxy or dimethoxy phenol groups can be converted into hydroquinone moieties after demethylation and can subsequently form quinone moieties by electrochemical oxidation (as discussed in Chapter 2 with demethylation in the first oxidation scan of CV). Nevertheless, not all methoxy groups are converted, depending on the electrolyte accessibility of lignin, leading to decreased charge storage compared to the theoretic capacity. Therefore, chemical oxidation of lignin before investigation of charge storage may be a simple approach to achieve as many electroactive sites in lignin as possible. The aim of this chapter is to increase the amount of active groups in lignin by using a direct chemical oxidation reaction and testing its practical battery application in lithium based systems.

Bitenc *et al.* synthesized a poly(hydrobenzoquinonyl-benzoquinonyl sulfide) polymer and investigated the electrochemical activity in LIBs (with 1 M LiTFSI in DOL/monoglyme electrolyte). The results showed that the polymer contains much more hydroquinone than benzoquinone groups and exhibited a gradually increasing capacity after the first 20 cycles. As a result of the activation processes during the first 20 cycles, hydroquinone moieties are first lithiated and subsequently oxidized to quinone ones[218] to finally reach equilibrium. Pirnat *et al.* reported an irreversible reaction occurring in the molecule of 1,2,4,5-tetrahydroxybenzene or 1,4-dihydroxy-2,5-dimethoxybenzene structures in the first oxidation cycle tested in a Li battery system (1 M solution of lithium hexafluorophosphate ($LiPF_6$) in a mixture of ethylene carbonate (EC) and diethylene carbonate (DEC) electrolyte and metallic Li as anode) (Figure 4-1 (a-b)). The original of the irreversible charge consumption was not entirely clear; however, the most probable explanation attributed it to the reaction between the electrolyte and the hydroxyl groups.[219] These results show that hydroquinone structures, similar in structure to the G and S units in lignin, may undergo irreversible redox reactions in LIB systems. They also reported a synthesis of a benzoquinone-formaldehyde based polymer by polymerization of

hydroquinone and formaldehyde followed by an oxidation process (Figure 4-1 (c)) and determination of the electrochemical activity in a 1 M lithium bis(trifluoromethanesulfonyl)imide in 1,3-dioxolane/dimethoxyethane (LiTFSI DOL/DME electrolyte. The highest electrochemical activity was obtained with the highest ratio of quinone to hydroquinone in the tested polymer, although both are expected to be electroactive as they constitute a redox couple.[169] This suggests that not only methoxy groups in lignin may be disadvantageous for charge storage in lithium battery systems but also hydroxyl groups, and polymers based on hydroquinone are less electroactive in LIBs compared to those based on benzoquinone.

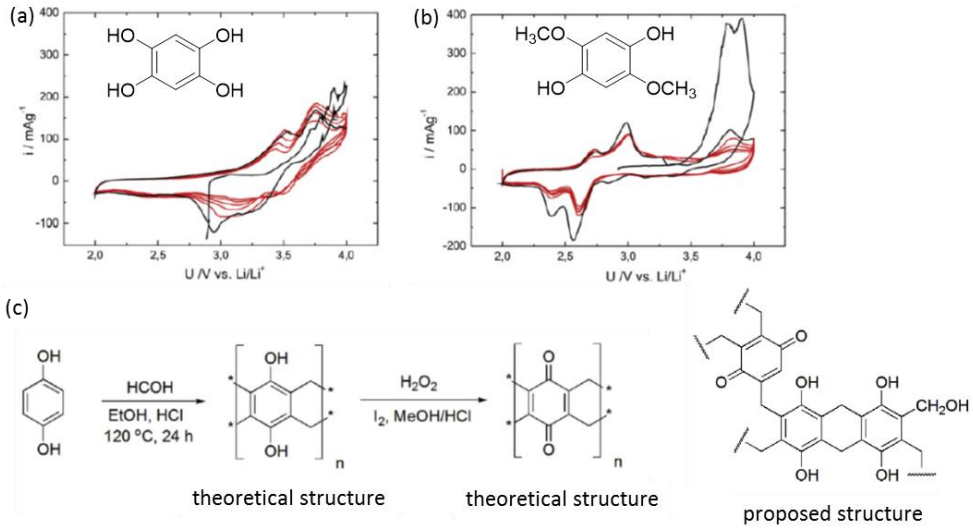

Figure 4-1 CV scans in the first of 5 cycles of samples with redox activity (a) 1,2,4,5-tetrahydroxybenzene and (b) 1,4-dihydroxy-2,5-dimethoxybenzene measured in 1 M $LiPF_6$ EC/DEC 1:1 v/v electrolyte. The black curve corresponds to the first cycle. Reprinted by permission.[219] Copyright 2013, Elsevier. (c)The reaction scheme and proposed structure of a benzoquinone-formaldehyde based polymer. Reprinted by permission.[169] Copyright 2013, Elsevier.

Thus, in order to improve the electrochemical activity of lignin in LIB application, an increase of the quinone to hydroquinone ratio may be an important factor. Conversion of terminal Ph-OH groups in lignin (HP, G, and S units) to the active quinone form can be affected by the oxidation methods. According to the results in Chapter 3, the appearance of some quinone moieties after annealing at elevated temperature resulted from a partial air oxidation in lignin. This is a simple oxidation route without chemicals which might be suitable for LIB application. In general, various more powerful chemical oxidation methods of lignin have been reported over the years.[90,110,220] Most oxidation reactions were utilized to generate valuable aromatic primary feedstock chemicals such as vanillin,

vanillic acid, syringic acid, and so on, which can be further applied in chemical industry. Cleavage of linkage bonds in lignin structure or even break-up of the aromatic ring is the result when strong oxidizing agents such as permanganate, molecular oxygen, and hydrogenperoxide are used.[90] Furthermore, a number of strategies with different catalysts have also been widely studied such as organometallic catalyzed oxidation,[221-225] biomimetic oxidation methods,[226-228] and enzyme-based oxidation methods.[192,220,229]

A group of milder oxidizing agents has been applied as an alternative to limit oxidation to specific groups and keep the aromatic ring intact. For example, sodium periodate[230,231] and Fremy's salt reagent are normally used for the determination of free Ph-OH groups (HP, G, and S units) in lignin. However, these oxidizing reagents have some limitations, such as a ring opening to generate free acid groups of peroxidated lignin product and the high cost of Fremy's salt.

Among the various synthetic methods of quinone derivatives,[232,233] oxidative dealkylation, especially demethylation, of hydroquinone dimethyl ethers is one of the most effective methods. Because the methyl ethers of phenol derivatives are quite stable under various reaction conditions they may require an additional demethylation step. Several oxidizing reagents for the oxidative demethylation reaction can generate quinone from dimethoxybenzene such as concentrated nitric acid (HNO_3),[234] silver oxide (AgO),[235,236] cerium ammonium nitrate (CAN),[233,237] and *N*-bromosuccinimide (NBS).[238] Oxidative demethylation by HNO_3 provides low yield and side reaction products (nitration of the aromatic ring) under vigorous conditions, while, AgO and NBS are expensive reagents that also work in strong acidic condition leading to complicated side reactions.[238] CAN has become the most versatile oxidizing agent in the synthesis of quinones, particularly in terms of the effective oxidative demethylation of dimethoxybenzene. The reaction can be performed without strong acid media and it is generally a relatively fast reaction at room temperature. It is well known that oxidation of 1,4-dimethoxybenzene derivatives with CAN yields the corresponding quinones, and occasionally diquinones are observed as byproducts (or sometimes being as the major product).[233,237]

This chapter aims to improve the amount of quinone moieties in lignin by oxidation of phenolic methoxy groups, the main type of Ph-OH functional groups in lignin, by both methods: simple air oxidation under elevated temperature, and using CAN as an oxidizing agent under mild conditions. 2-Methoxy-4-methylphenol (MMP) was used as a lignin

model compound to confirm the oxidation demethylation method with CAN before applying it to Kraft lignin. The characterization of oxidized lignin model compounds was performed by FTIR, ^{1}H and ^{13}C NMR, as well as mass spectrometry (MS). The possible products of lignin oxidation were estimated from the results obtained from the lignin model compound. Qualitative analysis of oxidized lignin samples was evaluated by various solid state techniques such as FTIR and UV-Vis. Electrodes were fabricated to test lithium battery application compared to an unmodified lignin composite electrode.

4.2 Battery testing of the air-oxidized lignin based electrode

As discussed in Chapter 3, the oxidation of lignin can be occurred by thermal treatment in the presence of glyoxal leading to a generation of some quinone moieties. Thus, it might be useful to test in LIB systems. First, it was tested for stability in lithium salt electrolytes with two conventional LIB electrolytes: 1 M lithium hexafluorophosphate in ethylene carbonate/diethylene carbonate ($LiPF_6$ EC/DEC, E1) and 1 M LiTFSI DOL/DME (E2) as shown in Figure 4-2 (a). Since the heat treatment leads to the oxidation of lignin regardless of the presence of glyoxal, for a comparison, two different lignin composite electrodes were used. Both electrodes used the same amount of lignin (45 wt%), high surface area carbon (50 wt%), and binding additives (5 wt%) and were annealed under the same conditions (optimized conditions from Chapter 3, 60 °C 18 h and then 80 ºC 2 h). One electrode used PVDF as the binder, the other uses glyoxal.

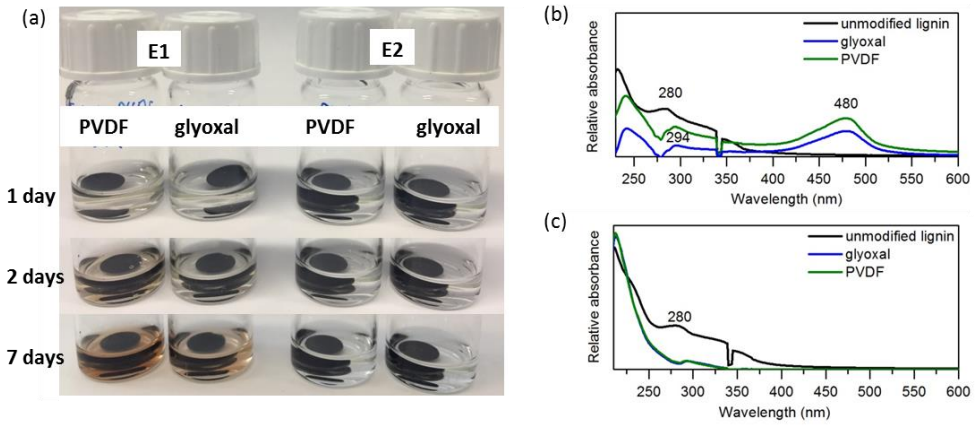

Figure 4-2 (a) Photographs of solubility testing in electrolyte solutions: 1 M $LiPF_6$ EC/DEC (E1) and 1 M LiTFSI DOL/DME (E2) of lignin carbon composite electrodes using either 5 wt% of PVDF as binder or glyoxal as crosslinker (annealing at 60 °C for 18 h then additionally at 80 °C for 2 h). UV-Vis spectra of the electrolyte solution of all samples after 7 days solubility testing compared with unmodified lignin in E1 (b) and E2 (c) at 0.25 mg mL^{-1}, E1 and E2 were used as background. An error from detector appears at around 340 nm.

The electrode using PVDF showed partial dissolution in E1 within 2 days of testing, which increased over a prolonged period of testing, while the other electrode (using glyoxal) remained insoluble within 2 days and presented partial dissolution within 7 days. This proves that the glyoxalated lignin composite electrode is more stable in E1 than an unmodified lignin composite electrode (using as PVDF as the binder). In the case of E2, both were stable for a whole week of testing.

UV-Vis spectroscopy was used to establish whether lignin did dissolve into the electrolyte. After testing the solubility for 7 days, the electrolyte solutions were determined and their UV-Vis spectra are presented in Figure 4-2 (b-c). Almost no dissolution of lignin is observed in E2 for both electrodes, while the presence of the absorption peak at 294 and 480 nm in E1 becomes obvious. This might indicate the dissolution of lignin from such electrodes into E1 and a complexation of lithium salt and lignin.[239] Moreover, a higher absorbance intensity is observed in the case of the lignin based electrode (using PVDF) compared to the glyoxalated lignin based electrode.

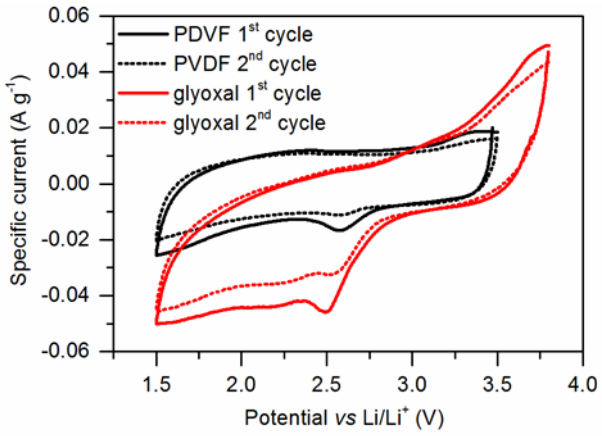

Figure 4-3 CV curves of lignin carbon composite electrodes investigated at 0.1 mV s^{-1} using 5 wt% of PVDF as binder (black) or glyoxal as crosslinker (red) in 1 M LiTFSI DOL/DME, E2. All electrodes were previously annealed at 60 °C for 18 h and additionally at 80 °C for 2 h.

Next, to determine the electrochemical activity, CV was investigated in E2 as shown in Figure 4-3. Since both electrodes were annealed under the same conditions, the existence of quinone functional groups generated from air oxidation during the annealing (as mentioned in chapter 3) should be within approximately the same range. A reduction peak can be observed at 2.5 V *vs.* Li/Li^+ but no oxidation peak appears. In the subsequent cycle, the reduction peak becomes less pronounced. The lignin based electrode using PVDF is less electroactive compared to the glyoxalated lignin based electrode. The results seem to

present an irreversible reduction reaction of the lignin composite electrode in lithium salt electrolytes. Particularly at the first oxidative scan, there is no demethylation and oxidation reaction occurring in the lithium salt electrolyte leading to little electroactive group formation. As observed in Figure 4-3, the glyoxalated lignin based electrode presents a higher current density at the reduction peak. The influence of pore blocking from the use of PVDF binder may reduce the electroactivity of this composite electrode.

Regardless if the electrochemical oxidation does not work, the reduction reaction of quinone moieties in lignin occurs at a potential of about 2.5 V *vs* Li/Li^+ (Figure 4.3). Thus, the glyoxalated lignin based electrode was selected for battery testing performance in terms of primary lithium battery (only discharge capacity from electrochemical reduction of quinone groups). The highest and most stable capacities obtained for benzoquinone polymer electrodes tested in E2 were reported in the potential window 1.5-3.5 V.[169]

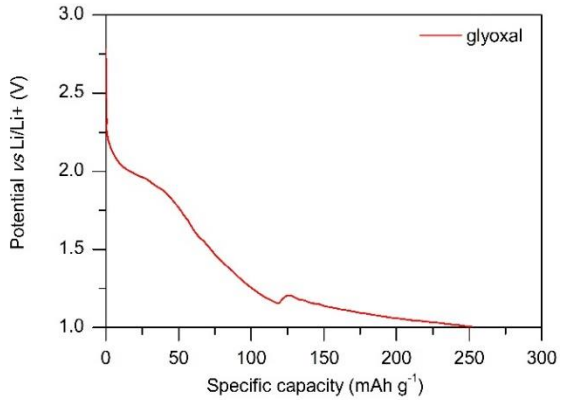

Figure 4-4 Discharge curves of lignin carbon composite electrodes which using 5 wt% glyoxal as crosslinker in 1 M LiTFSI DOL/DME (E2) at a discharge current density of 2 mA g^{-1}.

Galvanostatic discharge was performed as shown in Figure 4-4. The discharge curve indicates that the open circuit voltage (OCV) value for this system is around 2.8 V. Two voltage plateaus are presented in the range of 2.2-1.8 V and 1.5-1.0 V. This is in good agreement with previous reports,[240-242] indicating the reaction of lithium ions and carbonyl groups (3.3-1.5 V) and the participation of hydroxyl groups (below 1.5 V) in the electrochemical reaction. The discharge capacity of 72 mAh g^{-1} in the potential range above 1.5 V is the result of the electrochemical interaction of lithium ions and the carbonyl groups of lignin, while the capacity of 178 mAh g^{-1} in the voltage range from 1.5-1 V during further discharge is due to the reduction of the hydroxyl groups in lignin.

From these results, it is assumed that to improve the discharge capacity and potential of the lignin based electrode in battery application, an increased amount of quinone functional groups in lignin is necessary. Even though the quinone functional group can be simply generated during heating at elevated temperature under the air atmosphere, a greater and more efficient oxidation would be better, as discussed in the following.

4.3 Oxidation reaction of MMP with CAN

The oxidative demethylation of dimethoxybenzene or methoxy phenol can be performed using CAN. In general, the product will not only contain quinone molecules, but also diquinones. During the reaction a radical cation intermediate is formed, that easily reacts with nucleophilic molecules such as the starting material (an aryl ether), or water.[24] To understand the reaction of CAN with lignin, a model molecule, MMP, representing a free Ph-OH type main lignin structure, G units, was first carried out as shown in Scheme 4-1. The possible products shown have been proposed in the literature.[233,237]

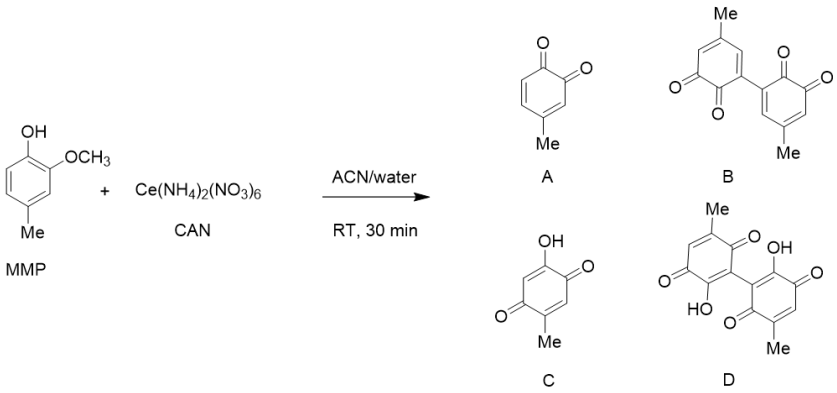

Scheme 4-1 Oxidative demethylation of MMP with CAN and possible products.

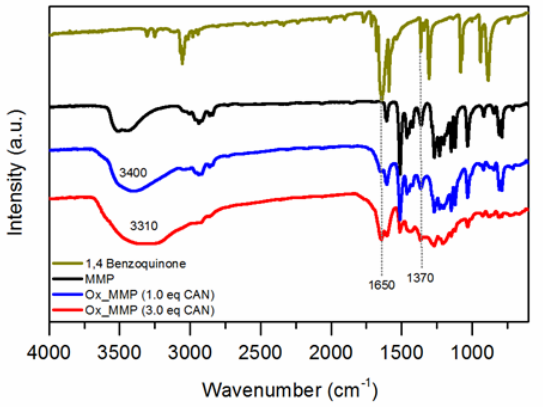

Figure 4-5 FTIR spectra of two oxidized products of MMP compared to 1,4-benzoquinone and MMP starting material.

The FTIR spectra of the oxidized MMP (Ox_MMP) products (Figure 4-5) show the characteristic absorption bands similar to the MMP starting material. The peaks of C-H stretching of CH_3 at 2936 cm^{-1}, the aromatic skeleton C-C stretching in the range of 1600-1400 cm^{-1}, the peaks of C-O stretching in Ph-OH groups, aromatic C-H deformation in range of 1300-1200 cm^{-1} and the peaks of C-O stretching of ether groups at 1035 cm^{-1} remain unchanged in Ox_MMP products. The appearance of a peak at 1650 cm^{-1} along with the increase in the amount of CAN used indicates the formation of quinone functional groups by oxidation (c.f. Figure 4-5, comparison with 1,4-benzoquinone spectrum). The increase in the intensity of the broad OH band in the range of 3300-3400 cm^{-1} may indicate the existence of water molecules. A peak at 1370 cm^{-1} with the increasing amount of CAN used indicates the OH bending of hydroxyl groups. This suggests the formation of *p*-quinone (C) or *p*-diquinone (D) products as shown in Scheme 4-1.

To determine the oxidation product of MMP, the crude product was analyzed by ^{1}H and ^{13}C NMR techniques and mass spectrometry (MS). The mass spectrum (Figure 4-6 (a)) shows the probable occurrence of many products happening during the oxidation reaction.

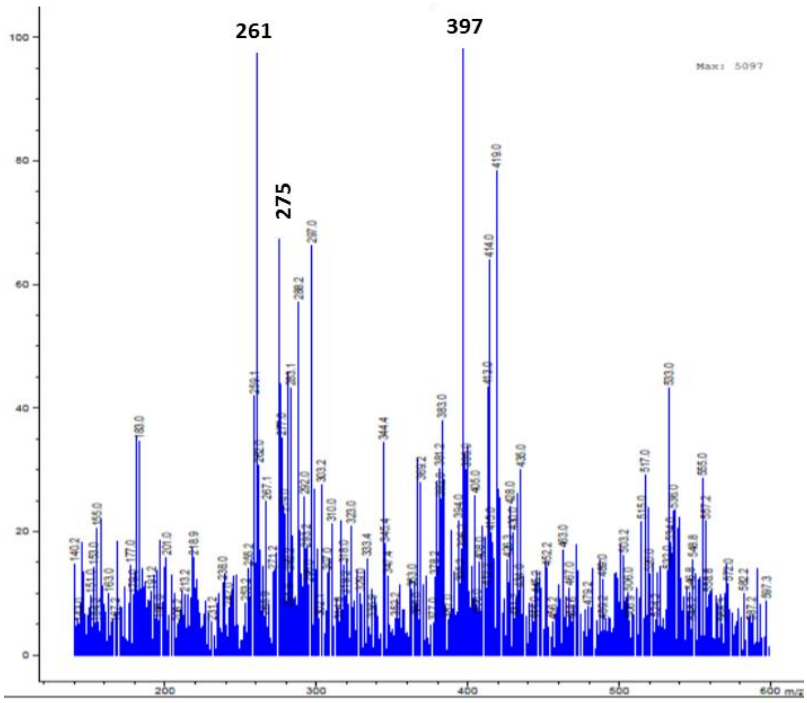

Figure 4-6 Mass spectrum (positive mode) of Ox_MMP (3 eq CAN).

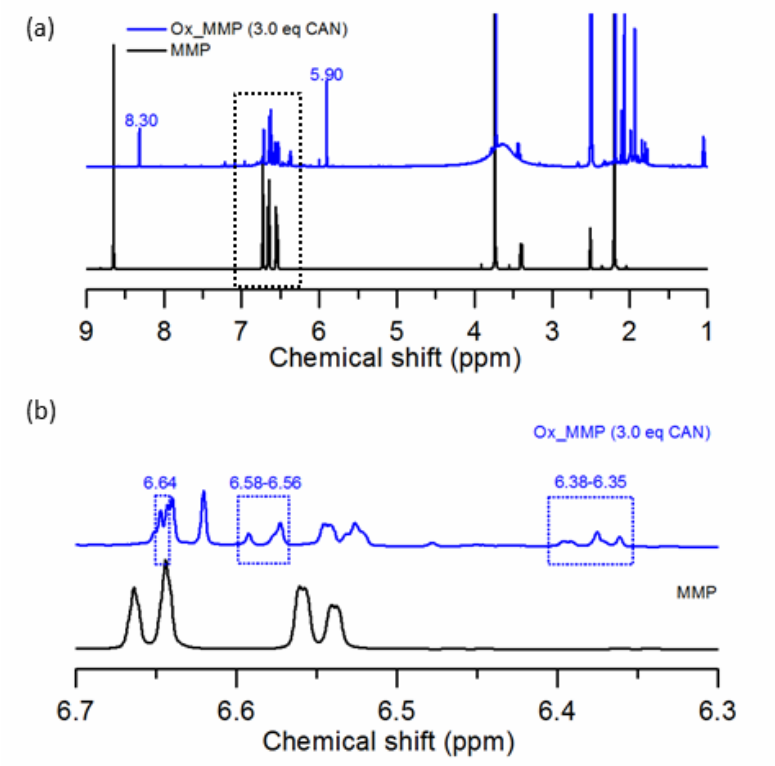

Figure 4-7 ^{1}H NMR spectrum of MMP and Ox_MMP (3 eq CAN) in DMSO-d_6 (a) and a zoom of the area indicated by the black dashed line (b).

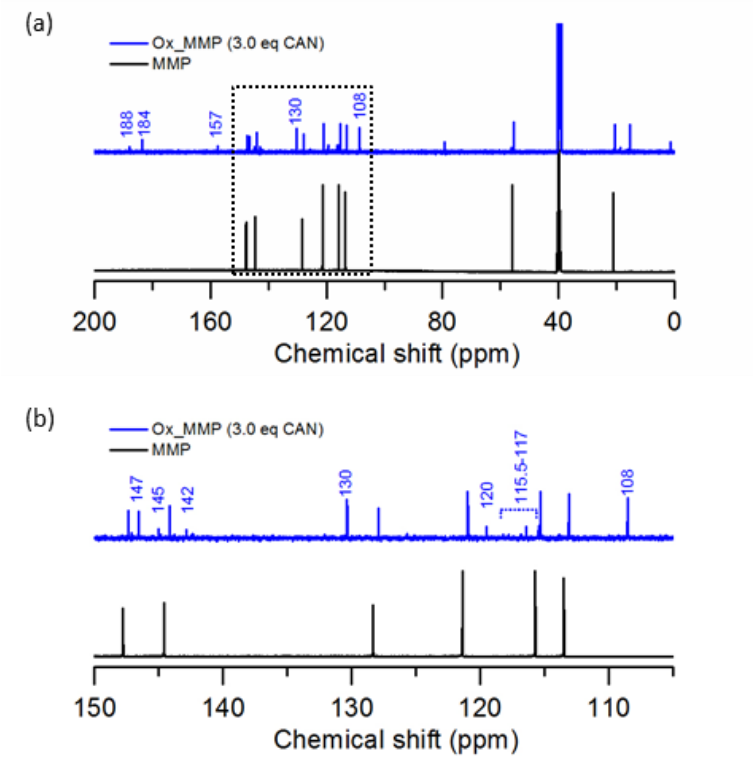

Figure 4-8 ^{13}C NMR spectrum of MMP and Ox_MMP (3 eq CAN) in DMSO-d_6 (a) and a zoom of the area indicated by the black dashed line (b).

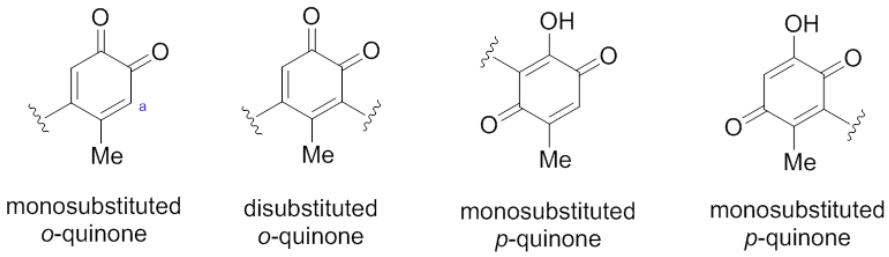

Scheme 4-2 Possibility of substitution on anticipated products from MMP oxidation with 3 eq CAN.

As shown by the ^{1}H NMR spectra of Ox_MMP (3 eq CAN) in Figure 4-7 (a), the appearance of significant peaks at 5.9 ppm may be attributed to the H_a of the monosubstituted *o*-quinone (Scheme 4-2). Another observed peak at 8.3 ppm might derive from protons in *ortho* position to nitrated quinone molecule (from reaction with nitrate groups in CAN). Both quinones might have formed. Some possible structures of the oxidized product regarding the MS, ^{1}H and ^{13}C NMR results may be presented as shown in Scheme 4-3 such as the molecule of hydroquinone-quinone (E), diquinone (F), and the molecules of quinone linked with hydroquinone molecule (G) with M 260, 274, and 396 g mol^{-1}, respectively.

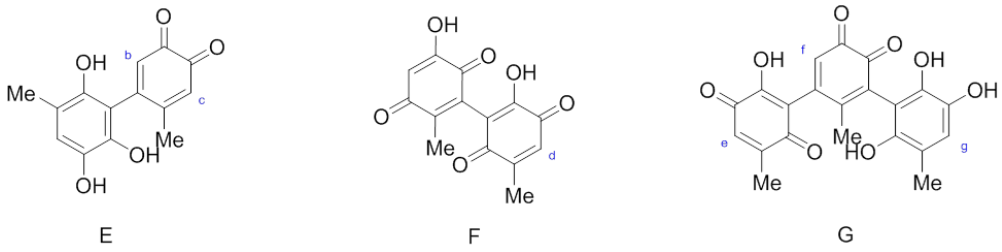

Scheme 4-3 Possible products of MMP oxidation with 3 eq CAN as estimated from the mass spectrum.

Table 4-2 ^{1}H and ^{13} C NMR chemical shift of some proposed oxidized products following Scheme 4-3.

position	^{1}H (ppm)		^{13}C (ppm)	
	expected*	observed	expected*	observed
b	6.5	6.58-6.56	111	108
c	6.0	5.90	114	115.5-117
d	6.7	6.64	131	130
e	6.7	6.64	131	130
f	6.3	6.35-6.38	109	108
g	6.2	6.35-6.38	117	115.5-117
C=O			180-187	184-188
C-O			140-157	142-157

*simulated from a ChemDraw program

The ^{1}H and ^{13}C NMR chemical shift of the proposed products are listed in a comparison between the simulation and observation results (Table 4-2). The main peaks from the quinone carbon at 188 and 184 ppm (C=O) and hydroquinone carbon at 142-152 ppm (C-O) can be clearly seen. Most chemical shifts match with the expected molecules; however, this only provides an idea for the possible products. It may be composed of different *ortho*- and *para*- quinone moieties and a linkage between such molecules.

Although the model compound lacks the complexity of the lignin polymer, the obtained data is very useful for understanding and forecasting possible reactions and products when conducting the same reaction with lignin.

4.4 Oxidation reaction of lignin with CAN

The oxidation reaction of lignin was performed the same way as with MMP. The amount of CAN varied using 0.8, 1, 1.5, and 3 equivalents of CAN with respect to the amount of S and G groups in lignin (3.25 mmol g^{-1} calculated from ^{31}P NMR). The oxidized lignin samples are named as Ox_lignin (n eq CAN), where n refers to the equivalents of CAN used. The solubility of all oxidized lignin samples was tested and the results summarized in Table 4-1.

Table 4-1 Solubility result of oxidized lignin samples in different solvents.

Sample	DMSO	NMP	DMF	THF	M_w	M_n	Đ
Unmodified lignin	+++	+++	+++	+++	4680	3140	1.5
Ox_lignin (0.8 eq CAN)	+++	+++	+++	+++	10800	5350	2.0
Ox_lignin (1.0 eq CAN)	++	++	++	++	8360*	3290*	2.5*
Ox_lignin (1.5 eq CAN)	+	+	+	+	N/A	N/A	N/A
Ox_lignin (3.0 eq CAN)	+	-	-	-	N/A	N/A	N/A

+++: completely dissolved; ++: partly dissolved; +: slightly dissolved; -: not dissolved
*: result obtained from the soluble fraction in NMP
N/A: not available, no measurement
Đ: dispersity (M_w/M_n)

It can be observed that the solubility decreases with the higher amount of CAN used. This is due to the crosslinking of the oxidized lignin sample yielding a high molecular weight. Unfortunately, since most samples are poorly soluble in the solvent used for SEC

measurements, the molecular weight can be determined only for Ox_lignin (0.8 eq CAN) with M_w 10800 and M_n 5350 g mol^{-1} (Đ 2.02) which is higher than unmodified lignin (Table 4-1). The characterization result of the lignin model molecule has shown that the main products are molecules formed by the crosslinking of two or three aromatic molecules. This supports the observation of reduced solubility in oxidized lignin samples due to the assumedly higher amount of molecular weight of the lignin samples with the higher amount of CAN used.

To determine the amount of quinone functional groups after the oxidation of lignin, FTIR, UV-Vis spectrophotometry and ^{31}P NMR (after derivatization) were performed. Figure 4-9 presents the FTIR spectrum of lignin samples with the different amounts of CAN used. It is clear that increasing the amount of CAN used in the oxidation reaction effects an increase in the intensity of the OH broad band (3500-3300 cm^{-1}) and the conjugated C=O stretching band at 1650 cm^{-1} which can be attributed to the increase of OH and quinone functional groups. Moreover, the additional peaks attributed to the aromatic ring skeleton of methylene C-H deformation (1430 cm^{-1}) and C-O stretching in Ph-OH groups (1370 and 1305 cm^{-1}) were observed. Thus the FTIR results are in good agreement with the data obtained from the model substrate investigated.

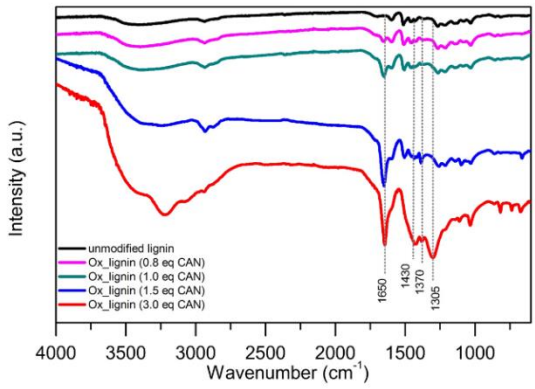

Figure 4-9 FTIR spectra of all oxidized lignin samples as compared with unmodified lignin.

Another technique which can be utilized to determine the presence of quinone functional groups is UV-Vis spectrometry. Since most oxidized lignin samples cannot be completely dissolved in DMSO solvent, only soluble samples were tested, with the UV-Vis spectra shown in Figure 4-10 (a). No additional absorption band for the two oxidized lignin samples (at 0.8 and 1.0 eq CAN) is observed. To compare all oxidized lignin samples, solid state UV-Vis spectrophotometry was applied as an alternative approach. The results

are presented in Figure 4-10 (b). A broadened peak in a range of 450-650 nm appears compared to the unmodified lignin and increases when higher amount of CAN were used. 1,4-Benzoquinone, used as a standard, presents a strong absorption peak at around 450 nm and 650 nm. The broadened band of oxidized lignin samples might present quinone functional groups in a variety of structural environments. Visible absorption spectroscopy is not directly effective for lignin-quinone quantification because of the broad featureless nature of lignin absorption spectra. Thus alternative measurement options were explored.

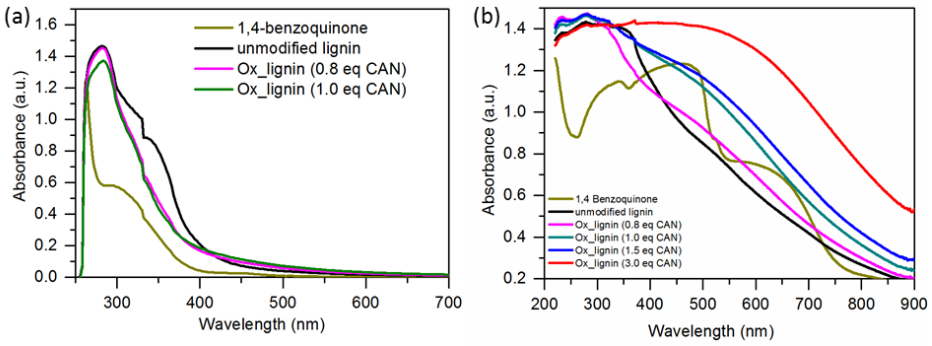

Figure 4-10 UV-Vis spectrum recorded in DMSO (a) and solid state UV–Vis spectrum ($BaSO_4$ as used for background) (b) of oxidized lignin samples as compared with 1,4-benzoquinone and unmodified lignin.

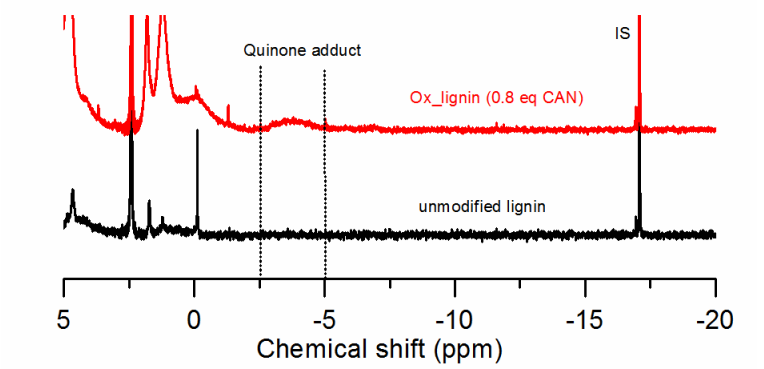

Figure 4-11 ^{31}P NMR spectrum of lignin samples after derivatization with trimethyl phosphite as referenced by tri-*m*-tolylphosphate (internal standard, IS).

There have been reports of the application of trimethylphosphite (TMP) derivatization to quantify *ortho*- and *para*-benzoquinone structures in lignin.[243-245] The stable dimethylphosphate ester products which are generated by the cyclization of quinone moieties with TMP and subsequent hydrolysis are detected by ^{31}P NMR spectroscopy. Unfortunately, only Ox_lignin (0.8 eq CAN) can be completely dissolved in DMSO, so it was compared to unmodified lignin as shown in Figure 4-11. The quinone adduct peak is

observed in the range of -2.5 to -5 ppm as referenced by tri-*m*-tolylphosphate (δ -16.3 ppm) for the sample Ox_lignin (0.8 eq CAN). The amount of quinone content is 0.025 mmol g^{-1} quantified by an integration area of IS. This confirms the successful oxidation to yield the quinone functional groups in lignin. Taking into account the results of previously discussed measurements, it can be expected that a higher amount of quinone content results from increasing the amount of CAN. However, this result is not completely clear since the relevant peak is of fairly low intensity. As discussed earlier, ^{13}C NMR technique is not a quantitative measurement method. It would be better if the other quinone content samples can be determined for a comparison; however, they have solubility limitations.

4.5 Lithium battery application

This application test is performed to test the assumption that increasing the amount of quinone functional groups in lignin could enhance the capacity of the resulting lithium batteries. Two oxidized lignin composite electrodes (using CAN at 1.5 and 3 eq) were assembled for a dissolution test in E2. There is no observable lignin dissolution in E2 within 7 days (Figure 4-12 (a-b)). Also, a UV-Vis spectrum of the E2 used exhibits only a relatively low intensity as shown in Figure 4-12 (c). This suggests that the oxidized lignin composite electrode is stable in E2.

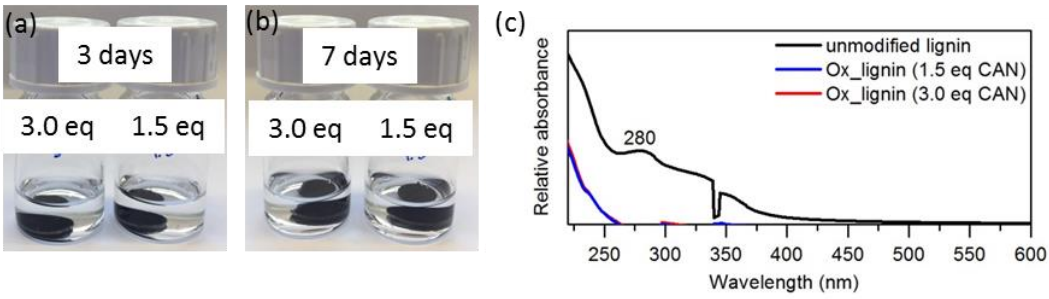

Figure 4-12 Photographs of the solubility testing of oxidized lignin based electrodes (with 3.0 and 1.5 eq CAN) in 1 M LiTFSI DOL/DME (E2) for 3 days (a) and 7 days (b). UV-Vis spectra (c) of the electrolyte solution of all samples after the solubility testing for 7 days compared with unmodified lignin in E2 (at 0.25 mg mL^{-1}), E2 was set as a background. An error from detector appears at around 340 nm.

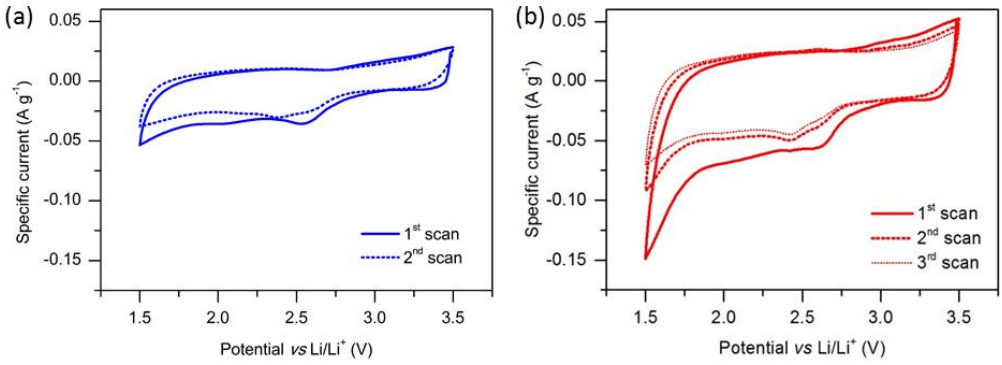

Figure 4-13 CV scans of Ox_lignin based electrodes investigated at 0.1 mV s^{-1} in 1 M LiTFSI DOL/DME, E2, using 50:50 wt% of high surface area carbon and Ox_lignin (1.5 eq CAN) (a) and Ox_lignin (3.0 eq CAN) (b).

CV scans of two oxidized lignin samples with expected high quinone content were selected for investigation in E2 as shown in Figure 4-13 (a-b). The reduction peak appears around 2.4-2.6 V *vs.* Li/Li^+ with a small oxidation peak at 3.0 *vs.* Li/Li^+ in the first scan. The reduction peak then becomes less pronounced and the oxidation peak almost disappears in the subsequent scans. The lignin based electrode using the lower amount CAN (1.5 eq) is less electroactive compared to the one using a higher amount CAN (3.0 eq). The amount of quinone groups is improved by oxidation compared to the lignin samples in chapter 3. However, they still exhibit an irreversible redox conversion in lithium salt electrolyte.

In order to compare the discharge capacity in battery performance to the crosslinked lignin after air-oxidation upon heating (Chapter 4.2), the oxidized lignin samples were tested under the same conditions. The discharge curves are presented in Figure 4-14 showing different electrochemical behaviors. The discharge curve of the Ox_lignin (3.0 eq CAN) based electrode presents a well-defined and sloping plateau in the voltage range of 2.75-2.60 V which is consistent with the appearance of a reduction peak in CV profile. It indicates the reaction of lithium ions and carbonyl groups (in range of 3.3-1.5 V).[240-242] As compared with the crosslinked lignin based electrode (glyoxal), the discharge capacity considerably improves to 272 mAh g^{-1} at a discharge rate of 2 mA g^{-1}. This confirms the successful oxidation reaction with CAN that can increase the amount of quinone moieties more than a typical air oxidation (Chapter 3). Another, lower plateau region is revealed at around 1.5 V attributed to the participation of hydroxyl groups in the electrochemical reaction with a discharge capacity of 450 mAh g^{-1} (1.5-1 V) at a discharge rate of 2 mA g^{-1}.

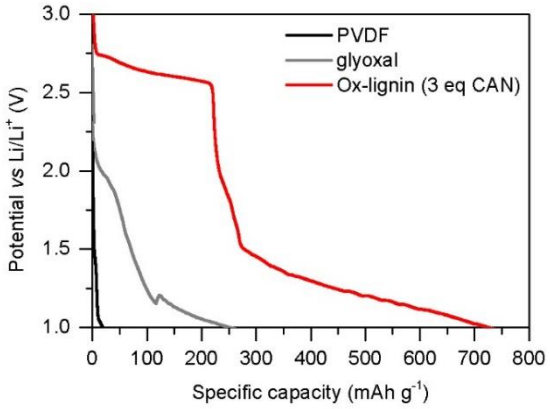

Figure 4-14 Discharge curves of lignin based electrodes recorded in 1 M LiTFSI DOL/DME (E2) at a discharge current density of 2 mA g^{-1}. The figure shows lignin carbon composite electrodes (constant at 50 wt% of high surface area carbon) with different modified lignins: using 45 wt% unmodified lignin with 5 wt% PVDF as binder, with 5 wt% glyoxal as crosslinker annealing at 60 °C for 18 h then additionally at 80 °C for 2 h, using 50 wt% Ox_lignin (3.0 eq CAN).

4.6 Conclusion

By oxidation of lignin with CAN under mild conditions, the quinone content is enhanced. The use of MMP as a lignin model compound allowed for the estimation of possible products from the oxidation reaction with CAN: crosslinked quinone products with the formation of *ortho*- and *para*-quinone functional groups. Thus the oxidation of lignin with CAN not only improves the quinone content leading to enhanced charge storage capacity but also increases the molecular weight of lignin samples leading to increased electrode stability in lithium salt electrolytes. The lithium battery testing revealed a higher capacity of 272 mAh g^{-1} at a discharge rate of 2 mA g^{-1} in the significant high potential range of 2.75-2.5 V due to the increase of the quinone content compared to the glyoxalated lignin based electrode.

5. Conclusion and outlook

The present thesis concerns the challenge of the utilization of lignin for sustainable energy storage applications through chemical modification with more environmental friendly and benign approaches. The aims of this thesis are to contribute to the understanding of the fundamental electrochemical behavior of lignin composite electrodes, as well as to study the influencing parameters of charge storage performance, the modification of the chemical structure of lignin, and the improvement of the electrode fabrication process to achieve high performance.

In the second chapter, the utilization of the available and cheap Kraft lignin in combination with sustainable conductive carbon for energy storage devices was explored. The contribution of faradaic and non-faradaic charge storage in the lignin composite electrode fabricated from lignin and conductive carbon was studied. In addition to the electric double layer charge storage capacity of the high surface area conductive carbon, the characteristic redox reaction of the quinone/hydroquinone redox couple in lignin was observed contributing an additional faradaic part to the charge storage of the lignin composite electrode. The charge storage capacity of the lignin composite electrode is mainly based on the surface area of conductive carbon and the composite ratio of lignin and carbon. The important factors at play for achieving high faradaic charge storage capacity contribute to high surface area, accessibility of redox sites in lignin and their interaction with conductive additives. A thinner layer of lignin covering the high surface area of carbon facilitates the electron transfer process with a shorter pathway from the active sites of nonconductive lignin to the current collector leading to the improvement of faradaic charge storage capacity. The best capacity achieved reaches 80 mAh g^{-1} (at current density of 0.075 A g^{-1}, mass of total material) of the electrode which is made from commercial and unmodified lignin and conductive carbon.

In the third chapter, a composite electrode free of fluorinated binder was successfully fabricated by a combination of the advantages of lignin: the active component (hydroquinone motif) for the high charge storage and the binding property for the stability of the electrode. In order to improve the stability and performance of lignin based electrodes, a modification by crosslinking with glyoxal at elevated temperature has been introduced. A higher molecular weight and decreased solubility of crosslinked lignin was

observed. Moreover, the order of processing steps for electrode fabrication is important to enhance faradaic charge storage capacity. The use of high molecular weight crosslinked lignin to prepare the composite electrode causes decreased contact and pore blocking on the high surface area carbon leading to less efficient charge storage. However, if crosslinking with glyoxal is performed after establishing a good contact between lignin and carbon the result is that the highest capacity of both faradaic and nonfaradaic charge storage are achieved. Therefore, in this chapter, a new route for the fabrication of the binder-free lignin based electrodes was proposed through a facile two-step process: formation of lignin-carbon composites first and the subsequent crosslinking of lignin on the carbon by glyoxal by annealing at elevated temperature. The final electrodes benefit from the combined faradaic and nonfaradaic charge storage and the characteristic combination of battery-like and capacitor-like behavior reaching a capacity of 80 mAh g^{-1} at a discharge rate of 0.2 A g^{-1}. The use of sustainable glyoxal and the biopolymer lignin is beneficial to obtain a more environmental friendly, cheap, safe, benign, and halogen-free material and hence contributes to greener storage devices.

In the fourth chapter, in order to enhance the amount of redox active functional groups in lignin, oxidation with cerium ammonium nitrate (CAN) was carried out under mild conditions. The advantage of oxidation by CAN is the direct oxidative demethylation of methoxy phenolic groups in lignin to quinone. A lignin model compound which is less complex in structure was employed to understand oxidation with CAN and to forecast the obtained products upon its application to lignin. As a result of the oxidation, not only is quinone obtained, but some crosslinked quinone products are observed and the stability is increased, leading to the decreased solubility of oxidized lignin based electrodes in lithium salt electrolyte. The lithium battery testing revealed a high capacity of 272 mAh g^{-1} at a discharge rate of 2 mA g^{-1} within the significantly high potential range of 2.75-2.5 V, superior to the performance of a glyoxalated lignin based electrode which was only partly air oxidized by heat treatment. This is due to a significant increase of quinone moieties in lignin. Thus, this result reveals good prospects for the use of Kraft lignin for lithium battery cathode with reasonable discharge capacity at high potential.

Interesting further research may address the improvement of the charge storage capacity on the lignin based electrode by applying the oxidation of lignin *in situ* on the lignin based electrode. One-step oxidation by the direct UV irradiation of alkali lignin in THF solution

for lignin color fading process has been reported in literature. The mechanism occurs through the photo-oxidation of phenolic hydroxyl and some methoxy groups into quinone structures and the subsequent degradation into aliphatic acid structures.[246] This method could probably be applied to the lignin based electrode; however, the reaction time and solvent should be studied in further detail. It is a greener and more effective approach for the oxidation of lignin, and the use of metal-free chemicals to avoid any influence of the remaining metal after the oxidation reaction in lignin structure is also preferable. Furthermore, the improvement of electrode fabrication is also important for future research. Electrospinning is a method of interest due to the possibility of providing thin fibers of sub-micrometer diameters. Lignin fiber may be decorated with conductive carbon to improve the conductivity of the electrode. Blending synthetic polymers (poly(ethylene oxide), or poly(vinyl acetate)) with lignin in solution before spinning helps to improve the spinning performance. So, there might be a possible approach to blending with conducting polymers as well. This technique might be able to improve the fabrication of the lignin based electrode with conductive additives by yielding a more homogeneous, porous, and thin film and finally leading to the enhancement of the charge storage capacity.

A. Materials and methods

A.1 Materials

All the chemicals were of reagent grade and used as received, without further purifications. All the deuterated solvents (DMSO-d_6 and $CDCl_3$) were purchased from Sigma Aldrich. All solvents used for analysis were of analytical grade.

A.1.1 Materials for chapter 2

Kraft lignin from southern pine trees was obtained from Domtar. Polyvinylidene fluoride (PVDF) was purchased from MTI Corporation. *N*-Methyl-2-pyrrolidone (NMP), *N*,*N*-dimethyl formamide (DMF), cyclohexanol, and 2-chloro-4,4,5,5-tetramethyl-1,3,2-dioxaphospholane (TMDP) were obtained from Sigma Aldrich. Chromium (III) acetylacetonate was purchased from Acros Organics. Pyridine was obtained from Alfa Aesar. Two types of conductive carbons, one with low specific surface area of 167 $m^2\ g^{-1}$ (C^L) and one with high specific surface area of 858 $m^2\ g^{-1}$ (C^H) were synthesized from renewable resources as described elsewhere.[247] Graphite foil as current collector was kindly donated by Henschke GmbH, Germany.

A.1.2 Materials for chapter 3

A high surface active carbon AB-520 with specific surface area of 2000 $m^2\ g^{-1}$ was purchased from MTI Corporation. Glyoxal (40 wt% aqueous solution, Carl Roth), glutaraldehyde (50 wt% aqueous solution, Fisher Scientific), thiophene-2,5-dicarboxaldehyde (Aldrich), 5-hydroxymethyl-2-furfuraldehyde (Acros), and terephthaldehyde (Acros) were used as received. 2,3,4,5,6-Pentafluorobenzaldehyde (Aldrich) and acetic anhydride (Alfa Aesar) were used as received.

A.1.3 Materials for chapter 4

Tri-*m*-tolylphosphate was received from TCI Chemicals. Trimethyl phosphite and Cerium ammonium nitrate (CAN) were purchased from Aldrich. Lithium ribbon, lithium bis(trifluoromethanesulfonyl)imide (LiTFSI) and lithium hexafluorophosphate ($LiPF_6$), dimethyloxyethane (DME), and diethyl carbonate (DEC) were purchased from Sigma-Aldrich. 1,3-dioxolane (DOL) and ethylene carbonate (EC) were obtained from Alfa Aesar.

A.2 Methods

Electrochemical measurements

It is a technique concerned with the interrelation of the movement of electrons and chemical effects which studies the change of chemical reactions by the passage of an electric current. Here, CV and galvanostatic charge discharge are mainly performed. These techniques are useful for characterizing the performance of electrodes as they most accurately replicate the charging and discharging processes for electrodes when used in practical applications.

Cyclic voltammetry (CV) is a common technique for the investigation of electrochemical processes by measurement of the current response (I) during an applied potential within a defined potential range (E) in dependence on time (scan rate, ν). CV is performed by applying the potential ramp to a working electrode to gradually change potential and then reverses the scan, returning to the initial potential. The CV graph is plotted of current versus the applied potential. The chemical reactions: redox reactions as well as adsorption phenomena (e.g., electrical double layer capacitive, EDL, behavior) can be identified by current change. Particularly, redox reactions which occur at an individual redox potential value of each redox active component can be identified by current changes. Therefore, the CV profile of a redox reaction is a characteristic feature displayed by a potential-dependent curve. In contrast, EDL and pseudocapacitive behavior present in a CV profile shows a potential-independent curve. CV provides useful information concerning the redox reactions, reversibility, and side reactions in the cells. A cyclic voltammogram featuring the typical behavior of the lignin carbon composite electrode (in this thesis) is depicted in Figure A-1.

CV was conducted using BioLogic MPG2 potentiostats. The charge storage capacity is calculated from CV curve to study the charge storage contribution of faradaic and nonfaradaic process. In this research, a typical CV profile feature shows a large separation of oxidative and reductive scan with distinct redox peaks in addition to a rectangular area of the lignin carbon composite electrode. The overall charge storage capacity is calculated following eqn (3):

$$Capacity = \int \frac{IdE}{\nu} \times \frac{1}{2m\Delta E} \ (mAh\ g^{-1}) \qquad \text{eqn (3)}$$

where I is the current (A), E is voltage (V), m is mass of the electrode (g), ΔE is the voltage range (V) and ν is the scan rate (V s^{-1}). Integration is carried out over a whole cycle of CV curve. For calculation of error bars, three measurements each were averaged.

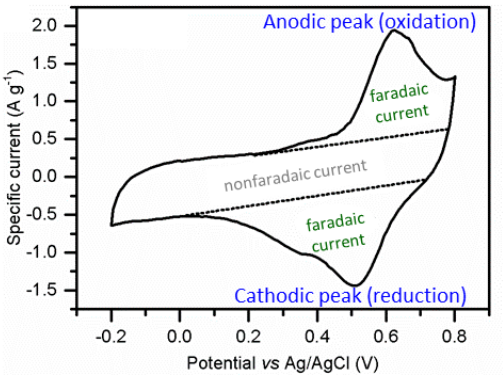

Figure A-1 The typical appearance of a CV curve of lignin carbon composite electrode.

The individual charge storage contributions are roughly indicated as in Figure A-1. For estimating faradaic contributions of redox processes in lignin, the integrate redox peaks only is used for calculation following eqn (3) while EDL capacitance results from subtracting the peak area from the maximal integration area. However, as comparison with a carbon electrode (without lignin), it shows almost exactly the same CV behavior as obtained by estimation by the dashed line in Figure A-1.

Galvanostatic Charge-Discharge or Cyclic Charge-Discharge is the standard technique used to test the performance and cycle-life of capacitors and batteries in order to estimate the practical cell capacity and determine the degradation processes. Most often, charge and discharge are conducted at constant current within the defined voltage window and recorded in a unit of time necessary for each cycle. A repetitive and continuous loop of charging and discharging is called a cycle. An example of a typical galvanostatic profile can be seen in Figure A-2. In this thesis, the capacity (mAh g^{-1}) of battery-like electrodes (non-linear galvanostatic curve) derived from the galvanic charge/discharge curve is calculated following eqn (4):[248]

$$Capacity = \frac{It}{m.3.6} \qquad \text{eqn (4)}$$

where t is the charge or discharge duration (s). For calculation of error bars, three measurements each were averaged.

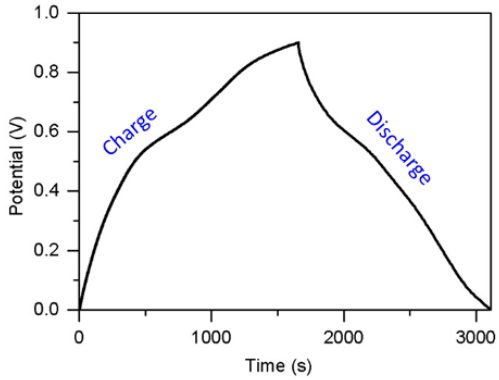

Figure A-2 The typical galvanostatic charge-discharge curve of lignin carbon composite electrode with potential window of 0.0-0.9 V at constant current density.

Fourier transform-infrared spectroscopy (FT-IR)

FT-IR relies on the detection of the absorption of specific wavelengths by molecules in the infra-red region of the electromagnetic spectrum. This absorption corresponds specifically to the chemical bonds in the molecule. The frequency range is measured as wave numbers typically over the range 4000-600 cm^{-1}. Structural information about chemical bonds and functional groups of the molecules can be obtained. An attenuated total reflection (ATR) accessory operates by measuring the changes that occur in a totally internally reflected infrared beam when the beam comes into contact with a sample in which an evanescent wave is employed for analysis. FT-IR spectra were recorded on a Nicolet iS5-FT-IR spectrometer with a Single Reflection Diamond ATR support.

Size exclusion chromatography (SEC)

SEC measurements are performed to determine the mass average molecular weight (M_w) of a polymer. M_w is calculated by comparison of its hydrodynamic volume with a polystyrene (PS) calibration standard in the case of lignin and modified lignin. The analysis is performed in NMP solvent by a Thermo Separation Products apparatus equipped with a Shodex RI-71 detector with 0.05 mol L^{-1} LiBr as internal standard at 70 °C. A column system equipped with a PSS GRAM 100/1000 column (8 × 300 mm, 7 µm particle size and porosity between 100-1000 Å) and a PSS GRAM pre-column (8 × 50 mm) was used.

Electrospray ionization-mass spectrometry (ESI-MS)

Mass spectrometry is an analytical technique providing both qualitative (structure) and quantitative (molecular mass) information. The molecules of interest are first transferred to ionized form (positive or negative charges) then passed through the mass analyzer and detector. A mass spectrum displays the relative abundance of the signals according to their mass to charge (m/z) ratio. Electrospray ionization is useful technique used in mass spectrometry to produce ionic species by an electrospray with a high voltage. ESI is a so-called 'soft ionization' technique, since there is very little fragmentation. It is typically used to determine the molecular weights of macromolecules. ESI-mass spectra were recorded on a Thermo Scientific Velos Pro LC-MS using acetonitrile as the solvent with formic acid as the ionization agent.

Nuclear magnetic resonance (NMR)

^{1}H-NMR spectra were recorded on a Bruker ascend400 Avance III with a Prodigy-probe in deuterated solvents. Acetylated lignins (5-10 mg) were dissolved in $CDCl_3$ (0.5 mL) with 1.5 µL of 2,3,4,5,6-pentafluorobenzaldehyde as an internal standard. Chemical shift of the samples are referred to the internal standard.

^{31}P NMR spectra were detected on a Varian 400 MR with an OneNMR-Probe.
Determination of hydroxyl groups in lignin: chemical shift of the samples are referred to an internal standard (cyclohexanol) for determine hydroxyl functional groups in lignin and modified lignin.[7,152,215] The most common phosphitylating reagent is TMDP which reacts with hydroxyl groups in lignin arising from aliphatic, phenolic and carboxylic acids groups in the presence pyridine to yield different phosphitylated products as seen in Figure A-3.

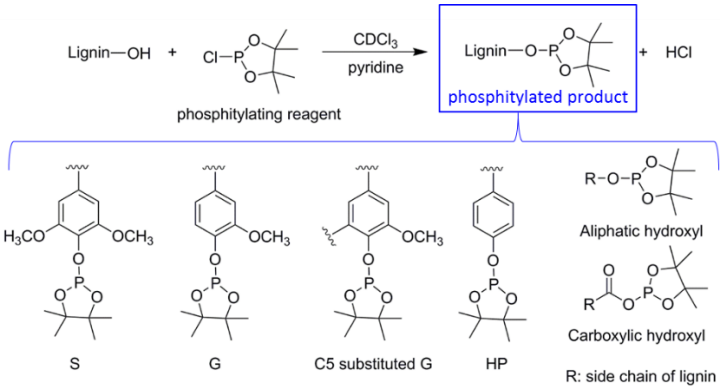

Figure A-3 Phosphitylation of hydroxyl groups in lignin structural units with TMDP.

Determination of quinone content: the internal standard tri-*m*-tolylphosphate was used both for quantification and as a shift reference. The reaction of trimethylphosphite (TMP) is applied to quantify *ortho*- and *para*-benzoquinone structures in lignin.[243-245] The stable dimethylphosphate ester products generated by cyclization of quinone moieties with TMP and subsequent hydrolysis (Figure A-4) are detected by ^{31}P NMR spectroscopy.

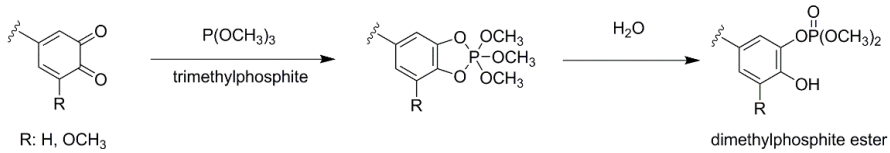

Figure A-4 Reaction of TMP with *ortho*-quinone derivative.

Scanning electron microscope (SEM)

This method is suitable for a 3-D imaging of the surface topology of sample. The specimens are deposited on an aluminum holder coated by carbon. During the analysis, an electron beam is directed onto the surface of sample and the scattered electrons are detected. The sample must be conductive, so normally the samples were sputter-coated with Au/Pd alloy before examination. SEM images were recorded on a Zeiss Leo 1550 Gemini microscope.

Thermogravimetric Analysis (TGA)

TGA analysis was performed using a TG 209F1 Libra TGA209F1D-0036-L instrument, under nitrogen atmosphere or synthetic air as indicated in the results, with a heating ramp from 25 to 1000 °C and a heating rate of 10 K min^{-1}. During TGA analysis the sample is heated and the loss of weight is recorded accordingly by the NETZSCH Proteus software. The TGA curves reveal the mass loss of the samples in relation to the temperature of thermal degradation, while the first derivative of that curve (DTG) shows the corresponding rate of mass loss. The peak of this curve (DTG_{max}) may be expressed as a single thermal decomposition temperature and can be used to compare the thermal stability characteristics of different samples.

UV-Visible spectrophotometry (UV-Vis)

Solution UV-Vis spectra were measured on a UV-Vis spectrophotometer (T70+, PG Instrument). All lignin samples were dissolved in DMSO with concentraion of 0.0625 mg

mL^{-1}. DMSO was set as background and the samples were measured in absorbance mode in the range of 200-700 nm. Solid UV-Vis spectra were analyzed on a UV-Vis spectrophotometer (UV-2600, Shimadzu) in diffuse reflectance mode in the range of 200-900 nm using $BaSO_4$ as background.

B. Experimental part

B.1 Preparation of lignin-carbon composite electrodes

While keeping the total quantity of all components constant at 60 mg, the ratios between lignin as active material, conductive carbon, and PVDF binder were varied. The materials were then mixed by ball milling with 250 µL NMP for 1 h at a frequency of 20 Hz. The ink slurry (10 µL) was applied as a film onto graphite sheet current collectors with a geometric surface area of 1.5 cm^2. The composite films were dried under vacuum at 60 °C for 18 h. The electrode compositions were denoted as $L_{wt\%\ lignin}C_{wt\%\ carbon}B_{wt\%\ binder}$.

B.2 Lignin phosphitylation

In order to determine hydroxyl functional groups in lignin and modified lignin, samples were phosphitylated.[134,214,215] Chemical shift of the samples are referenced to an internal standard (cyclohexanol). Lignin or modified lignins (30 mg) were dried under vacuum at 40 °C overnight and then dissolved in 200 µL DMF. 100 µL 1:1 (v:v) DMF/pyridine solution containing cyclohexanol (11 µmol) and chromium (III) acetylacetonate (1.4 µmol) as a relaxing agent was added. After stirring for 5-10 min, the phosphitylating agent TMDP (100 µL) and $CDCl_3$ (300 µL) were added to the mixture. The samples were recorded by ^{31}P NMR.

B.3 Lignin acetylation

Acetylation is another general technique for the interpretation of the structure of lignin.[97,249,250] Briefly, 3 mL of 1:1 (v/v) mixture of pyridine and acetic anhydride was added to 100 mg of lignin or modified lignin then the mixture was stirred for 48 h at room temperature. The resulting product was precipitated by addition of 20 mL of 1% HCl (at 0 ºC), filtered, washed with deionized water to neutralization, and finally dried under

vacuum at room temperature. Acetylated lignin samples were dissolved in $CDCl_3$ and recorded by ^1H NMR.

B.4 Electrochemical measurement

Electrochemical characterization was performed in a typical three-electrode system at room temperature at a scan rate of 5 mV s^{-1}. Cyclic voltammetry was recorded in various concentrations of $HClO_4$ aqueous solution electrolyte in the potential voltage window from -0.2 V to 0.8 V *vs.* Ag/AgCl KCl^{sat}. Electrochemical impedance spectroscopy (EIS) was conducted in the frequency range of 0.02 Hz to 20 kHz with 10 mV sinusoidal voltage. Galvonostatic charge/discharge was measured at various current densities (0.075-5 A g^{-1}) with the potential windows ((-0.1)-0.8 V) or (0.0-0.9 V).

B.5 Modification of lignin with dialdehyde crosslinking agents (in solution)

1.35 g lignin was dissolved in 12 mL NMP, then 296 µL glyoxal solution (containing 150 mg glyoxal, *i.e.* the same glyoxal:lignin ratio as in the films with 5% glyoxal, 0.82 mol equivalent of total phenolic G and HP groups in lignin, as estimated from ^{31}P NMR) was added. The mixture was heated at different temperatures (60 °C, 80 °C, or 100 °C) for 18 h. To precipitate the modified lignin, $CHCl_3$ was added to the solution and the precipitate was then filtered and dried under vacuum at room temperature overnight. For heat treatment of lignin without glyoxal, the lignin concentration in NMP and the treatment conditions were kept the same as in the procedure above. After 18 h, NMP was removed under high vacuum at room temperature. The product was solidified by addition of some water, then filtered and dried again under vacuum at room temperature.

B.6 Crosslinked lignin composite electrode preparation by crosslinking lignin ***before*** electrode formation

Electrode fabrication was performed in the same manner as B.1 with modification. 30 mg crosslinked lignin (in solution as followed B.6) and 30 mg high surface area carbon were mixed together in 250 µL NMP by mortar mixing. The obtained slurry was applied onto graphite sheet current collectors with a geometric surface area of 1.5 cm^2. Finally, the composite film was dried in a vacuum oven at room temperature for 3 days.

B.7 Crosslinked lignin composite electrode preparation by crosslinking lignin ***during*** electrode formation

The total amount of components was kept at 60 mg in 250 µL NMP, keeping the amount of high surface area carbon fixed at 30 mg (50 wt%). The amount of a dialdehyde crosslinker was varied between 0-10 wt%. Lignin and carbon were mixed together in 250 µL NMP by mortar mixing to obtain homogeneous ink slurry, subsequently a crosslinker was added into the slurry, followed by further mixing. 10 µL slurry was applied onto graphite sheet by drop casting with a geometric surface area of 1.5 cm^2. The composite films were kept at various temperatures (60 °C, 80 °C, or 100 °C) for 18 h in vacuum or were further heated to 80 °C for 2 h.

B.8 Battery testing

A Swagelok-type two-electrode cell was used to test battery performance. A lithium metal disk (thickness: 0.1 mm; diameter: 8 mm) was used as the counter electrode. Lignin carbon composite electrodes (diameter: 10 mm), cut by an EQ-T06-Disc tool (MTI, USA) were used as working electrodes. The electrolyte was 1 M LiTFSI DOL/DME. To prevent a short circuit, a glass fiber separator (Whatman GF/A; diameter: 13 mm) was placed between the lithium anode and the cathode. The cells were assembled in a dry glove box in argon atmosphere (oxygen and water content < 0.1 ppm). Systems were allowed to relax for at least 12 h to stabilize the cells. CV was performed at a scan rate of 0.1 mV s^{-1} in the range of 3.8-1.5 V and galvanostatic discharge was performed at a constant current density of 3.5-1.0 V. The specific capacities were calculated per weight of total mass.

B.9 Oxidation of 4-methyl-2-methoxyphenol (MMP) by Cerium ammonium nitrate (CAN)

MMP was dissolved in 10 mL ACN/water (1:1; v/v) then CAN was added into the solution. After being stirred at room temperature for 30 min, the solution turned to red wine color and was then extracted with $CHCl_3$. The organic phase was collected and evaporated to yield the crude product. The crude product was noted as Ox_MMP, x denoting the equivalents of CAN used with respect to the amount to MMP.

B.10 Oxidation of lignin by Cerium ammonium nitrate (CAN)

Kraft lignin was first dissolved in 10 mL DMF then 10 mL CAN aqueous solution was added. After being stirred at room temperature for 30 min, the mixture turned to red wine color then it was evaporated, washed with water, filtered and dried in vacuum at 40 ºC. The oxidized lignin product was noted as Ox_lignin, x denoting the equivalents of CAN used with respect to the amount to S and G groups existing in lignin (3.25 mmol g^{-1}).

B.11 Quinone content determination by ^{31}P NMR[244]

In order to analyse the quinone content, dried lignin samples (30 mg) was derivatized with 250 µL trimethylphosphite and 250 µL anhydrous DMF under an argon atmosphere at room temperature for 2 days. Then excess trimethylphosphite was removed under vacuum at 40°C for 3 hours. The treated lignins were dissolved in 450 µL of solvent consisting of 60% DMSO-d_6/pyridine (v/v) containing tri-*m*-tolylphosphate (0.7 mg/mL) and chromium (III) acetylacetonate (0.9 mg/mL). 5 µL water (0.3 mmol per 30 mg lignin) was added and analysis was carried out by ^{31}P NMR. The internal standard, tri-*m*-tolylphosphate (δ -16.3 ppm), was used both for quantification and as a shift reference.

C. Supplementary information

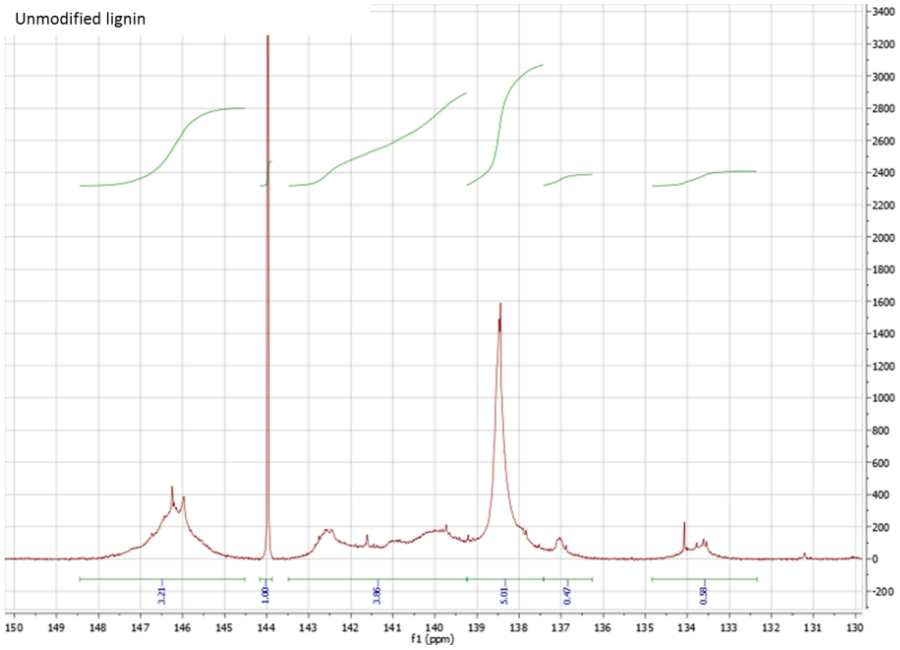

Figure C-1 ^{31}P NMR spectra of unmodified lignin in DMSO-d_6 solvent after phosphorylation (cyclohexanol as an internal standard,144.5 ppm).

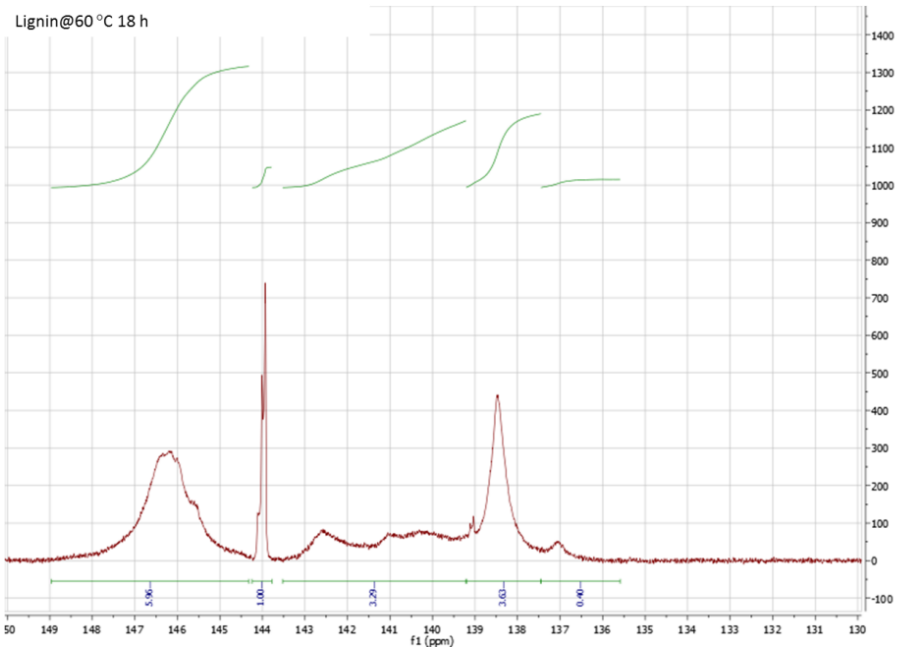

Figure C-2 ^{31}P NMR spectrum of heat-treated lignin at 60 °C 18 h in DMSO-d_6 solvent after phosphorylation (cyclohexanol as an internal standard,144.5 ppm).

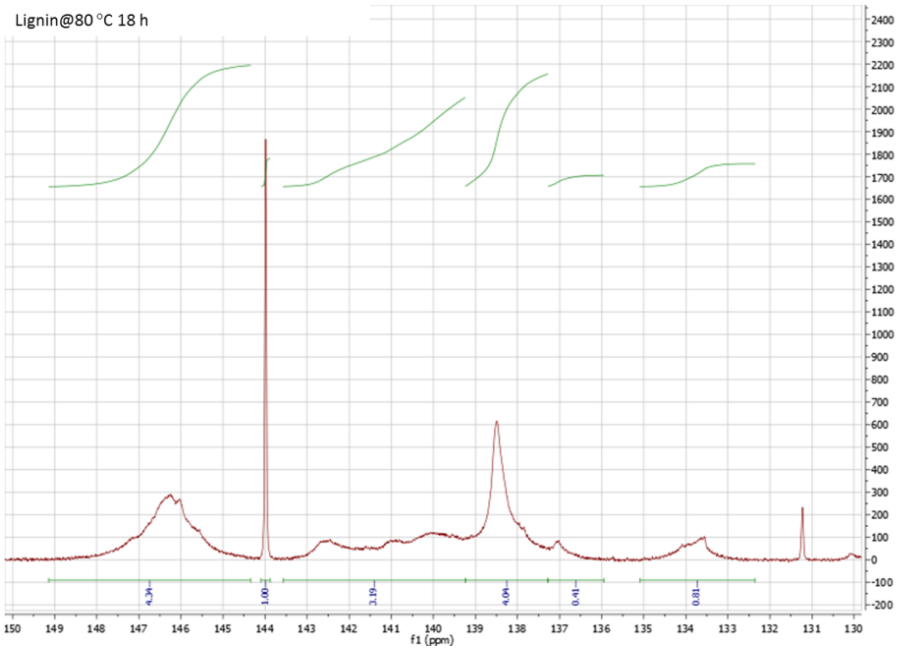

Figure C-3 ^{31}P NMR spectrum of heat-treated lignin at 80 °C 18 h in DMSO-d_6 solvent after phosphorylation (cyclohexanol as an internal standard,144.5 ppm).

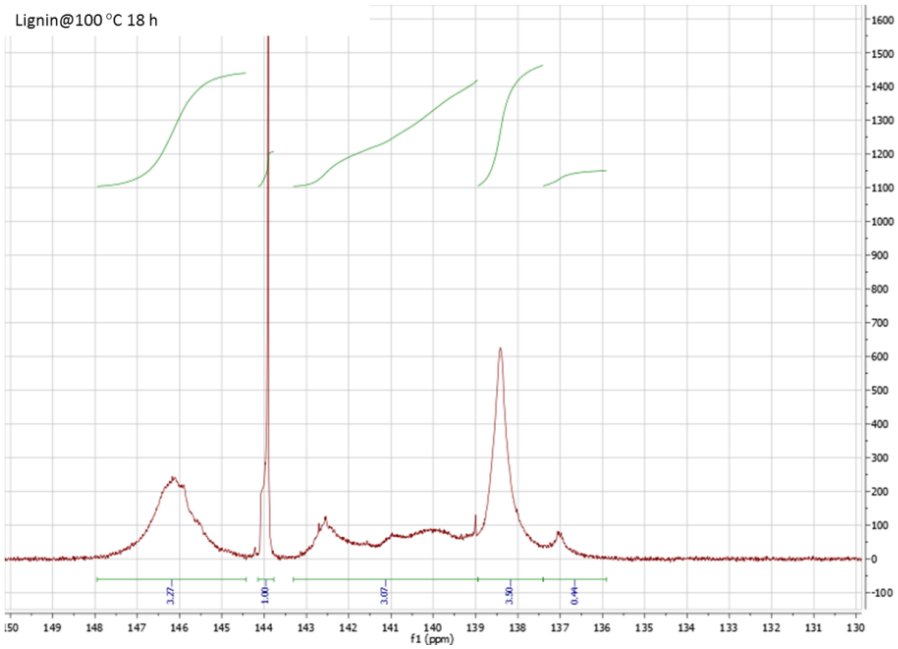

Figure C-4 ^{31}P NMR spectrum of heat-treated lignin at 100 °C 18 h in DMSO-d_6 solvent after phosphorylation (cyclohexanol as an internal standard,144.5 ppm).

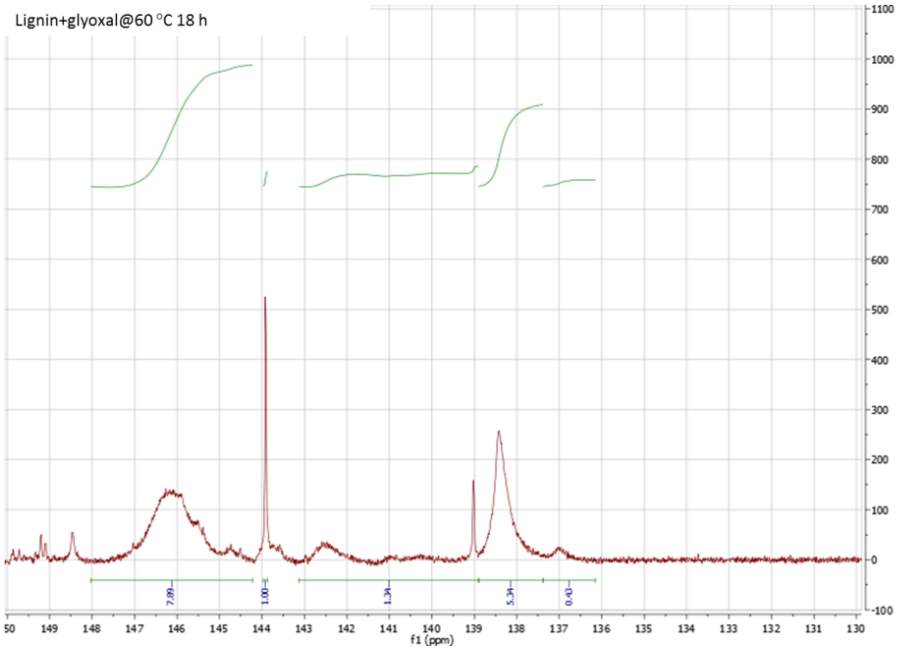

Figure C-5 ^{31}P NMR spectrum of heat-treated lignin with glyoxal at 60 °C 18 h in DMSO-d_6 solvent after phosphorylation (cyclohexanol as an internal standard,144.5 ppm).

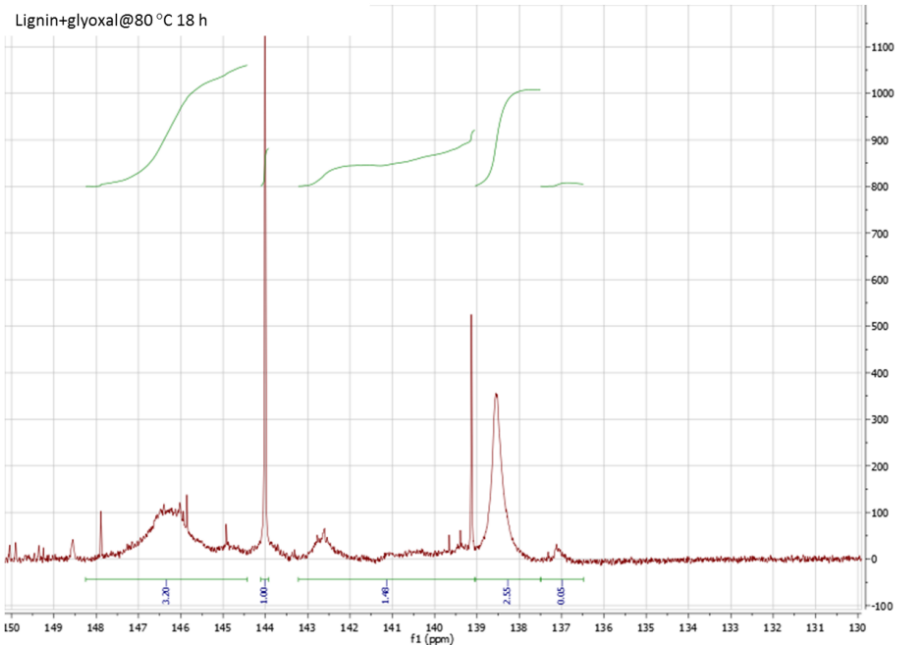

Figure C-6 ^{31}P NMR spectrum of heat-treated lignin with glyoxal at 80 °C 18 h in DMSO-d_6 solvent after phosphorylation (cyclohexanol as an internal standard,144.5 ppm).

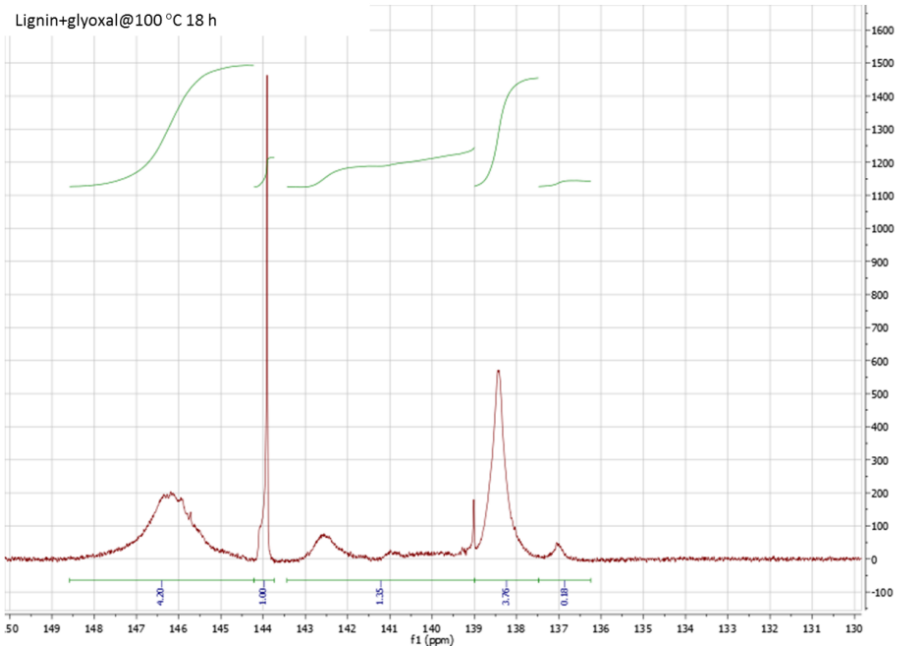

Figure C-7 ^{31}P NMR spectrum of heat-treated lignin with glyoxal at 100 °C 18 h in DMSO-d_6 solvent after phosphorylation (cyclohexanol as an internal standard,144.5 ppm).

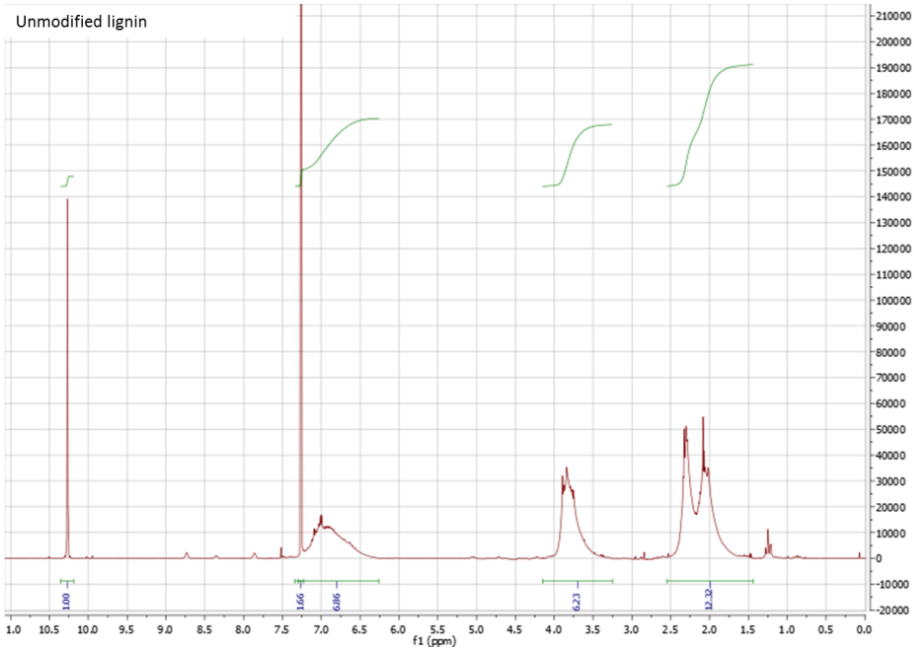

Figure C-8 ^{1}H NMR spectrum of Kraft lignin in $CDCl_3$ solvent after acetylation (2,3,4,5,6-pentafluorobenzaldehydeas as an internal standard, 10.26 ppm).

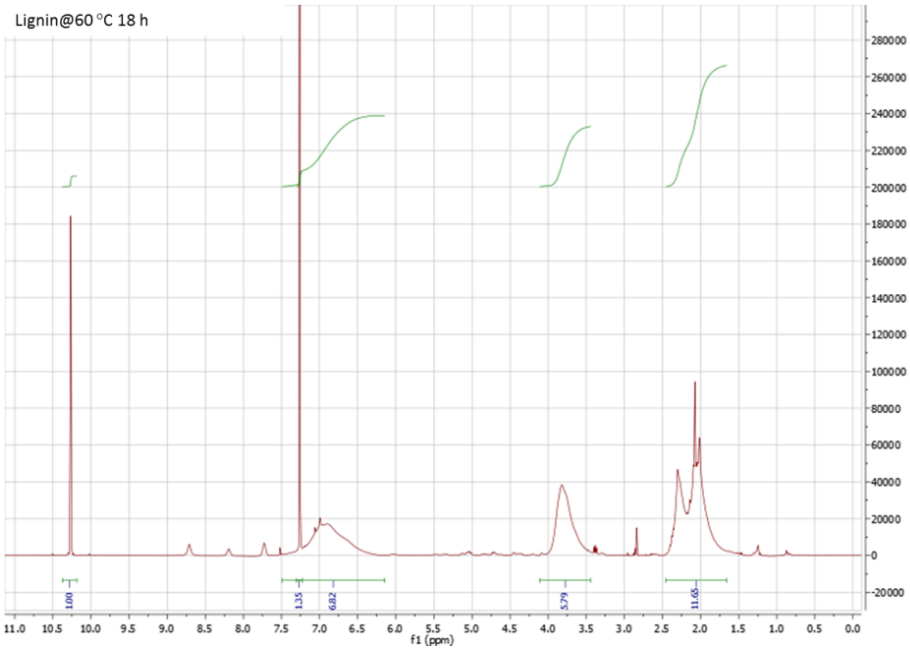

Figure C-9 ^{1}H NMR spectrum of heat-treated lignin at 60 °C 18 h in $CDCl_3$ solvent after acetylation (2,3,4,5,6-pentafluorobenzaldehydeas as an internal standard, 10.26 ppm).

Figure C-10 ^{1}H NMR spectrum of heat-treated lignin at 80 °C 18 h in $CDCl_3$ solvent after acetylation (2,3,4,5,6-pentafluorobenzaldehydeas as an internal standard, 10.26 ppm).

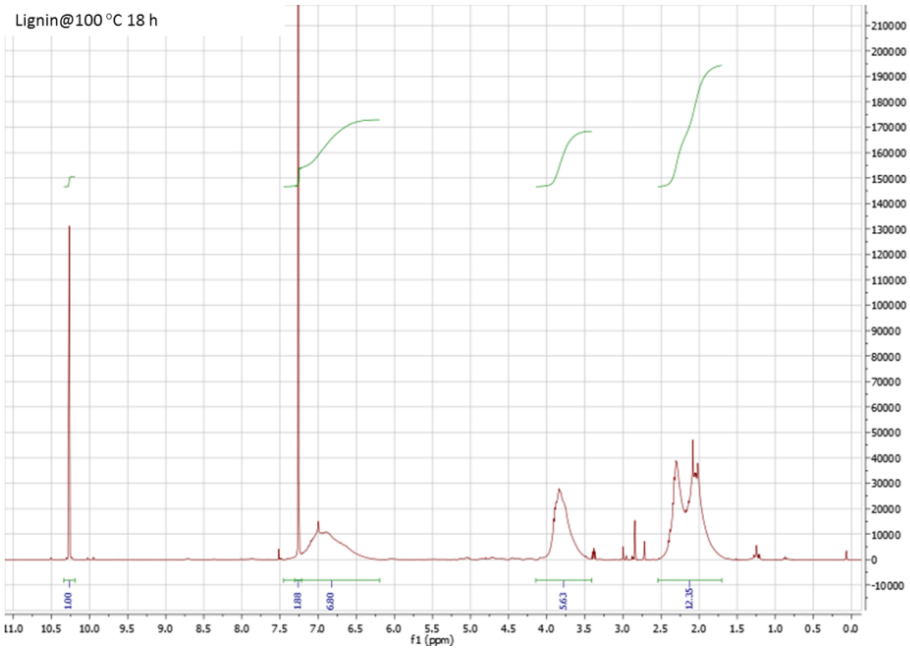

Figure C-11 ^{1}H NMR spectrum of heat-treated lignin at 100 °C 18 h in $CDCl_3$ solvent after acetylation (2,3,4,5,6-pentafluorobenzaldehydeas as an internal standard, 10.26 ppm).

Figure C-12 ^{1}H NMR spectrum of heat-treated lignin at 60 °C 18 h in the presence of glyoxal in $CDCl_3$ solvent after acetylation (2,3,4,5,6-pentafluorobenzaldehydeas as an internal standard, 10.26 ppm).

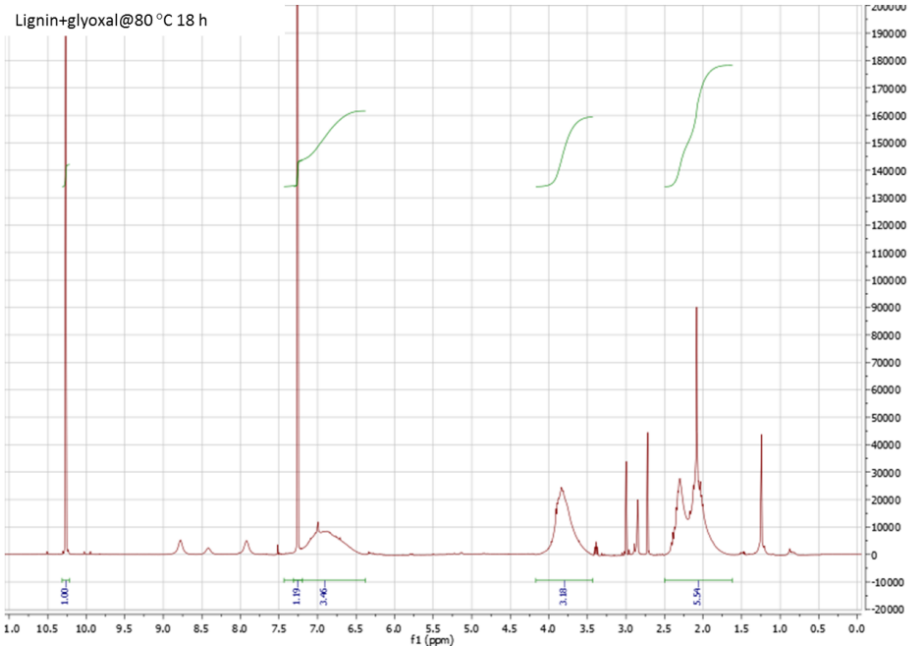

Figure C-13 ^{1}H NMR spectrum of heat-treated lignin at 80 °C 18 h in the presence of glyoxal in $CDCl_3$ solvent after acetylation (2,3,4,5,6-pentafluorobenzaldehydeas as an internal standard, 10.26 ppm).

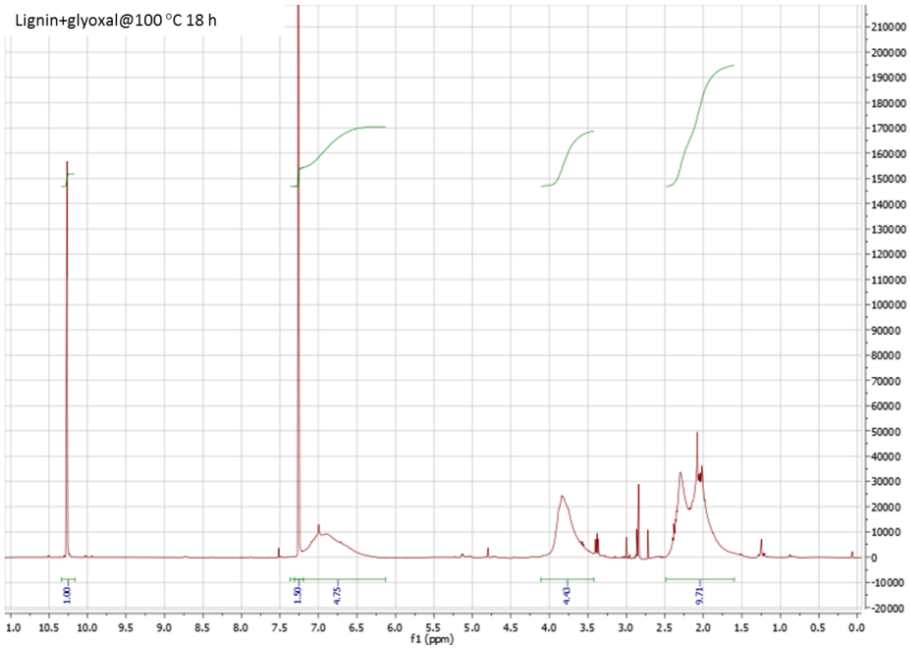

Figure C-14 ^{1}H NMR spectrum of heat-treated lignin at 100 °C 18 h in the presence of glyoxal in $CDCl_3$ solvent after acetylation (2,3,4,5,6-pentafluorobenzaldehydeas as an internal standard, 10.26 ppm).

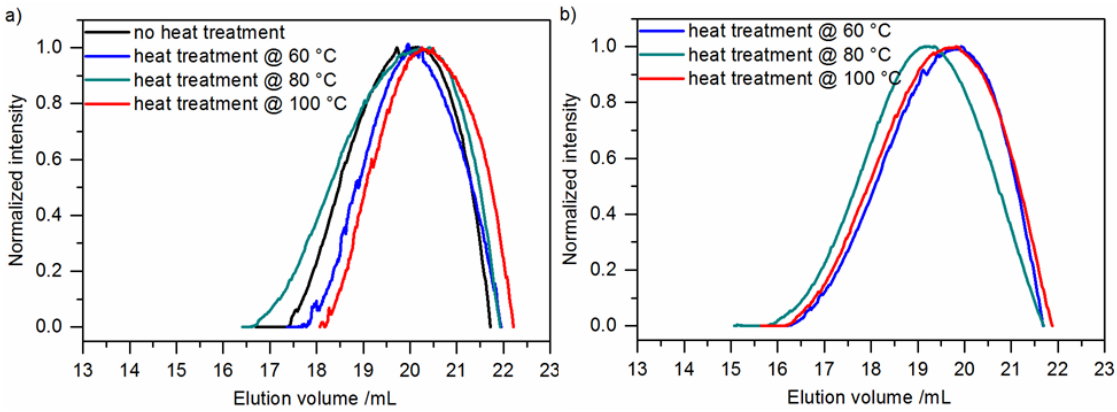

Figure C-15 GPC traces in NMP of samples that were heat treated at different temperature as indicated. a) Neat lignin; b) lignin in the presence of glyoxal.

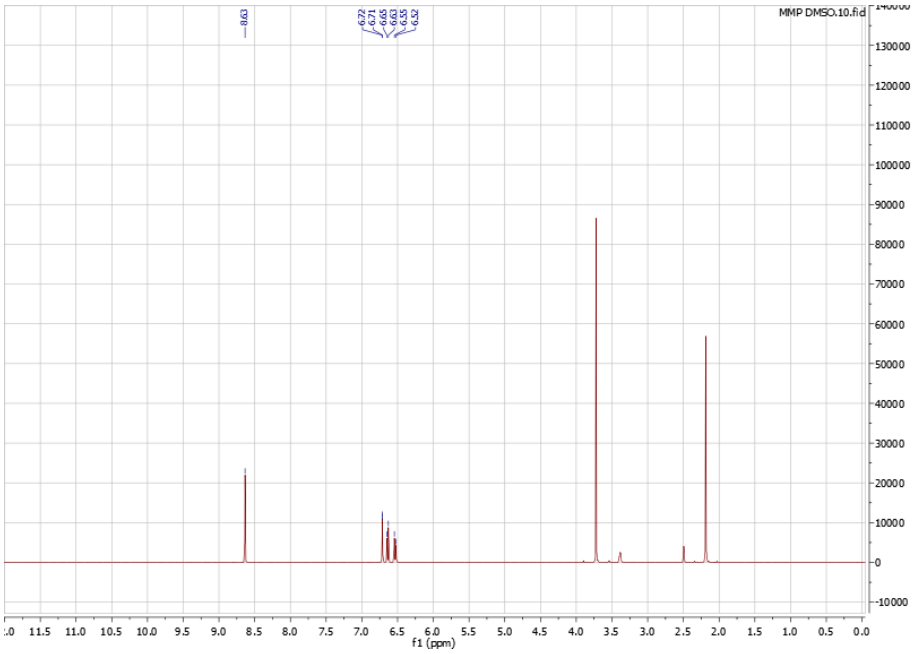

Figure C-16 ^{1}H NMR spectrum of MMP in DMSO-*d6* solvent.

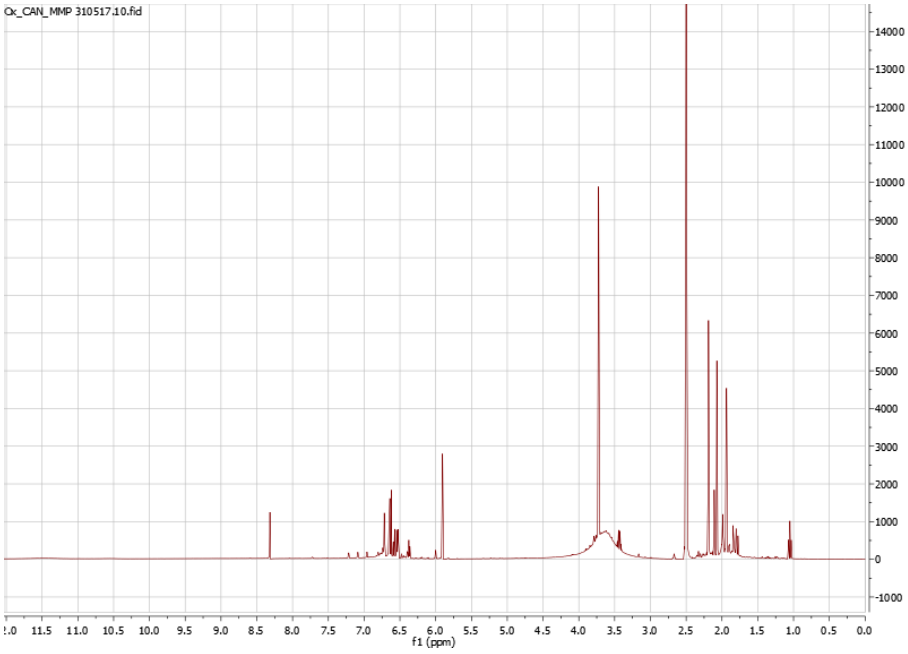

Figure C-17 ^{1}H NMR spectrum of crude product of Ox_MMP (3.0 eq CAN) in DMSO-*d6* solvent.

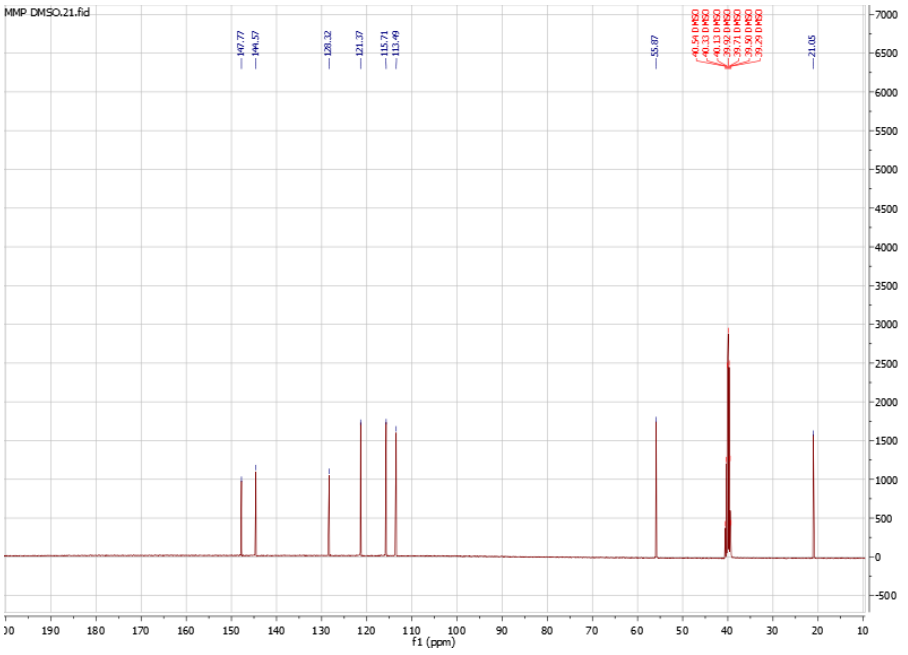

Figure C-18 ^{13}C NMR spectrum of MMP in DMSO-*d6* solvent.

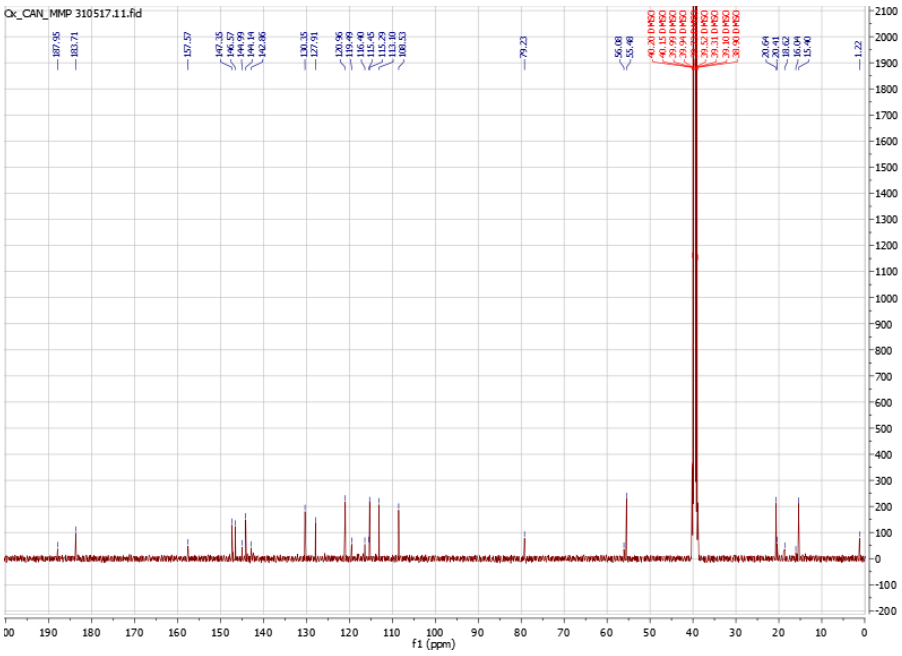

Figure C-19 ^{13}C NMR spectrum of crude product of Ox_MMP (3 eq CAN) in DMSO-*d6* solvent.

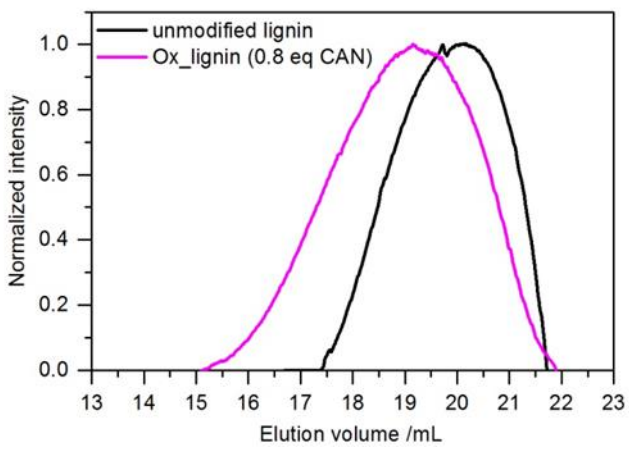

Figure C-20 GPC traces in NMP of samples of unmodified lignin and Ox_lignin (0.8 eq CAN).

D. List of abbreviations

1,3-dioxolane	DOL
2-chloro-4,4,5,5-tetramethyl-1,3,2-dioxaphospholane	TMDP
5-hydroxymethyl-2-furfuraldehde	FA
Aliphatic hydroxy	Ali-OH
Ampere per gram	A g^{-1}
Ampere-hours per gram	Ah g^{-1}
An Energy Dispersive X-Ray Analyser	EDX
Attenuated total reflection	ATR
Binder	B
Carbon	C
Cerium ammonium nitrate	CAN
Counter electrode	CE
Current	I
Cyclic voltammogram	CV
Derivative thermogravimetry	DTG
Diethyl carbonate	DEC
Dimethyl formamide	DMF
Dimethyloxyethane	DME
Dispersity	Đ
Electrical Double layer	EDL
Electrochemical impedance spectroscopy	EIS
Electrospray ionization-mass spectrometry	ESI-MS
Equation	eqn
Equivalent	eq
Equivalent series resistance	ERS
Ethylene carbonate	EC
Fourier transform-infrared spectroscopy	FT-IR
Gel permeation chromatography	GPC
Glutaraldehyde	GA
Guaiacyl	G
Lignin	L
Lithium bis(trifluoromethanesulfonyl)imide	LiTFSI
Lithium hexafluorophosphate	$LiPF_6$
Lithium-ion batteries	LIBs
mass to charge	m/z
Molar	M
N-Methyl-2-pyrrolidone	NMP
Nuclear magnetic resonance	NMR
Number average molecular weight	M_n
Perchloric acid	$HClO_4$
Phenol-formaldehyde	PF
Phenolic hydroxy	Ph-OH

p-hydroxylphenol	HP
Platinum	Pt
Polystyrene	PS
Polyvinylidene fluoride	PVDF
Potassium chlorode	KCl
Reference electrode	RE
Room temperature	RT
Scanning electron microscope	SEM
Silver nitrate	$AgNO_3$
Size exclusion chromatography	SEC
Syringyl	S
Terephthaldehyde	TA
Tetrahydrofuran	THF
Theoretical capacity	C_{theor}
Thermogravimetric Analysis	TGA
Thiophene-2,5-dicarboxaldehyde	ThA
Total hydroxy	Total-OH
Trimethylphosphite	TMP
UV-Visible spectrophotometry	UV-Vis
Volt	V
Weight average molecular weight	M_w
Working electrode	WE

E. List of publications

Publications:

Chaleawlert-umpon, S., Berthold, T., Wang, X., Antonietti, M., Liedel, C*. "Kraft Lignin as Electrode Material for Sustainable Electrochemical Energy Storage" Advanced Materials Interfaces **2017**, *4(23)*, 1700698.

Chaleawlert-umpon, S. and Liedel, C*. "More sustainable energy storage: lignin based electrodes with glyoxal crosslinking" Journal of Materials Chemistry A **2017**, *5*, 24344-24352.

Participated conference:

Saowaluk Chaleawlert-umpon, Thomas Berthold, Xuewan Wang, Markus Antonietti, and Clemens Liedel* "Investigating Electrochemical Behavior of Kraft Lignin for Sustainable Electrode Material" The Organic Battery Days 2017, Uppsala, Sweden, 8-9 June 2017, Poster.

F. Acknowledgements

I would like to express my deep gratitude to many people who have come along with me and have given me guidance and help during the time spent on my PhD.

First of all, I would like to express much thanks to Prof. Dr. Markus Antonietti who provided me the opportunity to do my PhD research at MPIKG, and Dr. Clemens Liedel, my supervisor, for all his guidance, discussion, encouragement, and pushing me through my research time. My thanks go to all the fruitful suggestions and discussions from Prof. Dr. Helmut Schlaad, Dr. Kerry Gilmore, Dr. Xuewan Wang, Thomas Berthold, Dr. Siebel Özenler, Dr. Valerio Molinari, Dr. Bernhard Schmidt, and Dr. Martin Oschatz. I would like to thanks Dr. Nina Fechler for the provision of conductive carbons and Dr. Davide Esposito for Kraft lignin.

Furthermore, I would like to thank my colleagues in the sustainable energy storage materials group: Jessica Brandt and Steffen Tröger-Müller for all your supports, friendship and kindliness. You both created an amazing atmosphere in the lab. I would like to thank my lunch mate, Lina Li, who'd always keep chatting with me about all the news, events, and gossips. Special thanks to the technicians for the measurements of my samples, useful suggestions, and some chemicals Antje Völkel, Rona Pitschke, Heike Runge, Ursula Lubahn, Marlies Gräwert, Sylvia Pirok, Olaf Niemeyer, Jessica Brandt, Katharina Otte, Regina Rothe, and Irena Shekova.

I would like to thank MPIKG for the financial support to do the research and contribute in a conference, the Royal Thai Government for providing me a scholarship, and the great opportunity for further study from my work places: National Science and Technology Development Agency and National Nanotechnology Center, Thailand. Moreover, thanks to all the staffs in the Office of Educational Affairs, Germany who took care of everything for all the Thai students in Germany. I would like to express my gratitude to all my friends in Thailand and for their help and for being good listeners, as well as for the encouragement and suggestions about the PhD student's life from Rawiwan, Kornpimol, Dr. Onanong, and Dr. Nuttawan.

Finally, I am very grateful for my mother's patience and sacrifice, waiting for me alone at our home in Thailand. She is the great driving force that keeps me going, that keeps me patient.

G. Declaration

The present work was carried out during the period from August 2015 to January 2018 at the Max Planck Institute of Colloids and Interfaces under supervision of Prof. Dr. Markus Antonietti.

I hereby declare that I have prepared the present work independently and have not used any other means or sources other than those specified.

Saowaluk Chaleawlert-umpon

Potsdam, den 08.01.2018

H. References

(1) Larcher, D.; Tarascon, J. M. *Nature Chemistry* **2015**, *7*, 19-29.
(2) BP Statistical Review of World Energy 2017 (2017). Available from: http://www.bp.com/en/global/corporate/energy-economics/statistical-review-of-world-energy/downloads.html. Accessed (2017, August 12).
(3) Conti, J. International Energy Outlook 2016 (2016). Available from: http://www.eia.gov/forecasts/ieo. Accessed (2017, August 12).
(4) Schon, T. B.; McAllister, B. T.; Li, P.-F.; Seferos, D. S. *Chemical Society Reviews* **2016**, *45*, 6345-6404.
(5) Milczarek, G.; Nowicki, M. *Materials Research Bulletin* **2013**, *48*, 4032-4038.
(6) Kim, S. K.; Kim, Y. K.; Lee, H.; Lee, S. B.; Park, H. S. *Journal of Chemistry and Sustainability, Energy and Materials* **2014**, *7*, 1094-1101.
(7) Armaroli, N.; Balzani, V. *Energy & Environmental Science* **2011**, *4*, 3193-3222.
(8) Chen, H.; Cong, T. N.; Yang, W.; Tan, C.; Li, Y.; Ding, Y. *Progress in Natural Science* **2009**, *19*, 291-312.
(9) Cho, J.; Jeong, S.; Kim, Y. *Progress in Energy and Combustion Science* **2015**, *48*, 84-101.
(10) Luo, X.; Wang, J.; Dooner, M.; Clarke, J. *Applied Energy* **2015**, *137*, 511-536.
(11) Yekini Suberu, M.; Wazir Mustafa, M.; Bashir, N. *Renewable and Sustainable Energy Reviews* **2014**, *35*, 499-514.
(12) Renewables Informations Overview (2017). Available from: https://www.iea.org/publications/freepublications/publication/renewables-information---2017-edition---overview.html. Accessed (2017, August 12).
(13) Electrical Energy Storage (2010). Available from: http://www.iec.ch/whitepaper/energystorage/?ref=extfooter. Accessed (2017, August 12).
(14) Conway, B. E. *Electrochemical Supercapacitors Scientific Fundamentals and Technological Applications*; Springer Science Business Media: New York, 1999.
(15) Brousse, T.; Belanger, D.; Long, J. W. *Journal of The Electrochemical Society* **2015**, *162*, A5185-A5189.
(16) Lukatskaya, M. R.; Dunn, B.; Gogotsi, Y. *Nature Communications* **2016**, *7*, 12647.
(17) Wang, Y.; Song, Y.; Xia, Y. *Chemical Society Reviews* **2016**, *45*, 5925-5950.
(18) Electric vehicle overview. Available from: http://energyskeptic.com/2015/electric-vehicle-overview. Accessed (2017, August 12).
(19) Simon, P.; Gogotsi, Y. *Nature Materials* **2008**, *7*, 845-854.
(20) Liu, R.; Duay, J.; Lee, S. B. *Chemical Communications* **2011**, *47*, 1384-1404.
(21) Chen, W.; Fan, Z.; Gu, L.; Bao, X.; Wang, C. *Chemical Communications* **2010**, *46*, 3905-3907.
(22) Huang, X.; Qi, X.; Boey, F.; Zhang, H. *Chemical Society Reviews* **2012**, *41*, 666-686.
(23) Rudge, A.; Davey, J.; Raistrick, I.; Gottesfeld, S.; Ferraris, J. P. *Journal of Power Sources* **1994**, *47*, 89-107.
(24) Miret, S. Storage wars: Batteries vs. supercapacitors. Available from: http://berc.berkeley.edu/storage-wars-batteries-vs-supercapacitors. Accessed (2017, August 12).
(25) Winter, M.; Brodd, R. J. *Chemical Reviews* **2004**, *104*, 4245-4270.
(26) Kumar, R. V.; Sarakonsri, T. *Introduction to Electrochemical Cells*; Wiley-VCH Verlag GmbH & Co. KGaA, Weinheim, Germany, 2010.
(27) Zu, C.-X.; Li, H. *Energy & Environmental Science* **2011**, *4*, 2614-2624.
(28) Cheng, F.; Liang, J.; Tao, Z.; Chen, J. *Advanced Materials* **2011**, *23*, 1695-1715.
(29) Lithium Batteries. Available from: https://www.doitpoms.ac.uk/tlplib/batteries/batteries_lithium.php. Accessed (2017, August 12).
(30) Muench, S.; Wild, A.; Friebe, C.; Häupler, B.; Janoschka, T.; Schubert, U. S. *Chemical Reviews* **2016**, *116*, 9438-9484.
(31) Thackeray, M. M.; Wolverton, C.; Isaacs, E. D. *Energy & Environmental Science* **2012**, *5*, 7854-7863.
(32) Xianxia Yuan; Hansan Liu; Zhang, J. *Lithium-ion batteries: advanced materials and technologies*; Boca Raton, FL : CRC Press, 2012.
(33) Goward, G. R.; Taylor, N. J.; Souza, D. C. S.; Nazar, L. F. *Journal of Alloys and Compounds* **2001**, *329*, 82-91.
(34) Rao, B. M. I.; Francis, R. W.; A.H., C. *Journal of The Electrochemical Society* **1977**, *124*, 1490-1492.
(35) Whittingham, M. S. *Chemical Reviews* **2004**, *104*, 4271-4302.
(36) Di Lecce, D.; Verrelli, R.; Hassoun, J. *Green Chemistry* **2017**, *19*, 3442-3467.

(37) Qie, L.; Manthiram, A. *ACS Energy Letters* **2016**, *1*, 46-51.
(38) Pang, Q.; Tang, J.; Huang, H.; Liang, X.; Hart, C.; Tam, K. C.; Nazar, L. F. *Advanced Materials* **2015**, *27*, 6021-6028.
(39) Liang, X.; Garsuch, A.; Nazar, L. F. *Angewandte Chemie International Edition* **2015**, *54*, 3907-3911.
(40) Yang, Y.; Zheng, G.; Cui, Y. *Chemical Society Reviews* **2013**, *42*, 3018-3032.
(41) Kraytsberg, A.; Ein-Eli, Y. *Journal of Power Sources* **2011**, *196*, 886-893.
(42) Armand, M.; Tarascon, J. M. *Nature* **2008**, *451*, 652-657.
(43) Poizot, P.; Dolhem, F. *Energy & Environmental Science* **2011**, *4*, 2003-2019.
(44) Williams, D. L.; Byrne, J. J.; Driscoll, J. S. *Journal of The Electrochemical Society* **1969**, *116*, 2-4.
(45) Alt, H.; Binder, H.; Köhling, A.; Sandstede, G. *Electrochimica Acta* **1972**, *17*, 873-887.
(46) Ohzuku, T.; Wakamatsu, H.; Takehara, Z.; Yoshizawa, S. *Electrochimica Acta* **1979**, *24*, 723-726.
(47) Yamaki, J. i.; Yamaji, A. *Journal of The Electrochemical Society* **1982**, *129*, 5-9.
(48) Novák, P.; Müller, K.; Santhanam, K. S. V.; Haas, O. *Chemical Reviews* **1997**, *97*, 207-282.
(49) Nigrey, P. J.; MacInnes, D.; Nairns, D. P.; MacDiarmid, A. G.; Heeger, A. J. *Journal of The Electrochemical Society* **1981**, *128*, 1651-1654.
(50) Häupler, B.; Wild, A.; Schubert, U. S. *Advanced Energy Materials* **2015**, *5*, 1402034-1402067.
(51) Liang, Y.; Tao, Z.; Chen, J. *Advanced Energy Materials* **2012**, *2*, 742-769.
(52) Song, Z.; Zhou, H. *Energy & Environmental Science* **2013**, *6*, 2280-2301.
(53) Song, Z.; Qian, Y.; Gordin, M. L.; Tang, D.; Xu, T.; Otani, M.; Zhan, H.; Zhou, H.; Wang, D. *Angewandte Chemie International Edition* **2015**, *54*, 13947-13951.
(54) Song, Z.; Zhan, H.; Zhou, Y. *Chemical Communications* **2009**, 448-450.
(55) Yang, Y.; He, K.; Yan, P.; Wang, D.; Wu, X.; Zhao, X.; Huang, Z.; Zhang, C.; He, D. *Electrochimica Acta* **2014**, *138*, 481-485.
(56) Zhao, L.; Wang, W.; Wang, A.; Yuan, K.; Chen, S.; Yang, Y. *Journal of Power Sources* **2013**, *233*, 23-27.
(57) Chen, W.-M.; Qie, L.; Yuan, L.-X.; Xia, S.-A.; Hu, X.-L.; Zhang, W.-X.; Huang, Y.-H. *Electrochimica Acta* **2011**, *56*, 2689-2695.
(58) Qiu, L.; Zhang, S.; Zhang, L.; Sun, M.; Wang, W. *Electrochimica Acta* **2010**, *55*, 4632-4636.
(59) Cai, Y.-m.; Qin, Z.-y.; Chen, L. *Progress in Natural Science: Materials International* **2011**, *21*, 460-466.
(60) Nakahara, K.; Iwasa, S.; Satoh, M.; Morioka, Y.; Iriyama, J.; Suguro, M.; Hasegawa, E. *Chemical Physics Letters* **2002**, *359*, 351-354.
(61) Sterby, M.; Emanuelsson, R.; Huang, X.; Gogoll, A.; Strømme, M.; Sjödin, M. *Electrochimica Acta* **2017**, *235*, 356-364.
(62) Zhang, M. *Journal of Alloys and Compounds* **2017**, *723*, 139-145.
(63) Oyama, N.; Tatsuma, T.; Sotomura, T. *Journal of Power Sources* **1997**, *68*, 135-138.
(64) Gracia, R.; Mecerreyes, D. *Polymer Chemistry* **2013**, *4*, 2206-2214.
(65) Xie, J.; Zhang, Q. *Journal of Materials Chemistry A* **2016**, *4*, 7091-7106.
(66) Nishide, H.; Koshika, K.; Oyaizu, K. *Pure and Applied Chemistry* **2009**, *81*, 1961-1970.
(67) Yokoji, T.; Matsubara, H.; Satoh, M. *Journal of Materials Chemistry A* **2014**, *2*, 19347-19354.
(68) Yao, M.; Senoh, H.; Yamazaki, S.-i.; Siroma, Z.; Sakai, T.; Yasuda, K. *Journal of Power Sources* **2010**, *195*, 8336-8340.
(69) Yao, M.; Yamazaki, S.-i.; Senoh, H.; Sakai, T.; Kiyobayashi, T. *Materials Science and Engineering: B* **2012**, *177*, 483-487.
(70) Arcila-Velez, M. R.; Roberts, M. E. *Chemistry of Materials* **2014**, *26*, 1601-1607.
(71) Oyama, N.; Sarukawa, T.; Mochizuki, Y.; Shimomura, T.; Yamaguchi, S. *Journal of Power Sources* **2009**, *189*, 230-239.
(72) Jaffe, A.; Saldivar Valdes, A.; Karunadasa, H. I. *Chemistry of Materials* **2015**, *27*, 3568-3571.
(73) Zeng, R.; Xing, L.; Qiu, Y.; Wang, Y.; Huang, W.; Li, W.; Yang, S. *Electrochimica Acta* **2014**, *146*, 447-454.
(74) Song, Z.; Xu, T.; Gordin, M. L.; Jiang, Y.-B.; Bae, I.-T.; Xiao, Q.; Zhan, H.; Liu, J.; Wang, D. *Nano Letters* **2012**, *12*, 2205-2211.
(75) Xiang, J.; Chang, C.; Li, M.; Wu, S.; Yuan, L.; Sun, J. *Crystal Growth & Design* **2008**, *8*, 280-282.
(76) Song, Z.; Qian, Y.; Liu, X.; Zhang, T.; Zhu, Y.; Yu, H.; Otani, M.; Zhou, H. *Energy & Environmental Science* **2014**, *7*, 4077-4086.
(77) Zhao, Q.; Guo, C.; Lu, Y.; Liu, L.; Liang, J.; Chen, J. *Industrial & Engineering Chemistry Research* **2016**, *55*, 5795-5804.
(78) Zou, Q.; Wang, W.; Wang, A.; Yu, Z.; Yuan, K. *Materials Letters* **2014**, *117*, 290-293.

(79) Zeng, R.-h.; Li, X.-p.; Qiu, Y.-c.; Li, W.-s.; Yi, J.; Lu, D.-s.; Tan, C.-l.; Xu, M.-q. *Electrochemistry Communications* **2010**, *12*, 1253-1256.
(80) Xu, L.; Yang, F.; Su, C.; Ji, L.; Zhang, C. *Electrochimica Acta* **2014**, *130*, 148-155.
(81) Thakur, V. K.; Thakur, M. K.; Raghavan, P.; Kessler, M. R. *ACS Sustainable Chemistry & Engineering* **2014**, *2*, 1072-1092.
(82) Upton, B. M.; Kasko, A. M. *Chemical Reviews* **2016**, *116*, 2275-2306.
(83) Zakzeski, J.; Bruijnincx, P. C. A.; Jongerius, A. L.; Weckhuysen, B. M. *Chemical Reviews* **2010**, *110*, 3552-3599.
(84) Kai, D.; Tan, M. J.; Chee, P. L.; Chua, Y. K.; Yap, Y. L.; Loh, X. J. *Green Chemistry* **2016**, *18*, 1175-1200.
(85) Liu, W.-J.; Jiang, H.; Yu, H.-Q. *Green Chemistry* **2015**, *17*, 4888-4907.
(86) Ratnaweera, D. R.; Saha, D.; Pingali, S. V.; Labbé, N.; Naskar, A. K.; Dadmun, M. *RSC Advances* **2015**, *5*, 67258-67266.
(87) Chung, H.; Washburn, N. R. *Green Materials* **2013**, *1*, 137-160.
(88) Chakar, F. S.; Ragauskas, A. J. *Industrial Crops and Products* **2004**, *20*, 131-141.
(89) Nitz, H.; Semke, H.; Mülhaupt, R. *Macromolecular Materials and Engineering* **2001**, *286*, 737-743.
(90) Francisco G. Calvo-Flores; Jose A. Dobade; Joaquin Isac-Garcia In *Wood Modification-Chemical, Thermal and other Processes*; Stevens, C., Ed.; John Wiley & Sons, Ltd.: 2015, p 9-48.
(91) Gellerstedt, G. *Industrial Crops and Products* **2015**, *77*, 845-854.
(92) Matsushita, Y. *Journal of Wood Science* **2015**, *61*, 230-250.
(93) Gierer, J. *Wood Science and Technology* **1985**, *19*, 289-312.
(94) Gratzl, J. S.; Chen, C.-L. In *Lignin: Historical, Biological, and Materials Perspectives*; American Chemical Society: 1999; Vol. 742, p 392-421.
(95) Esposito, D.; Antonietti, M. *Chemical Society Reviews* **2015**, *44*, 5821-5835.
(96) Laurichesse, S.; Avérous, L. *Progress in Polymer Science* **2014**, *39*, 1266-1290.
(97) Vishtal, A. G.; Kraslawski, A. *Bioresource Technology* **2011**, *6*, 3547-3568.
(98) Bhat, A. H.; Dasan, Y. K.; Khan, I. In *Agricultural Biomass Based Potential Materials*; Hakeem, K. R., Jawaid, M., Y. Alothman, O., Eds.; Springer International Publishing: Cham, 2015, p 155-179.
(99) Obydenkova, S. V.; Kouris, P. D.; Hensen, E. J. M.; Heeres, H. J.; Boot, M. D. *Bioresource Technology* **2017**, *243*, 589-599.
(100) Ragauskas, A. J.; Beckham, G. T.; Biddy, M. J.; Chandra, R.; Chen, F.; Davis, M. F.; Davison, B. H.; Dixon, R. A.; Gilna, P.; Keller, M.; Langan, P.; Naskar, A. K.; Saddler, J. N.; Tschaplinski, T. J.; Tuskan, G. A.; Wyman, C. E. *Science* **2014**, *344*, 1246843.
(101) George L. Catignani; Carter, M. E. *Journal of Food Science* **1982**, *47*, 1745-1748.
(102) Pouteau, C.; Dole, P.; Cathala, B.; Averous, L.; Boquillon, N. *Polymer Degradation and Stability* **2003**, *81*, 9-18.
(103) García, M. C.; Díez, J. A.; Vallejo, A.; García, L.; Cartagena, M. C. *Industrial & Engineering Chemistry Research* **1996**, *35*, 245-249.
(104) Cotterill, J. V.; Wilkins, R. M. *Journal of Agricultural and Food Chemistry* **1996**, *44*, 2908-2912.
(105) Li, Z.; Xiao, D.; Ge, Y.; Koehler, S. *ACS Applied Materials & Interfaces* **2015**, *7*, 15000-15009.
(106) Pérez, N. A.; Rincón, G.; Delgado, L. A.; González, N. *Adsorption* **2006**, *12*, 279-286.
(107) E. Gonzalez-Serrano; T. Cordero; J. Rodrı´guez-Mirasol; Rodrı´guez, J. J. *Industrial & Engineering Chemistry Research* **1997**, *36*, 4832-4838.
(108) Ge, Y.; Song, Q.; Li, Z. *Journal of Industrial and Engineering Chemistry* **2015**, *23*, 228-234.
(109) Ayyachamy, M.; Cliffe, F. E.; Coyne, J. M.; Collier, J.; Tuohy, M. G. *Biomass Conversion and Biorefinery* **2013**, *3*, 255-269.
(110) Lange, H.; Decina, S.; Crestini, C. *European Polymer Journal* **2013**, *49*, 1151-1173.
(111) Barzegari, M. R.; Alemdar, A.; Zhang, Y.; Rodrigue, D. *Polymer Composites* **2012**, *33*, 353-361.
(112) Kubo, S.; Kadla, J. F. *Journal of Polymers and the Environment* **2005**, *13*, 97-105.
(113) Bozsódi, B.; Romhányi, V.; Pataki, P.; Kun, D.; Renner, K.; Pukánszky, B. *Materials & Design* **2016**, *103*, 32-39.
(114) Mainka, H.; Täger, O.; Körner, E.; Hilfert, L.; Busse, S.; Edelmann, F. T.; Herrmann, A. S. *Journal of Materials Research and Technology* **2015**, *4*, 283-296.
(115) Gogoi, S. B. *Indian Chemical Engineer* **2010**, *52*, 325-335.
(116) El Mansouri, N.-e.; Pizzi, A.; Salvadó, J. *Holz als Roh- und Werkstoff* **2007**, *65*, 65-70.
(117) Yang, S.; Zhang, Y.; Yuan, T. Q.; Sun, R. C. *Journal of Applied Polymer Science* **2015**, *132*, 42493-42500.
(118) Ferdosian, F.; Pan, Z.; Gao, G.; Zhao, B. *Polymers* **2017**, *9*, 70.
(119) Spiridon, I.; Leluk, K.; Resmerita, A. M.; Darie, R. N. *Composites Part B: Engineering* **2015**, *69*, 342-349.

(120) Zhang, Y.; Liao, J.; Fang, X.; Bai, F.; Qiao, K.; Wang, L. *ACS Sustainable Chemistry & Engineering* **2017**, *5*, 4276-4284.
(121) Patwardhan, P. R.; Brown, R. C.; Shanks, B. H. *Journal of Chemistry and Sustainability, Energy and Materials* **2011**, *4*, 1629-1636.
(122) Bugg, T. D. H.; Ahmad, M.; Hardiman, E. M.; Singh, R. *Current Opinion in Biotechnology* **2011**, *22*, 394-400.
(123) Martínez A. T.; Speranza M.; Ruiz-Dueñas F. J.; Ferreira P.; Camarero S.; Guillén F.; Martínez M. J.; Gutiérrez A.; del. Río J. C. *International Microbiology* **2005**, *8*, 195-204.
(124) Matrakova, M.; Rogachev, T.; Pavlov, D.; Myrvold, B. O. *Journal of Power Sources* **2003**, *113*, 345-354.
(125) Nirmale, T. C.; Kale, B. B.; Varma, A. J. *International Journal of Biological Macromolecules* **2017**, *103*, 1032-1043.
(126) Lu, H.; Cornell, A.; Alvarado, F.; Behm, M.; Leijonmarck, S.; Li, J.; Tomani, P.; Lindbergh, G. *Materials* **2016**, *9*, 127-145.
(127) Chatterjee, S.; Jones, E. B.; Clingenpeel, A. C.; McKenna, A. M.; Rios, O.; McNutt, N. W.; Keffer, D. J.; Johs, A. *ACS Sustainable Chemistry & Engineering* **2014**, *2*, 2002-2010.
(128) Tenhaeff, W. E.; Rios, O.; More, K.; McGuire, M. A. *Advanced Functional Materials* **2014**, *24*, 86-94.
(129) García-Negrón, V.; Phillip, N. D.; Li, J.; Daniel, C.; Wood, D.; Keffer, D. J.; Rios, O.; Harper, D. P. *Energy Technology* **2017**, *5*, 1311-1321.
(130) Chatterjee, S.; Clingenpeel, A.; McKenna, A.; Rios, O.; Johs, A. *RSC Advances* **2014**, *4*, 4743-4753.
(131) Chen, T.; Zhang, Q.; Xu, J.; Pan, J.; Cheng, Y.-T. *RSC Advances* **2016**, *6*, 29308-29313.
(132) Zhao, H.; Wang, Q.; Deng, Y.; Shi, Q.; Qian, Y.; Wang, B.; Lu, L.; Qiu, X. *RSC Advances* **2016**, *6*, 77143-77150.
(133) Zhang, L.; You, T.; Zhou, T.; Zhou, X.; Xu, F. *ACS Applied Materials & Interfaces* **2016**, *8*, 13918-13925.
(134) Jeon, J. W.; Zhang, L.; Lutkenhaus, J. L.; Laskar, D. D.; Lemmon, J. P.; Choi, D.; Nandasiri, M. I.; Hashmi, A.; Xu, J.; Motkuri, R. K.; Fernandez, C. A.; Liu, J.; Tucker, M. P.; McGrail, P. B.; Yang, B.; Nune, S. K. *Journal of Chemistry and Sustainability, Energy and Materials* **2015**, *8*, 428-432.
(135) Ruiz-Rosas, R.; Valero-Romero, M. J.; Salinas-Torres, D.; Rodriguez-Mirasol, J.; Cordero, T.; Morallon, E.; Cazorla-Amoros, D. *Journal of Chemistry and Sustainability, Energy and Materials* **2014**, *7*, 1458-1467.
(136) Hu, S.; Zhang, S.; Pan, N.; Hsieh, Y.-L. *Journal of Power Sources* **2014**, *270*, 106-112.
(137) Lai, C.; Zhou, Z.; Zhang, L.; Wang, X.; Zhou, Q.; Zhao, Y.; Wang, Y.; Wu, X.-F.; Zhu, Z.; Fong, H. *Journal of Power Sources* **2014**, *247*, 134-141.
(138) Ma, X.; Kolla, P.; Zhao, Y.; Smirnova, A. L.; Fong, H. *Journal of Power Sources* **2016**, *325*, 541-548.
(139) Saha, D.; Li, Y.; Bi, Z.; Chen, J.; Keum, J. K.; Hensley, D. K.; Grappe, H. A.; Meyer, H. M.; Dai, S.; Paranthaman, M. P.; Naskar, A. K. *Langmuir* **2014**, *30*, 900-910.
(140) Ago, M.; Borghei, M.; Haataja, J. S.; Rojas, O. J. *RSC Advances* **2016**, *6*, 85802-85810.
(141) Navarro-Suarez, A. M.; Carretero-Gonzalez, J.; Roddatis, V.; Goikolea, E.; Segalini, J.; Redondo, E.; Rojo, T.; Mysyk, R. *RSC Advances* **2014**, *4*, 48336-48343.
(142) Tian, J.; Liu, Z.; Li, Z.; Wang, W.; Zhang, H. *RSC Advances* **2017**, *7*, 12089-12097.
(143) Lu, H.; Zhao, X. S. *Sustainable Energy & Fuels* **2017**, *1*, 1265-1281.
(144) Rodríguez, J. J.; Cordero, T.; Rodríguez-Mirasol, J. In *Production of Biofuels and Chemicals from Lignin*; Fang, Z., Smith, J. R. L., Eds.; Springer Singapore: Singapore, 2016, p 217-262.
(145) Xia, K.; Ouyang, Q.; Chen, Y.; Wang, X.; Qian, X.; Wang, L. *ACS Sustainable Chemistry & Engineering* **2016**, *4*, 159-168.
(146) Li, H.; Yuan, D.; Tang, C.; Wang, S.; Sun, J.; Li, Z.; Tang, T.; Wang, F.; Gong, H.; He, C. *Carbon* **2016**, *100*, 151-157.
(147) Zhang, W.; Lin, H.; Lin, Z.; Yin, J.; Lu, H.; Liu, D.; Zhao, M. *Journal of Chemistry and Sustainability, Energy and Materials* **2015**, *8*, 2114-2122.
(148) Milcazrek, G.; Inganas, O. *Science* **2012**, *335*, 1468-1471.
(149) Leguizamon, S.; Díaz-Orellana, K. P.; Velez, J.; Thies, M. C.; Roberts, M. E. *Journal of Materials Chemistry A* **2015**, *3*, 11330-11339.
(150) Admassie, S.; Nilsson, T. Y.; Inganas, O. *Physical Chemistry Chemical Physics* **2014**, *16*, 24681-24684.
(151) Nagaraju, D. H.; Rebis, T.; Gabrielsson, R.; Elfwing, A.; Milczarek, G.; Inganäs, O. *Advanced Energy Materials* **2014**, *4*, 1300443.

(152) Nilsson, T. Y.; Wagner, M.; Inganas, O. *Journal of Chemistry and Sustainability, Energy and Materials* **2015**, *8*, 4081-4085.
(153) Rębiś, T.; Nilsson, T. Y.; Inganäs, O. *Journal of Materials Chemistry A* **2016**, *4*, 1931-1940.
(154) Admassie, S.; Ajjan, F. N.; Elfwing, A.; Inganas, O. *Materials Horizons* **2016**, *3*, 174-185.
(155) Ajjan, F. N.; Jafari, M. J.; Rębiś, T.; Ederth, T.; Inganäs, O. *Journal of Materials Chemistry A* **2015**, *3*, 12927-12937.
(156) Xu, H.; Jiang, H.; Li, X.; Wang, G. *RSC Advances* **2015**, *5*, 76116-76121.
(157) Ajjan, F. N.; Casado, N.; Rebis, T.; Elfwing, A.; Solin, N.; Mecerreyes, D.; Inganas, O. *Journal of Materials Chemistry A* **2016**, *4*, 1838-1847.
(158) Chen, K.; Song, S.; Liu, F.; Xue, D. *Chemical Society Reviews* **2015**, *44*, 6230-6257.
(159) Raccichini, R.; Varzi, A.; Passerini, S.; Scrosati, B. *Nature Materials* **2015**, *14*, 271-279.
(160) Xiong, C.; Zhong, W.; Zou, Y.; Luo, J.; Yang, W. *Electrochimica Acta* **2016**, *211*, 941-949.
(161) Chaleawlert-umpon, S.; Berthold, T.; Wang, X.; Antonietti, M.; Liedel, C. *Advanced Materials Interfaces* **2017**, *4*, 1700698.
(162) Guin, P. S.; Das, S.; Mandal, P. C. *International Journal of Electrochemistry* **2011**, 816202.
(163) Rafiee, M.; Nematollahi, D. *Electroanalysis* **2007**, *19*, 1382-1386.
(164) Du, J.; Wang, S.; You, H.; Zhao, X. *Environmental Toxicology and Pharmacology* **2013**, *36*, 451-462.
(165) Zurutuza, A.; Marinelli, C. *Nature Nanotechnology* **2014**, *9*, 730-734.
(166) Titirici, M.-M.; White, R. J.; Brun, N.; Budarin, V. L.; Su, D. S.; del Monte, F.; Clark, J. H.; MacLachlan, M. J. *Chemical Society Reviews* **2015**, *44*, 250-290.
(167) Gosselink, R. J. A.; de Jong, E.; Guran, B.; Abächerli, A. *Industrial Crops and Products* **2004**, *20*, 121-129.
(168) Emanuelsson, R.; Sterby, M.; Strømme, M.; Sjödin, M. *Journal of the American Chemical Society* **2017**, *139*, 4828-4834.
(169) Pirnat, K.; Mali, G.; Gaberscek, M.; Dominko, R. *Journal of Power Sources* **2016**, *315*, 169-178.
(170) Milczarek, G. *Electroanalysis* **2007**, *19*, 1411-1414.
(171) Danielson, B.; Simonson, R. *Journal of Adhesion Science and Technology* **1998**, *12*, 923-939.
(172) Aracri, E.; Diaz Blanco, C.; Tzanov, T. *Green Chemistry* **2014**, *16*, 2597-2603.
(173) Chou, S. L.; Pan, Y.; Wang, J. Z.; Liu, H. K.; Dou, S. X. *Physical Chemistry Chemical Physics* **2014**, *16*, 20347-20359.
(174) Zhang, S. S.; Xu, K.; Jow, T. R. *Journal of Power Sources* **2004**, *138*, 226-231.
(175) Maleki, H.; Deng, G.; Kerzhner-Haller, I.; Anani, A.; Howard, J. N. *Journal of The Electrochemical Society* **2000**, *147*, 4470-4475.
(176) Martins, P.; Lopes, A. C.; Lanceros-Mendez, S. *Progress in Polymer Science* **2014**, *39*, 683-706.
(177) Zhu, Z. *International Journal of Electrochemical Science* **2016**, 8270-8279.
(178) Qu, Q. T.; Wang, B.; Yang, L. C.; Shi, Y.; Tian, S.; Wu, Y. P. *Electrochemistry Communications* **2008**, *10*, 1652-1655.
(179) Lux, S. F.; Schappacher, F.; Balducci, A.; Passerini, S.; Winter, M. *Journal of The Electrochemical Society* **2010**, *157*, A320-A325.
(180) Zhang, Z.; Zeng, T.; Lai, Y.; Jia, M.; Li, J. *Journal of Power Sources* **2014**, *247*, 1-8.
(181) Nguyen, V. H.; Wang, W. L.; Jin, E. M.; Gu, H.-B. *Applied Surface Science* **2013**, *282*, 444-449.
(182) Yuan, J.; Prescher, S.; Sakaushi, K.; Antonietti, M. *Journal of Materials Chemistry A* **2015**, *3*, 7229-7234.
(183) Krause, A.; Kossyrev, P.; Oljaca, M.; Passerini, S.; Winter, M.; Balducci, A. *Journal of Power Sources* **2011**, *196*, 8836-8842.
(184) Dolah, B. N. M.; Deraman, M.; Othman, M. A. R.; Farma, R.; Taer, E.; Awitdrus; Basri, N. H.; Talib, I. A.; Omar, R.; Nor, N. S. M. *Materials Research Bulletin* **2014**, *60*, 10-19.
(185) Basri, N. H.; Deraman, M.; Kanwal, S.; Talib, I. A.; Manjunatha, J. G.; Aziz, A. A.; Farma, R. *Biomass and Bioenergy* **2013**, *59*, 370-379.
(186) Berenguer, R.; Garcia-Mateos, F. J.; Ruiz-Rosas, R.; Cazorla-Amoros, D.; Morallon, E.; Rodriguez-Mirasol, J.; Cordero, T. *Green Chemistry* **2016**, *18*, 1506-1515.
(187) Domínguez-Robles, J.; Sánchez, R.; Díaz-Carrasco, P.; Espinosa, E.; García-Domínguez, M. T.; Rodríguez, A. *International Journal of Biological Macromolecules* **2017**, *104*, 909-918.
(188) Duval, A.; Lawoko, M. *Reactive and Functional Polymers* **2014**, *85*, 78-96.
(189) Leitner, S.; Gratzl, G.; Paulik, C.; Weber, H. *Journal of Carbon Research* **2015**, *1*, 43-57.
(190) Saidane, D.; Barbe, J. C.; Birot, M.; Deleuze, H. *Journal of Applied Polymer Science* **2010**, *116*, 1184-1189.
(191) Areskogh, D.; Li, J.; Gellerstedt, G.; Henriksson, G. *Biomacromolecules* **2010**, *11*, 904-910.
(192) Fitgau, L. F.; Peter, F.; Boeriu, C. G. *Acta Biochimica Polonic* **2013**, *60*, 817-822.

(193) Wells Jr, T.; Kosa, M.; Ragauskas, A. J. *Ultrasonics Sonochemistry* **2013**, *20*, 1463-1469.
(194) Malutan, T.; Nicu, R.; Popa, V. I. *BioResources* **2008**, *3*, 13-20.
(195) Ang, A.; Ashaari, Z.; Baker, E. S.; Ibrahim, N. A. *BioResources* **2015**, *10*, 4795-4810.
(196) El Mansouri, N.-E.; Yuan, Q.; Huang, F. *BioResources* **2011**, *6*, 4523-4536.
(197) Lim, Y. B.; Tan, Y.; Perri, M. J.; Seitzinger, S. P.; Turpin, B. J. *Atmospheric Chemistry and Physics* **2010**, *10*, 10521-10539.
(198) Ramires, E. C.; Megiatto Jr, J. D.; Gardrat, C.; Castellan, A.; Frollini, E. *Bioresource Technology* **2010**, *101*, 1998-2006.
(199) Chaleawlert-umpon, S.; Liedel, C. *Journal of Materials Chemistry A* **2017**, *5*, 24344-24352.
(200) Sen, S.; Patil, S.; Argyropoulos, D. S. *Green Chemistry* **2015**, *17*, 4862-4887.
(201) Fenner, R. A.; Lephardt, J. O. *Journal of Agricultural and Food Chemistry* **1981**, *29*, 846-849.
(202) Tan, S. S. Y.; MacFarlane, D. R.; Upfal, J.; Edye, L. A.; Doherty, W. O. S.; Patti, A. F.; Pringle, J. M.; Scott, J. L. *Green Chemistry* **2009**, *11*, 339-345.
(203) Wysokowski, M.; Klapiszewski, Ł.; Moszyński, D.; Bartczak, P.; Szatkowski, T.; Majchrzak, I.; Siwińska-Stefańska, K.; Bazhenov, V.; Jesionowski, T. *Marine Drugs* **2014**, *12*, 2245-2268.
(204) Shi, R.; Li, B. *Starch - Stärke* **2016**, *68*, 1224-1232.
(205) Chengzhong Cui; Hasan Sadeghifar; Sanghamitra Sen; Argyropoulos, D. S. *Bioresources* **2013**, *8*, 864-886.
(206) Nour-Eddine El Mansouri; Qiaolong Yuan; Farong Huang *Bioresources* **2011**, *6*, 2647-2662.
(207) Navarrete, P.; Pizzi, A.; Pasch, H.; Delmotte, L. *Journal of Adhesion Science and Technology* **2012**, *26*, 1069-1082.
(208) Mansouri, N. E. E.; Pizzi, A.; Salvado, J. *Journal of Applied Polymer Science* **2007**, *103*, 1690-1699.
(209) Grenier-Loustalot, M.-F.; Larroque, S.; Grande, D.; Grenier, P.; Bedel, D. *Polymer* **1996**, *37*, 1363-1369.
(210) Zhang, Y.; Qiang, Z.; Vogt, B. D. *RSC Advances* **2014**, *4*, 44858-44867.
(211) Khan, M. A.; Ashraf, S. M. *Journal of Thermal Analysis and Calorimetry* **2007**, *89*, 993-1000.
(212) Ammar, M.; Khiari, R.; Belgacem, M. N.; Elaloui, E. *Mediterranean Journal of Chemistry* **2014**, *2*, 731-737.
(213) P. Navarrete; A. Pizzi ; K. Rode; M. Vignali; Pasch, H. *Journal of Adhesion Science and Technology* **2013**, *27*, 586-597.
(214) Pu, Y.; Cao, S.; Ragauskas, A. J. *Energy & Environmental Science* **2011**, *4*, 3154-3166.
(215) Constant, S.; Wienk, H. L. J.; Frissen, A. E.; Peinder, P. d.; Boelens, R.; van Es, D. S.; Grisel, R. J. H.; Weckhuysen, B. M.; Huijgen, W. J. J.; Gosselink, R. J. A.; Bruijnincx, P. C. A. *Green Chemistry* **2016**, *18*, 2651-2665.
(216) Fawcett, W. R. *The Journal of Physical Chemistry* **1993**, *97*, 9540-9546.
(217) Duval, A.; Lange, H.; Lawoko, M.; Crestini, C. *Green Chemistry* **2015**, *17*, 4991-5000.
(218) Bitenc, J.; Pirnat, K.; Mali, G.; Novosel, B.; Randon Vitanova, A.; Dominko, R. *Electrochemistry Communications* **2016**, *69*, 1-5.
(219) Pirnat, K.; Gaberscek, M.; Dominko, R. *Journal of Power Sources* **2013**, *235*, 214-219.
(220) Crestini, C.; Crucianelli, M.; Orlandi, M.; Saladino, R. *Catalysis Today* **2010**, *156*, 8-22.
(221) Crestini, C.; Pro, P.; Neri, V.; Saladino, R. *Bioorganic and Medicinal Chemistry* **2005**, *13*, 2569-2578.
(222) Crestini, C.; Caponi, M. C.; Argyropoulos, D. S.; Saladino, R. *Bioorganic and Medicinal Chemistry* **2006**, *14*, 5292-5302.
(223) Bozell, J. J.; Hames, B. R. *Journal of Organic Chemistry* **1995**, *60*, 2398-2404.
(224) Gaspar, A. R.; Gamelas, J. A. F.; Evtuguin, D. V.; Pascoal Neto, C. *Green Chemistry* **2007**, *9*, 717-730.
(225) Kim, Y. S.; Chang, H.-m.; Kadla, J. F. *Holzforschung* **2008**, *62*, 38-49.
(226) Crestini, C.; Saladino, R.; Tagliatesta, P.; Boschi, T. *Bioorganic and Medicinal Chemistry* **1999**, *7*, 1897-1905.
(227) Takahashi, A.; Kurahashi, T.; Fujii, H. *Inorganic Chemistry* **2009**, *48*, 2614-2625.
(228) Che, C. M.; Huang, J. S. *Chemical Communications* **2009**, 3996-4015.
(229) Cole, J. L.; Clark, P. A.; Solomon, E. I. *Journal of the American Chemical Society* **1990**, *112*, 9534-9548.
(230) Lai, Y.-Z.; Guo, X.-P.; Situ, W. *Journal of Wood Chemistry and Technology* **1990**, *10*, 365-377.
(231) Gosselink Richard, J. A.; van Dam Jan, E. G.; de Jong, E.; Gellerstedt, G.; Scott Elinor, L.; Sanders Johan, P. M. *Holzforschung* **2011**, *65*, 155-162.
(232) Akai, S.; Kita, Y. *Organic Preparations and Procedures International* **1998**, *30*, 603-629.

(233) Abraham, I.; Joshi, R.; Pardasani, P.; Pardasani, R. T. *Journal of the Brazilian Chemical Society* **2011**, *22*, 385-421.
(234) Musgrave, O. C. *Chemical Reviews* **1969**, *69*, 499-531.
(235) Snyder, C. D.; Rapoport, H. *Journal of the American Chemical Society* **1972**, *94*, 227-231.
(236) Rao, D. V.; Ulrich, H.; Sayigh, A. A. R. *The Journal of Organic Chemistry* **1975**, *40*, 2548-2549.
(237) Love, B. E.; Simmons, A. L. *Tetrahedron Letters* **2016**, *57*, 5712-5715.
(238) Kim, D. W.; Choi, H. Y.; Lee, K.-J.; Chi, D. Y. *Organic Letters* **2001**, *3*, 445-447.
(239) Peart, C.; Ni, Y. *Journal of Wood Chemistry and Technology* **2001**, *21*, 113-125.
(240) Gnedenkov, S. V.; Opra, D. P.; Zemnukhova, L. A.; Sinebryukhov, S. L.; Kedrinskii, I. A.; Patrusheva, O. V.; Sergienko, V. I. *Journal of Energy Chemistry* **2015**, *24*, 346-352.
(241) Gnedenkov, S. V.; Opra, D. P.; Sinebryukhov, S. L.; Tsvetnikov, A. K.; Ustinov, A. Y.; Sergienko, V. I. *Journal of Industrial and Engineering Chemistry* **2014**, *20*, 903-910.
(242) Gnedenkov, S. V.; Sinebryukhov, S. L.; Opra, D. P.; Zemnukhova, L. A.; Tsvetnikov, A. K.; Minaev, A. N.; Sokolov, A. A.; Sergienko, V. I. *Procedia Chemistry* **2014**, *11*, 96-100.
(243) Argyropoulos, D. S.; Heitner, C. *Holzforschung* **1994**, *48*, 112-116.
(244) Argyropoulos, D. S.; Zhang, L. *Journal of Agricultural and Food Chemistry* **1998**, *46*, 4628-4634.
(245) Zawadzki, M.; Ragauskas, A. "Quantitative Determination of Quinone Chromophores in isolated Lignins," Institute of Paper Science and Technology Atanta, Georgia, 1999.
(246) Wang, J.; Deng, Y.; Qian, Y.; Qiu, X.; Ren, Y.; Yang, D. *Green Chemistry* **2016**, *18*, 695-699.
(247) Berthold, T.; Castro, C. R.; Winter, M.; Hoerpel, G.; Kurttepeli, M.; Bals, S.; Antonietti, M.; Fechler, N. *Chemistry of Nanomaterials for Energy, Biology and More* **2017**, *3*, 311-318.
(248) Laheäär, A.; Przygocki, P.; Abbas, Q.; Béguin, F. *Electrochemistry Communications* **2015**, *60*, 21-25.
(249) Thring, R. W.; Chornet, E.; Bouchard, J.; Vidal, P. F. *Industrial & Engineering Chemistry Research* **1991**, *30*, 232-240.
(250) Ferdosian, F.; Yuan, Z.; Anderson, M.; Xu, C. *RSC Advances* **2014**, *4*, 31745-31753.